Towards an Energy-Efficient Inductively-Powered Ultra-High Frequency Pulsed Neurostimulator

C. Toitos

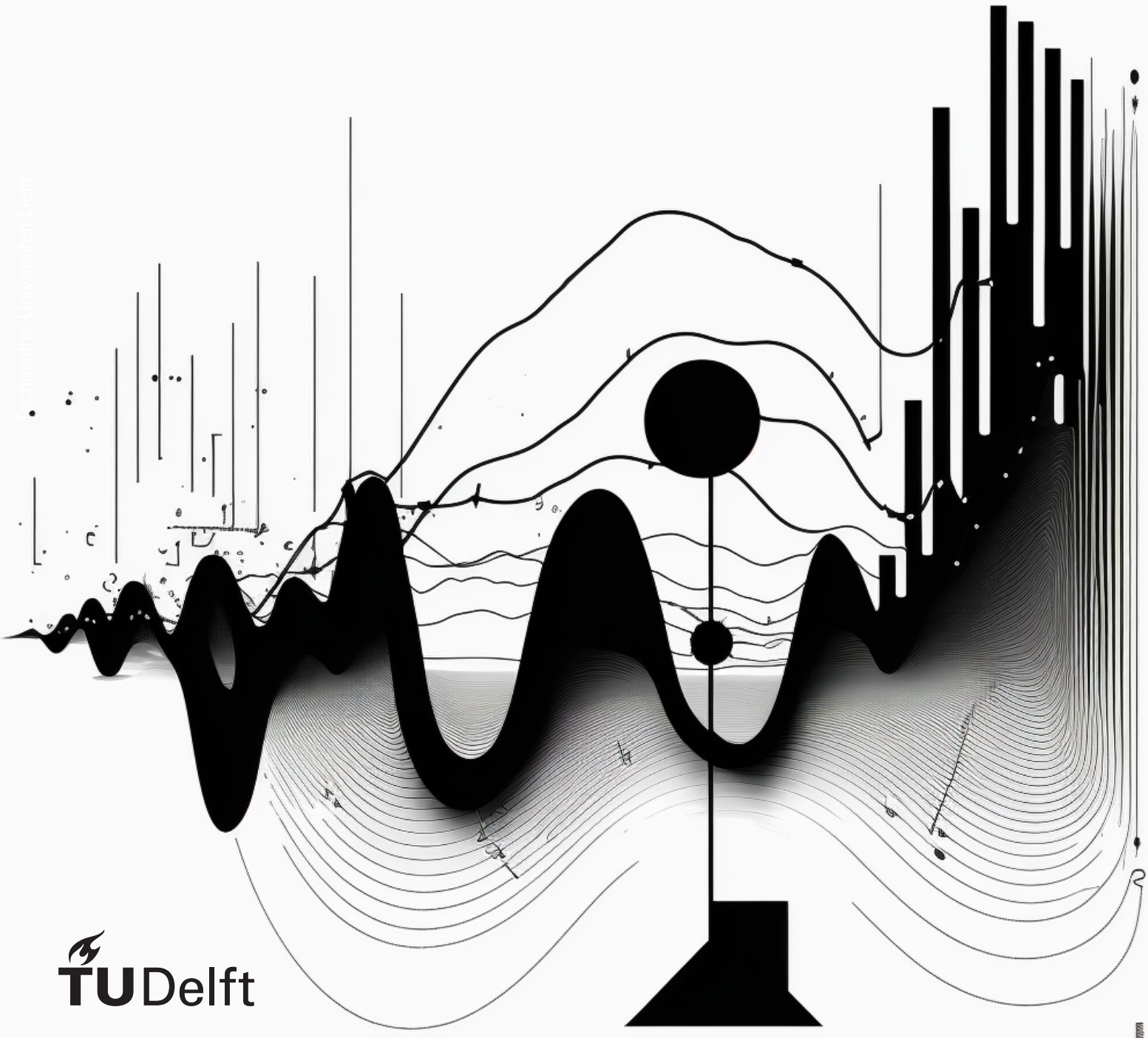

TU Delft

Towards an Energy-Efficient Inductively-Powered Ultra-High Frequency Pulsed Neurostimulator

by

C. Toitos

to obtain a double degree of

Master of Science
in Electrical and Biomedical Engineering

at the Delft University of Technology,
to be defended publicly on Wednesday April 26, 2023 at 09:00 AM.

Student number:	4635930	
Project duration:	January, 2019 – April, 2023	
Thesis committee:	Prof. dr. ir. W.A. Serdijn,	TU Delft, supervisor
	Dr. V. Giagka,	TU Delft, supervisor
	Dr. ir. C.J.M. Verhoeven,	TU Delft

An electronic version of this thesis is available at `http://repository.tudelft.nl/`.

TU Delft

Abstract

Electrical stimulation has emerged as a promising therapeutic modality for the treatment of various neurological disorders such as Parkinson's disease, chronic pain, epilepsy, and depression. In addition, recent studies have provided evidence supporting the effectiveness of electrical stimulation as a treatment option for patients with chronic migraine and cluster headaches who have been unresponsive to other therapies. Specifically, stimulation of the occipital and supraorbital nerves has shown promise in managing these refractory conditions. Current implantable medical devices (IMDs) are battery-powered, which increases the size of the implant and involves lengthy wires to connect with the electrodes. Wireless power transfer (WPT) techniques can be used to reduce the size and omit the battery from the implants. However, conventional power management methods use a rectifier, power converter, and neurostimulator to convert the AC power of the link to DC power and provide electrical stimulus, which lowers implant power efficiency.

This thesis presents a novel neurostimulator circuit that salvages and stores available energy from an inductive link. The circuit design includes an inductor for energy storage and utilizes a buck-boost converter-like topology to deliver the stored energy to the tissue. This topology exploits the capacitive membrane's characteristics and injects the charge into the tissue through ultra-high frequency pulsed stimulation without requiring additional circuits that may contribute to power losses. Operating at the resonance frequency of 6.58MHz, the circuit was designed and simulated to inject approximately 500nC at an 18mm distance from the transmitter. Furthermore, the proposed circuit design incorporates a charge-metering circuit adapted to ensure stimulation efficacy in response to coupling variations. To guarantee safety during stimulation, the residual voltage is carefully monitored and brought close to zero at the end of each stimulation cycle. To achieve this, a charge-balancing scheme has been implemented, which utilizes a comparator to monitor the residual voltage across the electrode.

The proposed circuit was designed on a printed circuit board (PCB) to evaluate its feasibility. To evaluate its performance, a signal generator was used to simulate the input of the inductive link, and an electrode-tissue interface (ETI) model was used at the output. The circuit demonstrated its efficacy in measuring the charge and reducing the residual voltage within established safety limits while maintaining energy efficiency. More specifically, the charge metering measured a charge of 404nC for 450nC of injected charge, which is 10.22% of error. Moreover, the circuit exhibited a linear response in controlling the injected charge. In the tested range, the charge balancing scheme yielded residual voltages ranging from -20mV to -16mV. The effectiveness of the charge balancing scheme was further confirmed through *in-vitro* measurements in a phosphate-buffered solution, with residual voltages measuring at -20mV, which falls within the safe range. Finally, the implemented circuit achieved a peak efficiency of 56%.

Acknowledgements

As I write these lines, I realise that the long and exceptional journey as a student in Delft has ended. However, looking back, I am grateful for the unique individuals I have met. These people have been a constant source of inspiration, support, and encouragement, and I could not have achieved this important milestone without their help.

First, I would like to thank Wouter for his endless patience and for encouraging my ideas despite my difficulties in supporting them. I must admit that his exceptional approach to teaching was the driving force behind my decision to enrol in the Master of electrical engineering and finally become a member of the bioelectronics group. A warm thank you to Vasso, who has been equally supportive and encouraging. I genuinely admire your competence in bringing clarity to my jumbled logic. I will never forget how both of you showed a more personal and supportive side during the most challenging phases of my thesis. Thank you so much for being there.

I am very grateful to the Bioelectronics group for being such a warm and welcoming community and always willing to share their knowledge and offer assistance. Many thanks to all of you for your kindness and generosity.

My deepest gratitude goes to my friends who have been with me throughout this journey. I want to express my appreciation for all the beautiful memories. Your unwavering support and presence during this journey from the beginning until now have been invaluable. I recognise that none of this would have been achievable without you.

Last, I would like to extend my thankfulness to my family for their unconditional love and patience. Menia and Vivi, you have been my rock through all the highs and lows, and I am thankful for having you in my life. You all have always believed in me and supported me in pursuing my choices to become the person I am.

C. Toitos
Delft, April 2023

Contents

List of Figures

List of Tables

1 Introduction

The nervous system monitors, integrates, and communicates information within and outside the body, controlling thoughts, actions, and emotions. It primarily comprises neurons, which transmit electrical and chemical signals. Until now, the most common way to tackle a disease is by using medicine, focusing on the chemical part. However, this method demonstrates poor specificity and often affects other body functions, introducing unwanted side effects. Conversely, neural stimulation focuses on the electrical component of a specified nervous system area. Its characteristics demonstrate a localized, instantaneous and reversible response as opposed to the chemical reaction.

Early applications of electrical stimulation involved cardiac pacemakers, which were used to treat arrhythmias, and cochlear implants, which restored hearing for those with severe hearing loss. With advancements in integrated circuit technology, a variety of neural prosthesis devices utilizing electrical stimulation have been developed, including retinal implants for vision restoration. Additionally, deep brain stimulation (DBS) has been employed to treat a range of neurological disorders, such as Parkinson's disease, pain, dystonia, and Tourette syndrome [1].

The present clinical devices exhibit adverse effects resulting from their large dimensions and the extensive wires connecting the neurostimulator to the electrodes [2]. Decreasing the size of the device could lead to better integration and minimize harmful events related to the wires. However, achieving miniaturization requires improving the power efficiency beyond that of conventional neurostimulators, which could decrease the size of the source or improve the level of integration. This thesis aims to investigate the efficient design of an inductively-powered electrical neurostimulator.

1.1. Background

The power conversion efficiency of an implant is a crucial parameter for achieving the miniaturization of the device. In conventional neurostimulators, power management is employed to convert the AC input from the inductive link into a fixed potential, V_{DD}, through an AC-DC conversion. The effectiveness of this conversion is a critical factor in determining the overall efficiency of the implant.

Fig. 1.1 illustrates a system-level circuit diagram of an inductively powered neurostimulator, where power is transferred from an external transmitter to the electrodes. In such a setup, the energy transmitted from the secondary link to the electrodes is subject to dissipation at each stage of the power transfer, ultimately decreasing efficiency. The overall efficiency of the implant can be determined by the product of the efficiencies of all circuits involved in the AC-DC conversion process, which is expressed in (1.1).

$$\eta_{implant} = \eta_{AC-DC} \times \eta_{NS} \tag{1.1}$$

where η_{AC-DC} is the efficiency of the AC to DC conversion, that is equal to the product of η_{Rec} and η_{pc} which are the efficiencies of the rectifier and the power converter. η_{NS} denotes the efficiency of the neurostimulator. Improving implant efficiency ($\eta_{implant}$), offers several advantages, including the potential to decrease the dimensions of the inductive link and mitigate the risk of tissue damage resulting from heat dissipation.

Numerous techniques have been employed to improve the efficiency of power conversion stages. Passive rectifiers often exhibit low efficiency due to their high voltage drop or large reverse currents. To tackle this issue, voltage-threshold compensation techniques and active synchronous rectifiers have been utilized to minimize the voltage drop. However, the peak reported efficiency at the 13.56MHz frequency is limited to 80% [3]. Power converters also contribute to power loss, and they also introduce two additional off-chip components. Furthermore, current-mode neurostimulators consume significant power across the current drivers, primarily due to the large voltage difference between the supply and tissue peak voltage [4] [5]. In the case of voltage-mode stimulators, they must drive the electrode adiabatically to minimize the power dissipation across its resistance. To accomplish this, the output voltage of the stimulator should be as high to keep a constant current injected into the electrode. Adiabatic switched-mode converters have demonstrated efficiencies lower than 60% [6] [7]. In conclusion, power losses at each stage considerably impact overall efficiency, leading to poor performance.

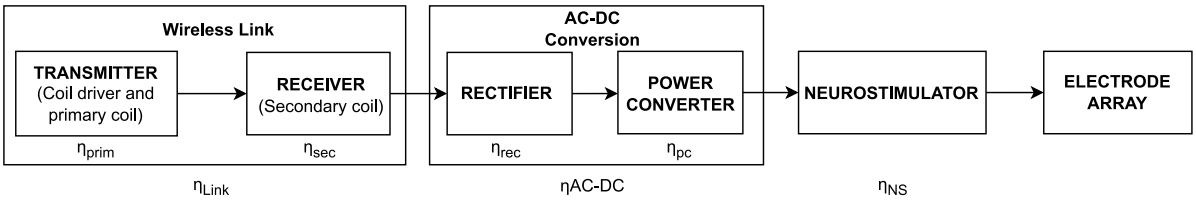

Figure 1.1: System level representation of an inductively powered neurostimulator. The implant power management employs a rectifier and a linear regulator to supply a fixed voltage to the neurostimulator. The implant efficiency equals the product of η_{AC-DC} and η_{NS}.

In contrast, it is feasible to develop a neurostimulator with an inductive link that fluxes energy into the tissue, thereby reducing the number of stages required. In [8], it was demonstrated that the capacitive property of neuron membranes could be leveraged to accumulate current until the threshold is reached. By utilizing this property, it is possible to bypass a number of circuits employed in the AC-DC rectification stages, which has as a main goal to provide a constant voltage across the neurostimulator.

1.2. Problem Statement

Considering the limitations observed in the power management techniques employed by the conventional neurostimulator, a question arises as to whether it is possible to decrease the current number of stages employed to generate a fixed voltage for the neurostimulator, which inherently leads to low power efficiency. Therefore, we hypothesise that the efficiency of the neurostimulator can be improved by reducing the number of stages, enabling implant miniaturization and power reduction.

1.3. Goal and Approach

The goal of this thesis is to improve the efficiency of wirelessly-powered neurostimulators by implementing innovative stimulating waveforms with a minimum number of circuit blocks. The proposed approach exploits the membrane's capacitive characteristic to integrate the total current, independent of the stimulating waveform. By doing so, energy can be transferred from the wireless link to the tissue using a single circuit, which reduces the power dissipation in the AC-DC conversion stages. The proposed approach has the potential to improve the overall efficiency of wirelessly-powered neurostimulators. This improvement can help reduce the power requirements of the implant, which, in turn, may benefit miniaturizing the device. Moreover, a topology for measuring and balancing the charge has been implemented to ensure the effectiveness and safety of the device.

1.4. Outline

This thesis is organized into the following chapters. In Chapter 2, an assessment is made of the viability of electrical stimulation as a treatment for chronic migraine and cluster headaches. The chapter also provides the theoretical fundamentals of wireless power transfer methods and electrical stimulation and presents an overview of state-of-the-art designs that enhance the power efficiency of the implant, particularly in relation to wireless power transfer links. Chapter 3 outlines the design of the ultra-high-frequency pulsed neurostimulator and describes the preliminary simulations undertaken dur-

ing the design phase. In Chapter 4, circuit simulations of the overall system are presented, as well as PCB measurements carried out using a linear tissue model and actual electrodes. Chapter 5 discusses and concludes the results of the study. This final chapter also discusses the contributions of this study and provides recommendations for future research in this field.

2

Literature review

2.1. Neural Stimulation

The concept of electrical stimulation dates back to 46 A.D. when the physician Scribonius Largus suggested electricity for treating headaches and gouty arthritis [9]. The means to produce electricity was an electric fish to conduct electrotherapeutic experiments until the seventeenth century. In 1658, the Dutch scientist Jan Swammerdam reported the first documented scientific experiments in neuromuscular physiology. In his experiments, he confuted prior beliefs that muscle contraction is a consequence of nervous fluid inflow. However, he probably did not clearly understand the exact stimulation origin. The contraction happened due to the current generated by the dissimilar metals Swammerdam used to pinch the motor nerve. During the next century, many European scientists performed a series of experiments in electrophysiology using electrical stimulation, which was made more accessible, given the technological advancements in the field. For example, Jean Jallabert used the Leyden jar -The first capacitor discovered at the University of Leiden- to electrically stimulate muscles for paralysis treatment. Galvani, similar to Swammerdam, also conducted numerous neuromuscular experiments using a bimetallic arch [9]. But did not have a clear understanding of the mechanism. Alessandro Volta continued the experiments and better understood the chemical electricity mechanism.

The scientific revolution transformed the views of our society about nature. The emerging knowledge from all the fundamental sciences gave a better insight into many aspects of our daily life, including the best machine of them all, our body. Since the body is an electrochemical system, we traditionally use medicine to treat diseases. They aim to target chemical components related to their pathophysiology, influencing their behaviour, e.g., by altering the conductivity of gated ion channels [10]. However, the specificity of pharmaceutical treatments is poor and affects other functions of our body that introduce side effects, i.e., drowsiness, fatigue, and dizziness. Advances in electronic miniaturization gave rise to neural stimulation that targets the electronic component of our nervous system to treat diseases. It offers a better resolution and an immediate response to the nervous system than drugs. The effects are immediate when stimulation activates the targeted neuronal circuits and reverses upon deactivation.

The dose delivered to the patient depends on the stimulation intensity. Current devices operate in an open loop, which means that dose delivery is adjusted according to the needs of each patient by the physician. That is similar to a drug subscription where the physician adjusts the dosage according to his empirical opinion. Closed-loop systems have been envisioned to deliver tailor-specific stimulation parameters to the subject based on measurements. Although a feedback loop that will correct in response to physiological advancements can increase the efficiency and efficacy of stimulation, there exist complexities for its implementation. Currently, few devices are used in clinical practice [11]. In this report, we will focus on the efficiency of the neurostimulator design itself. Moreover, neurostimulation can elicit a neuronal response using different forms of energy: magnetic, electric, light, and acoustic. In this report, we will focus on electric stimulation, in which we drive the electrodes with current to generate a potential that will alter the transmembrane resting voltage.

Electric stimulation is used for Deep Brain Stimulation (DBS) to treat numerous neurological disorders such as Parkinson's disease, dystonia, and tremor. It has also shown benefits in restoring neural input. Typical applications are retinal and cochlear stimulation. Spinal cord stimulation (SCS) is an-

other widely used application to suppress pain. It has also shown potential benefits in clinical practice. For example, recent studies have shown that occipital and supraorbital nerve stimulation can benefit patients suffering from chronic migraines.

2.2. Case Study: Migraine

In 2016, migraine was reported as the second leading cause of disability worldwide, affecting more than 10% of the global population [12]. Migraines can vary in different ways: intensity, frequency, location, and cause.

Headaches classify as primary and secondary. In primary headaches, the underlying cause is unknown - it affects 46% of the population. Its associated symptoms are possibly one-sided pain in the head, nausea, vomiting, and sensitivity to light. In secondary headaches, migraine is a symptom, and the underlying conditions could be a spinal injury, brain tumor, or post-traumatic events. In that case, the treatment should target the pathophysiology of the underlying condition itself. The main classification in primary migraines concerns the frequency of occurrence. Patients experience migraines with different frequencies, and they are expected to change dynamically. Those who encounter headaches less than 15 days/month are episodic, while patients that encounter headaches more than 15 days/month are chronic. Fig. 2.1 shows the correlation of patient disability with headache days/month. It is apparent that with the increase in the headache frequency per month, the percentage of patients experiencing disability also increases. Most patients with chronic headaches attending neurology centres have chronic migraine or cluster headaches, of which the estimated prevalence is 2% and 0.02%, respectively [13]. It is reported in the literature that the quality of life of individuals suffering from chronic migraine is impaired. At the same time, they experience more significant disability and economic burden compared to episodic migraine patients [14] [15]. Hence, it is of primary importance to stop the frequency of occurrence.

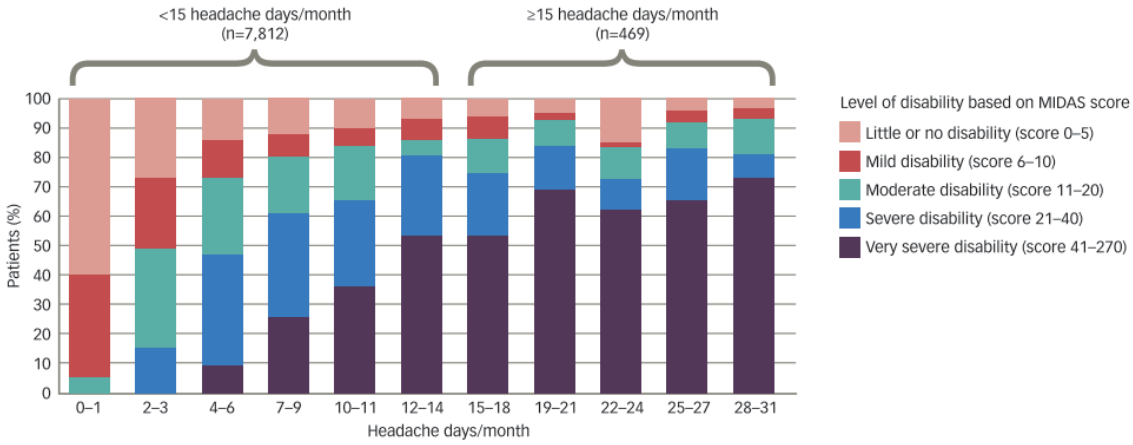

Figure 2.1: Correlation between the numbers of headache days per month and disability score [16]. Image is taken from [10].

2.2.1. Preventive Treatments for Chronic and Cluster Headaches

Currently, migraine has no cure due to its unknown pathophysiology. However, due to its high prevalence, healthcare providers have become increasingly skilled in tracking its symptoms and trigger mechanisms to prevent it. The existing approaches involve modifying the lifestyle, use of medication, and other therapeutic modalities. Current preventive treatments include antiepileptics, antidepressants, beta-blockers, angiotensin-converting enzyme inhibitors, and angiotensin receptor blockers, which also have shown satisfactory results when used by episodic migraine patients [16]. However, these treatments become ineffective in chronic migraine and cluster headache patients, while frequent medication intake leads to overuse-related headaches. The best-case scenario's response rate of the preventive treatments does not exceed 50%, while it is much lower for chronic migraine cases. In addition, preventive drug treatments have a high adverse effect profile (Fig. 2.2). For that reason, most of the patients are intractable to pharmacological treatment. Only one-third of the people eligible for preventive treat-

ments receive them, and out of these, over three-quarters discontinue the treatment throughout 1-year due to efficacy and safety limitations and the long time it takes to achieve clinical benefit [16]. A recent study suggested that the concentration of calcitonin gene-related peptide (CGRP) is high in areas related to migraine pathophysiology, indicating its possible relevance. M. Ashina [17] conducted a short-term analysis to test the efficacy of anti-CGRP (erenumab) with a subgroup of 492 participants with prior preventive treatment failure. The results showed that the average monthly migraine days was half for 41% of the participants. Although the results show better performance from previous pharmaceutical treatments, a 69% in the study remains untreated, meaning that a significant minority remains refractory from any pharmacological treatment.

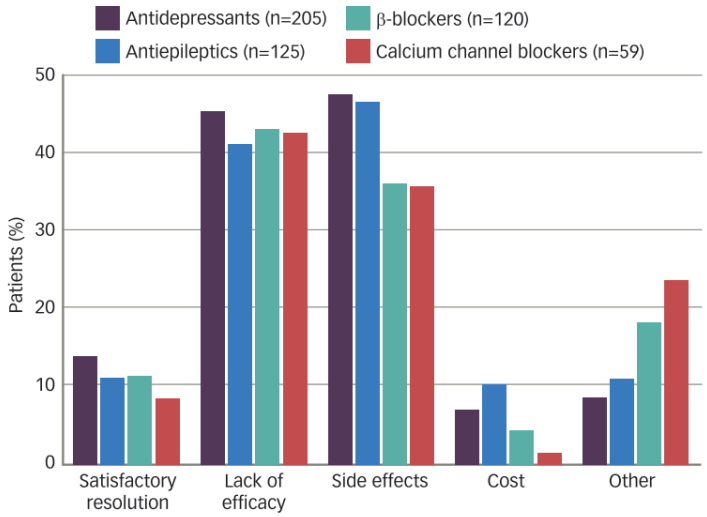

Figure 2.2: Evaluation of patient satisfaction, efficacy, safety and costs for various preventive treatments (i.e Antidepressants, Antiepileptics, β-blockers, calcium channel blockers) [16].

2.2.2. Electrical Stimulation for Pain

Neurostimulation of central and peripheral pathways may help drug-intractable patients to modulate pain. Although the exact pathophysiology of migraine is unknown, multiple targets are used in neurostimulation, including the supraorbital nerve, posterior hypothalamus/ventral tegmental area, a sphenopalatine ganglion (SPG), occipital nerve, vagus nerve, and cortex. These areas are relevant because they connect with the trigeminovascular complex, which plays a significant role in pain transmission from the head and facial regions to higher brain centres [18]. In addition, some targets are responsible for preventive treatment, thus relaxing the initial area of sensitization. Other areas provide acute treatment that stops cortical spreading and depression and activates the brain stem - an area responsible for pain control.

Currently, existing non-invasive devices target the vagus, supraorbital nerve, and cortex. However, most of these methods have demonstrated clinical benefits for episodic migraines and episodic cluster headaches [13]. Additionally, the device for Vagus nerve stimulation supports its efficacy in chronic cluster headaches, but the only evidence provided is a manufacturer-sponsored trial [13].

Available invasive stimulation devices target occipital nerves, SPG, and the deep brain (ventral tegmental area). A multicenter trial studied the efficacy of SPG stimulation with 28 patients. It reported a significant difference in resolved cluster attacks between the active and control group (67% - 7%). After three months of stimulation, only 31% of the sham group continued acute medication in contrast with 77% of the controlled group [19]. More than 60 open-label studies of deep brain stimulation for the treatment of chronic cluster headache show an average response rate of 66% [13]. A single randomized placebo-controlled trial of 11 patients studied the response rate after a month follow-up period. The response rate between the two groups did not show a significant statistical difference, which could be due to the short study period [20].

Currently, three controlled studies regarding occipital nerve stimulation demonstrate mixed results. The ONSTIM (Occipital Nerve Stimulation for the Treatment of Intractable Chronic Migraine Headache)

study [21] is the first published multicenter, randomized, blinded, controlled study to obtain efficacy and safety data. Sixty-one patients were divided into active stimulation (28 patients), preset (16), and medical management (17). The responders' rate was defined as >50% reduction in monthly migraine days and a 3-point reduction in pain intensity compared to baseline. At the end of the study, the responders were 39%, 6%, and 0% in active stimulation, medically managed, and preset stimulation, respectively. The PRISM (Precision Implantable Stimulator for Migraine) [2] conducted a multicenter double-blinded control trial of 125 patients with refractory migraine. The difference between the active and sham-stimulation groups was not statistically different. The first showed a decrease of 5.5 migraine days/month, while the latter showed a reduction of 3.9 migraine days/month after three months of stimulation. Silberstein et al. designed the third randomized controlled study of 157 patients [22]. The responders were those who achieved 50% or greater reduction in mean visual analogue scores (VAS). The study did not show a significant statistical difference in the active and sham groups (17% vs 14%). However, there was a significant difference in the headache days reduction for the active and sham group (27% and 15%), and the subjects achieved at least a 30% reduction in headache days (38% vs 19%). Open-label studies have also demonstrated the clinical benefits of occipital nerve stimulation for patients suffering from refractory chronic migraine and cluster headache. The average response rate was 67% and 56% for patients with cluster headache and chronic migraine, respectively [13].

Reed et al. were the first to hypothesize that neurostimulation should target the areas where migraine usually is expressed to suppress pain [23]. This will result in some form of paresthesia effect on the parts of the body that hurt. This rationality was also in line with the spinal cord stimulation used to suppress extremities and back pain. In our case, migraine is experienced in both the frontotemporal region innervated by the supraorbital nerve and the occipital region innervated by the occipital nerve. Therefore, it would make more sense to stimulate both areas. Moreover, these nerves also connect to the trigeminocervical complex. Thus, stimulation should be done at both affected areas to provide a better paresthesia effect. Reed et al. published an open-label, non-randomized study where seven patients with CM were implanted [23]. All the patients had at least a 50% reduction in severity and 83% pain reduction. In addition, Hann et al. [24] conducted a case study that showed that 71% of the patient had at least a 50% decrease in severity, further supporting the argument for the efficacy of dual neurostimulation.

Work	Study Design	Total patients	Stimulation site	Comments	Adverse Events
Reed [23]	Open-label, non-randomized structure	7	ONS and SONS	100% had reduced severity and frequency	Lead migration (14.3%), infection (14.2%), Allergic reaction to IPG (14.2%)
Haan & Sharan [24]	Case series	14	ONS and SONS	71% had reduced severity (>50%) and frequency	Lead migration (42.8%), Lead site allodynia (21.4%), infection (14.2%), Surgical intervention (35.7%)
Saper [21]	Prospective, multicenter, randomized, blinded and placebo-controlled	66	ONS	39% had $\geq$ 50% reduced frequency	Lead migration (24%),
Silberstein [22]	Double-blinded, randomized study	157 Control group (n=52) Active group (n=105)	ONS	No significant statistical difference between active and control group	Lead migration (18.7%), Numbness at IPG/Lead site (21.5%)
Dodick [2]	Double-blinded, randomized study	157 Control group (n=52) Active group (n=105)	ONS	50% had $\geq$ 50% reduced severity and frequency, improved lifestyle	Lead migration (18.5%), Nubmness at IPG/Lead (24%),
Rodrigo [25]	Uncontrolled, open-label observational study	35	ONS	93 % Long term efficacy (Medically intractable) 63% reduced frequency, improved lifestyle	Infection (8.1%)

Table 2.1: Summary of studies to test occipital nerve stimulation (ONS) and combined with supraorbital nerve stimulation (SONS).

2.2.3. Surgical Implantation

Neurostimulators consist of three parts, the implantable pulse generator (IPG), the extension wires, and the leads. The IPG is the bulkiest part of the neurostimulator. Thus, it is implanted ipsilaterally in the abdomen or the chest region. It consists of the battery and controls and connects to the electrodes with an extension lead as shown in Fig. 2.3.

The electrodes for the supraorbital nerve are anchored in the temporal region posteriorly of the ear and they are tunneled laterally to the forehead. At this point, another incision is made to insert the electrodes perpendicular to the supraorbital nerves. Similarly, for the occipital nerve, an incision is made laterally of the occipital bone and the electrode is inserted across the path of the nerve. Finally, the extension lead connects with the electrode wires in the upper cervical region.

Stimulation of occipital and supraorbital nerves has several advantages compared to deep brain stimulation since it does not involve craniotomy. Most importantly, that makes the implantation of the device minimally invasive. However, the design of the device is poor due to the IPG bulky size, which requires wires to run from the torso to the head. Some of the adverse events related to poor design

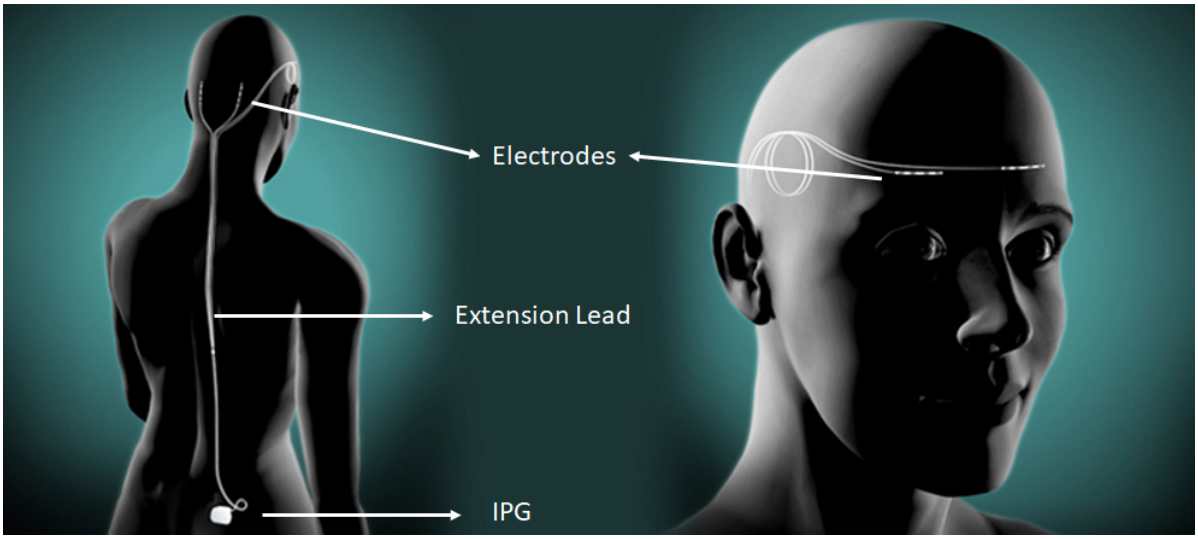

Figure 2.3: Implant for Occipital and Supraorbital nerve stimulation.

of the device are lead migration and infection. Table. 2.1 enlist the adverse events encountered in the aforementioned studies that were conducted for the efficacy of neurostimulation to treat migraines. Moreover, it can also result in potential problems in the circuit due to additional losses and electromagnetic interference. The latter becomes especially relevant in ultra-high frequency stimulation since the radiation increases at higher frequencies. Different values are reported for the frequency of occurrence of lead migration which seems to depend on the operator and surgery [13]. The life span of such a device depends on the battery life. When the battery runs down, surgery is required to replace it. This increases the potential risk for more failures as well as the cost of the treatment.

Therefore, the goal is to miniaturize the device and place it proximal to the electrodes. In such a way, we will minimize the adverse events.

2.2.4. Requirements for the Implant

The challenges of the existing methods are due to the invasiveness of such a device. Battery-powered neurostimulators increase the device's size, and, in such cases, often extensive wires are required to connect the IPG to the electrode arrays, as shown in Fig. 2.3. Therefore, such an implant architecture increases the risk of infection, pain and malfunction of the implant itself. Those challenges pose the requirements for the implant. Hence, the system should be long-lasting, miniaturized and reliable. This means that the system should be powered wirelessly to eliminate the battery. This choice will also eliminate the long wires of the system. Additionally, it should achieve high power efficiency to make the system smaller. Hence, a smaller transmitter and receiver can meet the power demands of the neurostimulator. Finally, the device needs to be able to transfer information based on its status and patient-related measurements.

2.3. Active Implantable Biomedical Microsystems

The goals for an active implantable neurostimulator are its miniaturization, durability, efficacy, efficiency and safety. All these requirements are a function of many implant aspects related to system and circuit-level operation. Moreover, the requirements depend on the stimulation parameters, such as the waveform and the mechanism employed for tissue excitation. For example, a larger stimulation charge threshold will require a bigger coil to satisfy the power demands. Although implantable medical devices (IMDs) can differ at some level, we can introduce a high-level system description to allow further elaboration in the subsequent sections. Wirelessly powered IMDs consist of a transmitter and receiver, but we will focus on the components of the latter. The system components are generally divided into power management, data telemetry, the controller and the stimulator. Fig. 2.4 shows the system level architecture of a neurostimulator.

For the system components to perform correctly, the implant must communicate information with

the external devices and vice versa. The two types of information used in implants are distinguished into sensory data and implant parameters. The first involves the stimulation parameters according to the needs of the patient. In that way, the information can change according to each patient. The latter consists of any parameter that relates to the operation of the implant itself. This can be information regarding the state of the stimulation, the power usage and the injected energy into the tissue.

Apart from the data link, a power link is used to power the implant. An inductive power link is usually tuned at 12.56MHz and can also be used for low-speed uplink. For higher-speed downlink, an optical data transmitter is used to avoid interference with the power link. Stimulation implants use two separate power links; a high-voltage level power reception, often adaptive for the stimulation unit, and a smaller coil for a 3.3V supply for the digital circuit.

As the name indicates, power management is responsible for the power reception and regulation to ensure proper circuit operation. Each circuit on the implant receives its energy from the power management unit. The most common topology to manage the energy is a rectifier and a linear drop-out regulator that converts and regulates the energy to a fixed voltage supply.

The control unit is connected to each part of the circuit and is responsible for proper and safe operation. It can either receive data from the data telemetry channel and decode them to stimulation parameters and channel configuration by adjusting the switches or code valuable measurement data to send back to the transmitter. For instance, it can increase the transmitted power due to insufficient voltage on the receiver or vice versa. A common safety mechanism is to short the receiver for over-voltage protection.

Last but not least, the neurostimulator block consists of a stimulator circuit, the electrode array and the charge balancing circuit. The stimulator circuit is the source that drives the electrodes and provides enough electric charge to the tissue for excitation or inhibition. For the design of the stimulation circuit, it is important to consider which electrical quantity to use, as this choice directly affects the power efficiency and the stimulation safety of the system. Its selection also depends on the application requirements (i.e. number and size of electrodes) and specifications. The charge balancing circuit is necessary to ensure that the electrodes will operate within a safe electrochemical regime.

The following chapter is divided into two sections: Sec. 2.4 deals with the stimulator block and presents all the required information for the design of an efficient, efficacious and safe neurostimulator. It first provides a model for the electrode-tissue interface, which provides a common ground for further discussion on the system power efficiency in relation to the stimulation quantity and parameters. This section also explores tissue dynamics and potential stimulation waveforms that can take advantage of them. Finally, it reviews different charge balancing techniques. In Sec. 2.5, we first review the possible wireless powering methods for a neurostimulator. Then, we provide the fundamental theory of near-field inductive coupling and the appropriate expressions to extract the electrical parameters from the geometrical characteristics. Next, we derive link expressions based on the electrical parameters to give insight into the potential performance of the inductive link. Finally, we provide state-of-the-art techniques to achieve better power transfer efficiency.

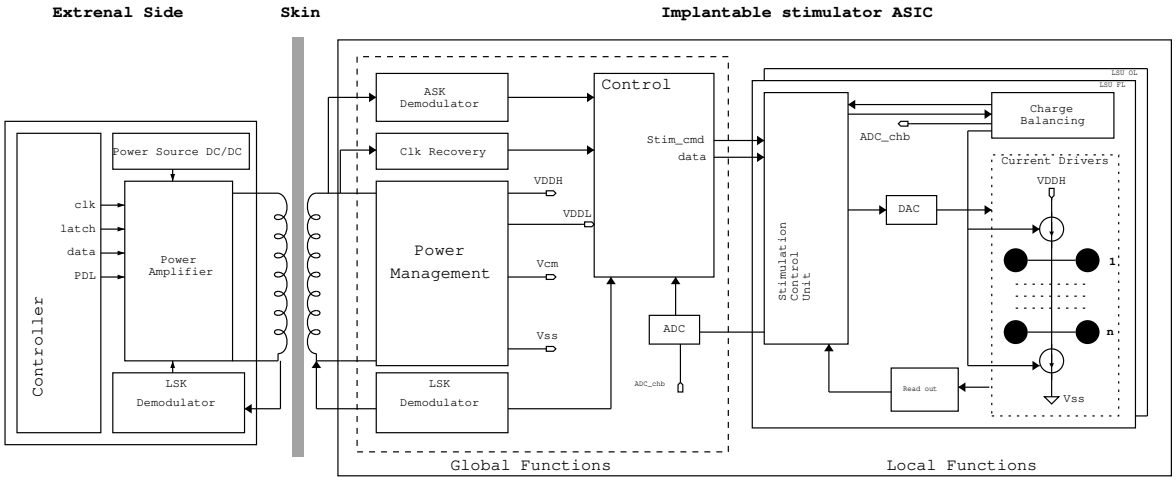

Figure 2.4: System level architecture of inductively-powered conventional neurostimulator.

2.4. Stimulation of Neural Tissue

The electrical energy that is received by the implant is injected into the tissue using an electrode array. Thus, the electrode array and the tissue form the stimulator load. To analyze the neurostimulator's power efficiency and safety, we need to define an accurate model.

Energy transfer happens through different processes due to the electrochemical nature of the environment. For example, electrons are responsible for charge transfer in the electrode-tissue interface, while ions transfer charge in tissue. Thus, each part is modelled with a different impedance: the electrode-tissue interface impedance (Z_{if}) and the tissue impedance (Z_{tis}).

2.4.1. Model of the Electrode-Tissue Interface

The simplest neurostimulator circuit involves two electrodes where current passes through the electrolyte. The current is injected into the working electrode (WE), and a counter electrode (CE) is required for the current to complete the path. A potential is formed upon placing the electrodes in the tissue to establish the electrochemical equilibrium, modelled as V_{eq}.

Primarily, two charge transfer processes occur at the electrode-tissue interface: First is the non-Faradaic process, where the charge is transferred through chemical species redistribution while no electrons are involved. Second is the Faradaic process, where electrons are the charge transfer mechanism between the electrode and electrolyte interface leading to reduction-oxidation reactions [26].

The two charge transfer processes should be modelled into electrical components according to the interaction type; charge accumulation and electrochemical reactions. The non-Faradaic charge transfer mechanism in the electrode-tissue interface is modelled with the dual-layer capacitor C_{dl}, which models the accumulated charge at the electrode-electrolyte interface. Since the charge is stored on the interface, we can reverse it by changing the current polarity. Besides the charge accumulation, the dual-layer capacitor modells the reversible electrochemical reactions, which manifest themself as charge accumulation across the interface. For instance, this happens when hydrogen atoms are bound to the electrode interface, increasing the stored charge.

The Faradaic processes are to model with the impedance R_{CT} where charge transfer occurs by means of reduction and oxidation reactions. When electron transfer occurs, products form at the electrode that cannot be recovered upon reversing the current (i.e. oxygen evolution). Generally, the process involved in the charge transfer depends on the electrode overpotential -the potential difference of the electrode with its equilibrium when an external voltage is applied. At small potentials over the equilibrium, charge transfer primarily happens through a non-Faradaic process and the Faradaic current is small. As the overpotential increases, current starts conducting through the Faradaic branch exponentially. Hence, energy transfer shifts from the capacitive to the resistive current branch as the potential increases, so it should remain low. The electrode overpotential depends on the total capacitance (i.e. large capacitance per area). For example, an electrode with a large total capacitance can store more charge for a small overpotential compared to an electrode with a smaller total capacitance.

In electrical terms, one can think of the reversible process as charge storage and the irreversible process as a dissipative conductive path. The values of C_{dl} and R_{CT} depend on the electrode properties and geometry. In the case of, for example, ideal polarizable electrodes (i.e. Platinum), charge injection occurs only by means of a non-Faradaic process. Although in the case of non-polarizable electrodes, charge injection occurs through the Faradaic process. Due to the complex electrochemical kinetics, their values are non-linear and thus intricate to be determined. For circuit simulations, a linear model is often used that considers the non-Faradaic charge transfer process and the tissue impedance.

The tissue is modelled with an impedance and its voltage determines the strength of the electric field. Modelling the tissue is a challenging task due to its complex nature. Some of the properties that we can incorporate into its model are non-linearity, anisotropy, time-variant, inhomogeneity, and dynamic properties. Due to the complexity, it is hard to simulate such a model in circuit simulation, and thus it is often simplified to a resistor R_{tis}. The impedance also depends on the electrode geometry. Large electrodes have a smaller impedance due to their effective area requiring higher current than small electrodes to generate the electric field strength. Due to their size, larger electrodes generate a spatially larger electric field that affects more neurons and thus lowers the stimulation specificity.

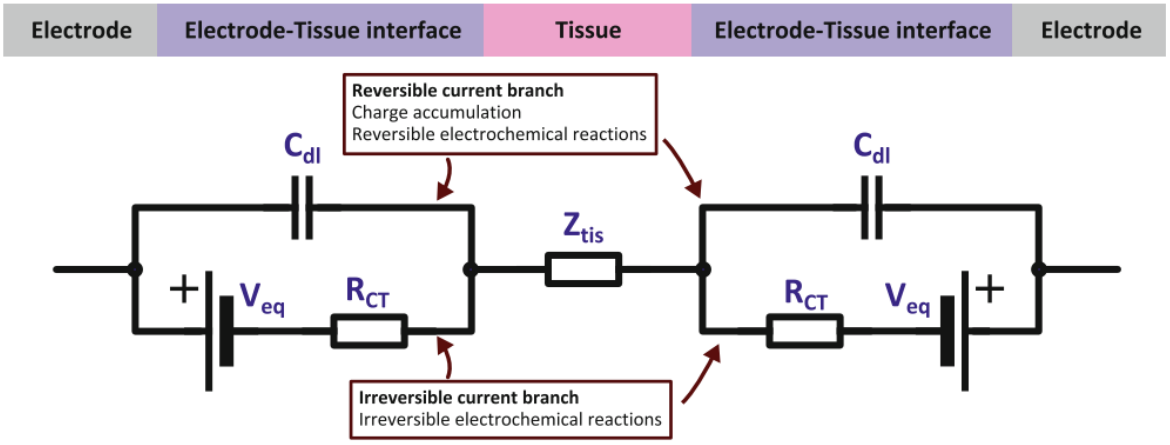

Figure 2.5: Model of the electrode-tissue impedance. It consists of: the electrode-tissue interface impedance that it is divided into a capacitive reversible branch C_{dl} and a resistive irreversible current branch (R_{CT}); the tissue impedance is modelled with a resistor. Image taken from [27]

2.4.2. Neuronal Level: Axonal Activation

Activation of neural tissue is achieved by injecting charge into the tissue itself. Thereby, the electrode is driven to a negative potential that makes the membrane potential difference more positive. The charge flows through the membrane due to its conductive and capacitive characteristics and the active ion charge pumps. When reaching a certain threshold, the neuron elicits an action potential [10]. The amount of charge required to activate the neuron depends on several factors, including the stimulation waveform, the type of stimulation, the stimulation frequency, electrode configuration, and geometry. Most importantly, it depends on the threshold of each corresponding neuron cell. Whether the cell's threshold is reached depends on stimulation strength and duration. This relation is illustrated by the strength-duration and charge-duration curves. See Fig. 2.6. As the stimulation pulse width increases, the threshold current I_{th} decreases. For an infinitely long pulse the current that can elicit an action potential is called the Rheobase current I_{Rh} and the chronaxy is the time it is required for activation to occur when the current intensity is $2I_{Rh}$ [26].

Alternatively, the charge-duration curve describes the activation, which plots the current integration over time - Increasing the stimulation period will increase the charge threshold. This is due to accommodation phenomena where a prolonged subthreshold stimulus leads to sodium pump inactivation and thus increases the threshold to elicit an action potential.

The strength-duration and charge-duration curves represent the tissue excitation qualitatively. On the other hand, quantitative parameters, such as I_{Rh} and Q_{min} depend on the tissue properties (e.g. thickness).

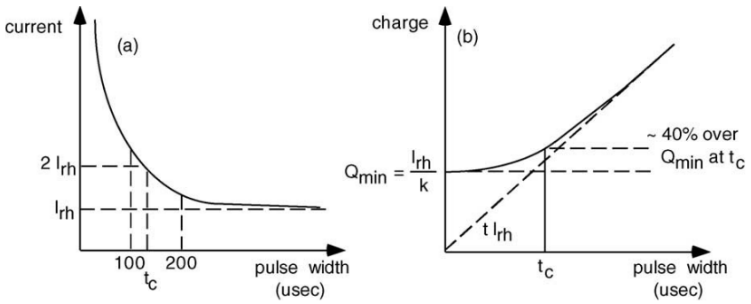

Figure 2.6: Strength- and Charge- duration curve. Image taken from [26]

2.4.3. Methods of Electrical Stimulation

Generally, three stimulation methods are used to inject charge into the tissue: Voltage-controlled stimulation, current-controlled stimulation, and switched-capacitor stimulation. Depending on the application, some methods could be more legitimate than others. Voltage-controlled stimulation provides high-efficiency stimulation, but charge control is complicated since the accurate load impedance is not known [7] [28]. The voltage across the tissue depends on the impedance of the electrode-tissue interface that changes over time and the electrode location. Moreover, during stimulation, the charge accumulates on the double-layer capacitance and the voltage across the tissue impedance decreases. Hence, charge balancing on the voltage-controlled stimulation is tricky since the exact charge depends on the electrode and electrode-tissue impedance. If the residual voltage exceeds the water window, the reactions taking place in the extracellular fluid can damage the electrode and tissue. [7] introduced a stimulator that uses inductive storage to drive the electrode. At the same time, it also claims the advantage of recovering the energy transferred back to the source, thus doing some energy recycling. The dynamic supply is constantly controlled to adiabatically drive the electrode and minimize the losses across tissue impedance. However, this method requires individual channel control, making scaling impractical since the circuit needs to be replicated as many times as the number of electrodes.

Current-controlled stimulation, on the contrary, is independent of electrode-tissue interface (ETI) impedance and thus provides better charge control and a safe method for charge balancing. The constant current also mitigates the losses that would otherwise happen if driven by a non-adiabatic process. However, this comes at the expense of reduced power efficiency due to the dropout voltage on the current source. In practice, current drivers must be designed with a large supply voltage to drive large electrode impedance that will accommodate the worst-case scenario. When the impedance is much lower, the extra energy dissipates on the driver. The efficiency degrades even more when multiple stimulation sites are required [29] [4] [30]. A common technique to mitigate power losses of the driver and increase the efficiency is to adapt the power supply voltage of the neurostimulator across the electrode voltage [5] [31] [32]. Nevertheless, the system efficiency is still limited since the power supply adapts to the driver with the highest power demand. That driver will operate with minimum power loss, while the rest of the channels with over-designed supplies will introduce losses to the system. Efficiency is inversely proportional to the number of channels which is a typical issue affecting retinal implants where many electrodes are used to increase the spatial resolution [5].

In switched-capacitor converters, the currents are exponential and not constant. To adiabatically drive the electrode, a capacitor bank should be deployed to adapt at its potential. This was proposed by [6], where they introduced a switched-capacitor converter performing adiabatic charging between the capacitors and the electrode. In essence, this approach replicates the voltage ramp across the electrodes similarly with constant current stimulation. This way, the potential difference between the capacitors and the electrode decreases, which in turn minimizes the losses on the switches between them and the tissue impedance. Although this system can achieve high theoretical efficiency, compared to the one-step capacitor that charges and discharges energy to the tissue, the measured efficiency was low due to the complex control involved in generating all the intermediate voltages required to achieve adiabatic charging. In [33], an adaptive switched-capacitor DC-DC converter was designed to generate four different voltages. The efficiency is limited by the large-voltage switches deployed to generate four voltages and the parasitic capacitances of the capacitors used for the conversion. Similarly, with other adaptive stimulators, the efficiency is degraded when the voltage supplies the driver with the biggest power demand while the rest of the channels operate with lower voltage compliance. [34] proposed a high-frequency switched-capacitor stimulator. A 1:1 switched-capacitor DC-DC converter generates the voltage. The topology consists of two switches that connect a conversion capacitor to the battery and the load. It operates in two non-overlapping phases, Φ_1 and Φ_2. During Φ_1 the capacitor is connected to the power supply to charge. On Φ_2 the capacitor is connected to the load to discharge the stored energy. The design has selected high-frequency operation to scale down the capacitor value to make it easier for integration. In a steady state, where the current stored in the conversion capacitor is equal to the current driving the stimulator, the efficiency can be defined as the ratio of the stimulation to battery voltage. However, the voltage across the electrodes needs to build up before reaching the steady state, and the stimulation voltage is always lower than the supply limiting the power efficiency to less than 100% of the theoretical efficiency. Since the charge in switched capacitor converters is electrode-dependent, additional circuitry is required to keep it within safe boundaries.

2.4.4. Stimulation Waveform Alternatives

Apart from the conventional ways of stimulation, research was done to investigate the effect of different stimulating waveforms that can improve power efficiency. Some works have focused on finding an optimum stimulation waveform/efficient activation, meaning that a stimulator can generate an action potential easier than conventional constant-current stimulation. For instance, [35] demonstrated that activation of neural tissue improves when a Gaussian-shaped waveform is used compared to conventional constant current stimulation. The activation efficiency increases when using an inter-pulse delay in biphasic stimulation [26]. Other works have focused on finding waveforms that allow a more efficient neurostimulator circuit design. In [27], the authors presented a buck-boost converter where the inductor is charged and discharged to the load repetitively. Changing the duty cycle can control the energy flux to the load. Unlike other buck-boost converters, this work omits the output filter capacitor. Thus, the stimulation waveform consists of high-frequency spikes instead of a constant-current rectangular phase, as shown in Fig. 2.7. The integral of both waveforms, hence the charge, is equal.

2.3.4.1 Efficiency of Ultra High-Frequency Pulsed Stimulation

Contrary to constant current stimulation, ultra high-frequency pulsed stimulation can increase system efficiency since it directly connects its output to the tissue. However, the divergence between the performance of both systems increases even more in multichannel stimulation due to the increased current driver loss in low-impedance channels. Instead, high-frequency pulses eliminate the need for a fixed high voltage source and charge the tissue directly. The proposed design used a buck-boost converter where the inductor will draw the energy from a constant battery source and discharge it to the load. In this way, it eliminates the non-exploited voltage headroom [27].

This design can also be used for multichannel operation since the inductor can steer the charge to multiple electrodes in an alternating fashion. Moreover, it can control the stimulation intensity for each channel by adjusting the duty cycle. The flexibility to independently control each channel solves the predominant issue of the current source in multichannel operation where all the channels are supplied with the potential of the highest impedance channel. As a result, ultra high-frequency pulsed stimulation can stimulate efficiently while controlling the injected charge.

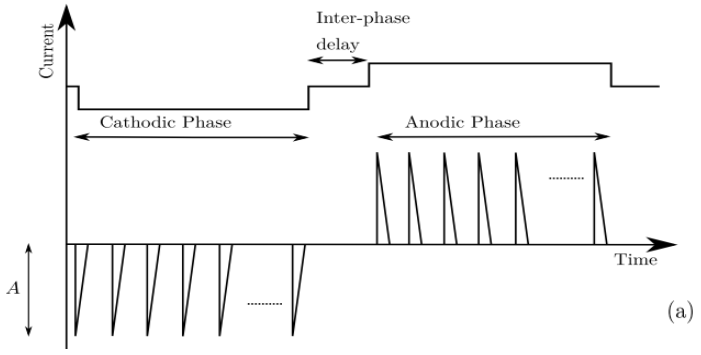

Figure 2.7: A representation of constant current and high-frequency waveform. The current injection to the tissue over time remains the same since the integral of both waveforms are equal. Image taken from [36]

2.3.4.2 Efficacy of High Frequency Stimulation

Ultra high-frequency pulsed stimulation exploits the capacitive characteristics of the tissue. When the high-frequency pulses are sent to the tissue, they are low-pass filtered and determine the transient voltage over and the current through the tissue. The impedance of the tissue was found by converting the complex permittivity and permeability of grey matter as a function of frequency into impedance [8]. In turn, the author used the transient voltage and current to demonstrate how they can influence the neuron membrane. Although activation can happen anywhere in the cell, the axon model was used to determine the membrane voltage. In order to provide input to the axon, the potential of the electrode was considered assuming it acts as a point source and also taking spatial and frequency dependency into consideration $\Phi(r, j\omega) = \frac{I_{tis}(j\omega)}{j\omega\varepsilon_0\varepsilon_r 4\pi r}$.

The potential $\Phi(r, j\omega)$ was used as input to the axon model to describe the membrane voltage response. The cable model is divided into segments: The intracellular path is modelled entirely as an

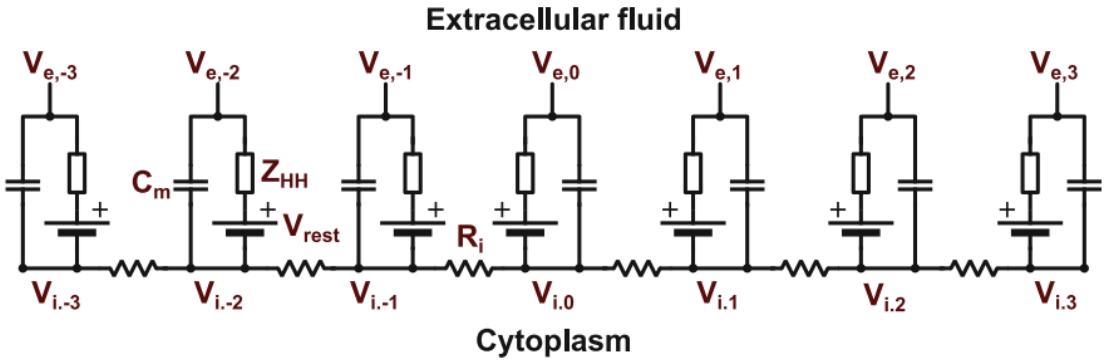

Figure 2.8: An axon model with lumped-element electronic component. Image taken from [27]

intracellular resistance R_i (Ω/cm axon length). At the nodes of Ranvier, a parallel branch is modelled with a non-linear impedance Z_{HH} for the ionic current described by Hodgkin Huxley equations and a series voltage source for the membrane potential V_{rest}. C_m models the capacitive characteristics of the membrane, which acts as a good dielectric.

The results showed that switched-mode stimulation evokes action potentials similar to classical stimulation. Controlling the duty cycle to adjust the intensity can have a similar effect to adapting the amplitude of the classical stimulation. Since the membrane capacitance is much larger than that of the tissue, the capacitance of the membrane dominates and is the one that can filter high-frequency pulses.

Switched-mode stimulation offers many advantages concerning the efficiency, -from the circuit design perspective- multi-channel operation and the size reduction by eliminating the output capacitor often used to stabilize the output voltage at the last stage of the neurostimulator [7]. However, there is no evidence concerning switched-mode stimulation's long-term safety and efficacy. Another essential concern is whether the high-frequency pulses degrade the efficiency from the tissue point of view due to dispersion.

2.4.5. Blocking Capacitors Effectiveness

Coupling capacitors are often used in series with the electrode for charge-balanced stimulation. It is often argued that their use facilitates tissue safety by blocking unwanted DC currents in case of device failure and facilitates passive charge balancing by decreasing the discharge time [37]. During voltage-mode stimulation blocking capacitors isolate the voltage DC levels between the stimulator and the ETI. Thus, the electrode can discharge through the faradaic impedance until the potential difference across the electrode is zero, as shown in Fig. 2.9. Usually, the voltage at the output of stimulators is generated by switching converters [7]. The switching events and ac voltages will result in currents that pass the dc capacitor, eventually resulting in charge accumulation across the electrode. In current stimulators, both DC and AC currents integrate across blocking and dual-layer capacitors, thus providing no protection against charge accumulation. Only in case of device failure or permanent offset currents blocking capacitors can be of use since they will interrupt the stimulation process when the voltage reaches the supply and the electrode will self-discharge instead of accumulating charge on the dual-layer capacitor. See Fig. 2.9. A blocking capacitor adds an extra burden to the voltage headroom due to the voltage drop across it. Therefore, its value should be chosen to be larger than the dual-layer capacitor to minimise the voltage drop. Typical values range between 1-100uF. Due to their large value, they are realised as off-chip components [38]. Since its value is considerably larger, the decrease in discharge time, as argued previously, is negligible and thus barely facilitates passive discharge [37].

Blocking capacitors are a widely used technique to prevent charge balancing and prevent tissue damage in case of device failure. However, they are bulky and their effectiveness is questionable. They are proven neither sufficient for protection nor an effective charge balancing technique. Instead, closed-loop charge-balanced circuits provide safety and a better alternative to bulky coupling capacitors

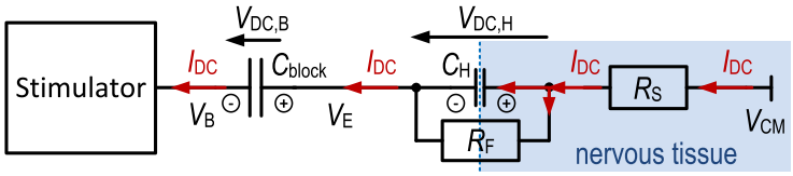

Figure 2.9: The coupling capacitor role when DC currents take palce and the voltage build up across the Cblock and Cdl. Image taken from [38]

2.4.6. Stimulation Safety: Charge Balancing

In order to ensure safe stimulation, it is essential to reverse any accumulated charge over the electrode-tissue interface. That means the voltage of the double-layer capacitor in Fig. 2.5 should remain as close to zero to prevent any irreversible electrochemical reaction (i.e. corrosion). For that reason, an anodic phase follows the cathodic phase to depolarize the cell membrane. However, charge-balanced biphasic stimulation recovers the voltage build-up over the ETI. However, it results in a net positive charge since the injected charge during the cathodic phase also transfers through faradaic reactions. Therefore, only a fraction of the injected charge should be recovered. Due to the non-linear and dynamic tissue properties, we cannot ensure that charge transfer will occur only by means of ion redistribution because this condition will certainly not be satisfied over multiple stimulation cycles, and the voltage will exceed the electrochemically safe regime, resulting in irreversible reaction products [26]. In order to ensure long-term stability, various methods are presented in the literature, which can be divided into subcategories: the passive and the active charge-balancing techniques.

Electrodes shortening is the most straightforward charge-balancing technique. Essentially, the load is shorted to the ground to remove the excess charge stored on the electrode-tissue interface. The discharge time depends on the tissue impedance given by the dual-layer capacitor C_{dl} and the tissue resistance R_s. Therefore, the effectiveness of the passive discharge approach depends on the electrode discharge time and the stimulation parameters. If the stimulation frequency and the electrode impedance are high, there is not enough time for the electrode-tissue interface to return to its resting potential. As a result, the charge accumulates over the stimulation cycles and exceeds the safety margins, compromising the stimulator safety. However, this technique can be effective when combined with active methods. In that case, the residual charge is not only dependent on the resolution of the active methods because passive discharge eliminates the residual charge on the electrode-tissue interface.

Another approach used for charge balancing is push-pull charge matching. That involves matching the cathodic and anodic phase [39] [40] [41] [42]. It is often implemented by making the current magnitudes and the durations the same for both phases, and usually, two approaches exist to implement this. In the first approach, only one current source drives the load and its direction is reversed by employing an H-bridge. To first order, the currents of both phases are equal. Since the charge is the integration of current over time, it is essential to match the phase periods. The second approach uses a current source and a current sink for the anodic and cathodic phases. In that case, there will always be some error due to layout matching and variation in the fabrication process, and thus it is critical to perform current tuning dynamically [40]. Both methods assume a linear load, ensuring charge balancing. However, as mentioned above, charge transfers through the Faradaic branch during the cathodic phase, resulting in a net positive charge at the end of the stimulation. Hence, it is unreasonable to neglect the electrochemical reactions in the tissue and assume that charge-balanced biphasic pulses will result in a net zero charge.

Among the active charge balancing techniques is the charge metering method. In this approach, the charge injected in the tissue during the anodic and cathodic phases is measured using a sensor. Subsequently, when the net charge becomes zero, the stimulation cycle ends. This method allows the freedom to use any stimulation pattern since the zero accumulated charge is what matters in the end. Usually, there are two approaches to sensing the current. The first uses a resistor to sense the current that flows into the tissue and converts this current to voltage. This approach requires three active circuits to compute the charge: an instrumentation amplifier, an integrator and a comparator [43] [44]. The stimulation terminates when the net charge across the ETI is zero. The error charge depends on the delay of the active circuits, and thus their operation should be fast. Moreover, this method is

inherently lossy since a resistor is used on the power path chain, decreasing the system efficiency. The smaller the resistor, the larger the amplification of the error amplifier should be. Additionally, during a biphasic stimulation, the voltage toggles between V_{DD} and V_{SS}. Hence, this also increases the CMRR requirements of the amplifier at high frequencies to sense the voltage difference and reject the common-mode voltage at sharp transitions. The second approach uses a capacitor in the power path to sense the current. Capacitors are inherently current integrators and the accumulation of charge manifests itself as a voltage across it [45] [46]. Unlike the previous approach, the capacitor does not dissipate energy. Instead, it stores energy that will manifest as a voltage drop across the capacitor, which might compromise the efficiency of stimulation. The voltage drop across the capacitor is inversely proportional to its area. Ideally, a small capacitor is required, but the voltage drop is higher for low charge values. Conversely, the voltage drop is small for larger capacitor values as a trade-off to less chip area. Some other methods use the voltage across the electrode to estimate the charge [27]. However, we have stated that the ETI models used are simplified and we do not incorporate their dynamic nature. Thus, if the model is not accurate, the estimation of the injected charge will introduce an error. In order to mitigate the issue of size and voltage drop across the capacitor, [47] used a two-channel system with two capacitors that integrate the current across the tissue in an alternating fashion. The capacitors are connected to a comparator and when their voltage reaches a predefined threshold, the comparator of the active channel triggers HIGH. This will switch the integration channel and let the charged capacitor discharge by shortening it to the ground. Each comparator trigger is used as an input to a counter. When a predefined number of counts is reached, the cathodic phase terminates, meaning that stimulation has reached the necessary injected charge. This approach solves the issue with the size and the voltage drop across the capacitor. Compared to the resistor sensor, the comparator is single-ended and relaxes its requirements. In this approach, the total injected charge is given by $Q_{tot} = NV_{ref}C_{unit}$. Hence, the only concern is to find the right balance between the counts of the charge packets, the reference voltage and the capacitor value. Given the total value of injected charge and a reference voltage, we can choose between a high number of counts and a small capacitor or vice versa. Ideally, the larger the counts, the smaller the value of the capacitor, meaning we can have a coarse charge measurement resolution and potentially small reference voltage. However, in non-ideal situations, time delays will introduce a charge measurement error. Hence, a design choice should be made for those parameters to minimize the error. A more elaborate discussion on this topic is made in Chapter 2.

So far, both methods use a sensor on the stimulation path that is either lossy or affects the stimulation efficiency. [48] has proposed a design that generates a scaled copy of the stimulation current by using a cascoded current mirror on the driver. Like previous designs, a capacitor integrates the current and a comparator compares its voltage to a threshold. The input voltage of the comparator predefines the amount of the injected charge. Compared to the resistor sensor, which employs a differential integrator, this design uses a single-ended comparator which relaxes the requirements. However, the system is limited in terms of scalability since it must replicate each channel. Therefore, it is not suitable for multichannel stimulation. Another drawback of this method is that a constant power supply is required for the correct operation of the cascoded current mirror. In the case of ultra-high frequency pulsed stimulation, where energy is released in the form of small packets directly by an inductor to the tissue, this technique will not be suitable for copying the current.

Pulse insertion is another active charge balancing technique [34] [45]. Unlike the other active methods, pulse insertion is a closed-loop technique that measures the tissue voltage at the end of a stimulation cycle. When the voltage exceeds the safety boundaries, positive or negative pulses are injected, depending on the polarity of the residual voltage, into the tissue to remove the residual charge. Additional active circuits, such as comparators and control units, are required to estimate the charge package's polarity and the available time frame to complete the charge balance until the next stimulation cycle. Care also has to be taken to keep the charge of these pulses small to remain within the safety window, otherwise leading to toggling. Delivering small charge packages will also mitigate stimulation artifacts. On the other hand, small charge packages put time constraints on bringing the residual voltage back to safe limits. If there is not enough time for all the pulses to take place, the voltage will accumulate over the double-layer capacitor. Another closed-loop approach measures the residual voltage and adds an offset charge during stimulation [49] [50] [51]. Its value is continuously adjusted to bring the residual voltage back to zero. Unlike the pulse injection, this method could not lead to stimulation artifacts and unwanted tissue excitation. However, the offset charge can affect the volume of the tissue recruitment since it changes the injected charge. On the other hand, [52] measures

the residual voltage and adjusts the anodic phase of the subsequent stimulation cycle. This method keeps the injected charge during the cathodic phase constant, thus not affecting the volume of tissue recruitment.

Another feedforward technique aims to measure the voltage across the tissue. The advantage of this method is that it neither affects the amount of the injected charge during stimulation nor introduces any stimulation artifacts. However, it strongly relies on the simplified tissue-interphase model that only considers a simple series $R_s C_{dl}$ load. If the model is no longer valid, a residual voltage will remain after a stimulation cycle [48].

The most effective way to ensure safety in long-term stimulation is to combine passive and active charge-balancing methods. In [30], the charge balancing circuit uses pulse insertion, offset regulation and passive discharge. [49] uses a mix of push-pull and offset regulation. In essence, it measures the error between two current sources and injects an offset to correct the error on the next cycle. This calibration scheme is shared among channels, making it suitable for multichannel stimulation.

2.5. Wireless Power Transfer

Each WPT technique generally consists of a receiver that harvests the energy sent by the transmitter. Energy is sent either in the form of wave radiation that propagates away from the source or in the form of reactive energy stored in the antenna vicinity and returns to the transmitter in a regenerative fashion. Fig. 2.10 illustrates WPT techniques that are optimised based on the three critical parameters to meet the requirements of a miniaturised neurostimulator: receiver lateral size, penetration depth and efficiency. Five methods are compared using the principles of electromagnetic and acoustic power transfer (APT). The former consists of the radiative approaches, viz. the far-field, the mid-field and the near-field inductive power transfer (IPT) and capacitive power transfer (CPT). From Fig. 2.10, it turns out that IPT, CPT and APT are the most appropriate power transfer modalities for miniaturised neurostimulators. However, each offers unique advantages, and the choice of the most appropriate method depends on the application requirements.

Far-field and mid-field approaches are suitable to power mm-sized deep-located implants without depending on the limited range of the reactive energy. Instead, energy propagates through a wave from the receiver to the implant. The direction of the propagation depends on the directivity of the antenna. Typically, a high-directivity antenna should be used to avoid unwanted losses due to wave spreading. However, implants use electrically short antennas (ESA) that suffer from poor gain (because of low directivity and efficiency). Therefore, the independence of the energy directionality and the implant location comes at the expense of lower efficiency. As a rule of thumb, the transmission efficiency is optimised when their antenna size becomes comparable to the wavelength. Therefore, the optimal frequency is chosen at the low GHz range for mid-field or far-field systems. However, at high frequencies, the impedance mismatch, tissue absorption losses and energy conversion losses become relevant and contribute significantly to the total system efficiency.

IPT, CPT and APT are the most suitable methods for power miniaturized neurostimulators. APT is appropriate for deep-located implants. Due to its lower attenuation coefficient, acoustic waves can achieve better power transfer capabilities compared to electromagnetic radiation. Since energy radiates, the directionality is of primary importance for the system efficiency. Given the low travelling speed of an acoustic wave, the wavelength is small at low operating frequencies, providing good potential for minimizing the piezoelectric transducer (PZT) size. However, PZTs are off-chip components bonded on a flexible substrate adding to the area of the implant. IPT operates at the low MHz range, where the wavelength is much larger than the coil size, and the reactive energy is predominantly stored in the magnetic field. Therefore, it is appropriate for short to medium transfer distances. Any implant near the transmitter can tap the energy, thus providing a good option for powering many implants within this range. As a rule of thumb, the range roughly equals the diameter of the transmitter coil and decays proportionally to $1/r^3$, with r being the relative concentric distance between the coils. Printed spiral coils (PSC) allow for easy integration in flexible substrates and achieving high reliability, but they come at the expense of a lower quality factor compared to wire-wound coils (WWC) [53]. Lastly, CPT can provide high efficiency for short-range implantation depths. However, it requires large plates to form high effective coupling capacitances. It can integrate in flexible substrates (similar to PSC in IPT), providing a low cost, easy fabrication with high reliability and immunity against electromagnetic interference.

Subsequently, we report the fundamental principles that govern each WPT method. Finally, we

compare them to determine the most appropriate method for our application.

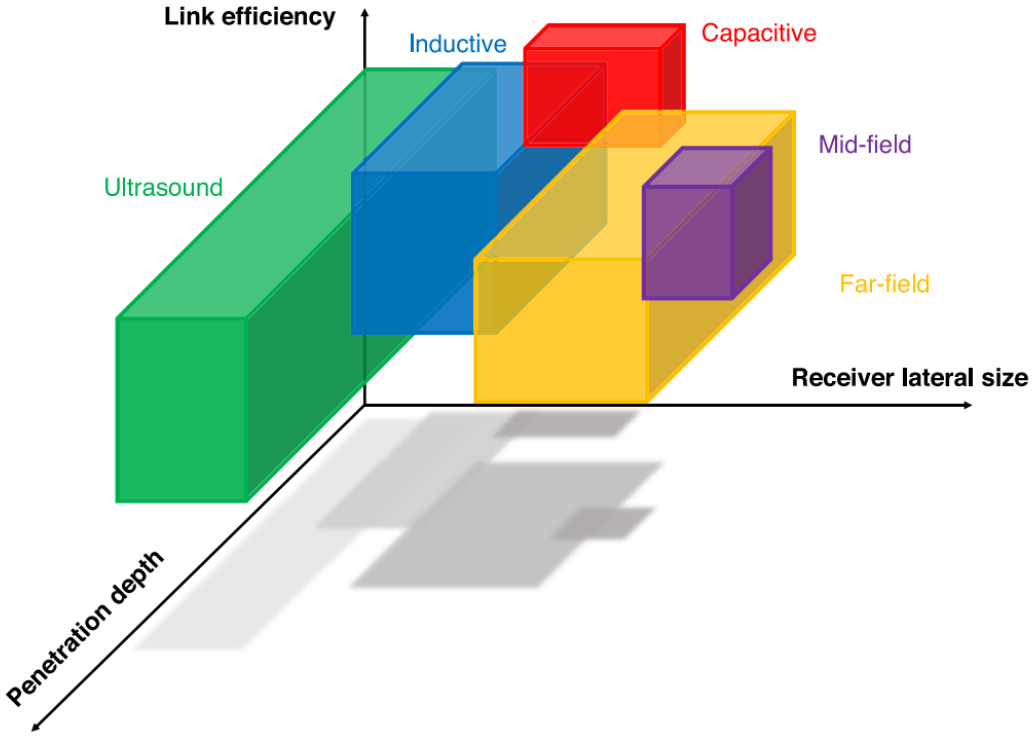

Figure 2.10: Quantitative comparison among WPT methods. Image taken from [54]

Inductive Power Transfer

Inductive coupling is the most widely used method for transcutaneous power transfer. Currently, several FDA-approved neurostimulators employ this method. It works according to the magnetostatic principle. A typical topology consists of a power amplifier driving the transmitter coil, generating a magnetostatic field that couples to the receiver coil. The coupled energy induces an electromagnetic force on the receiving coil, generating the current to power the load. Its magnitude reflects the power that becomes available to the receiver, and its value can be expressed mathematically by Faraday's law:

$$\mathcal{E} = \oint_{\partial\Sigma} \vec{E}.d\vec{l} = -\frac{d}{dt}\oint_{\Sigma} \vec{B}.d\vec{A} \tag{2.1}$$

where EMF ($\mathcal{E}$) is equal to the circulation of electric field ($\vec{E}$) around the coil contour ($\partial\ \Sigma$) which in turn is equal to the negative rate of change of the magnetic field flux through the coil surface (Σ). Also, $d\vec{l}$ and $d\vec{A}$ are the coil contour and surface vector elements, respectively. From (2.1), the power transfer increases by increasing the magnetic field, which is done either by increasing the current on the transmitter side or reducing the distance between the coils. Increasing the transmitter frequency will result in a higher induced EMF on the receiver. Increasing the flux on the receiver side is possible by decreasing the distance and properly aligning both coils or increasing the coil contour. However, the above solutions are limited by the application's geometrical constraints, such as the possible receiver size and the distance between both coils. Although the induced EMF increases by changing the parameters mentioned above, an upper limit is imposed to meet the safety requirements. The maximum Specific Absorption Rate (SAR) safety limit for the human head is set to $1.6W/kg$ [55].

The Power Transfer Efficiency (PTE) metric is of primary importance for each wireless power transfer method. A high PTE means most of the power sent from the primary is delivered to the load. As described above, achieving high power transfer capabilities by increasing the transmitter current and frequency is different from high PTE since the link is subjected to losses. Most relevant losses in IPT

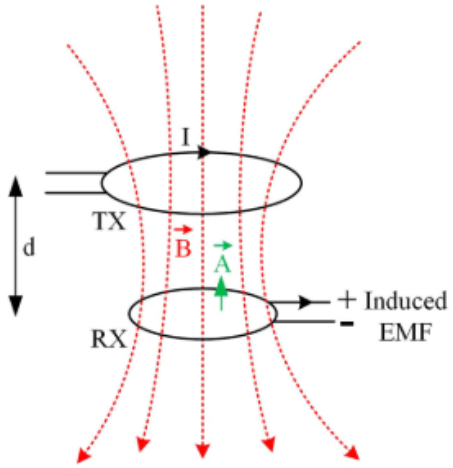

Figure 2.11: Illustration of the induction principle. The magnetic flux crossing the Rx coil generates an EMF to prevent change of the current in the Tx coil. Figure taken from [56]

are due to ac resistance caused by eddy currents and the proximity effect, loose coupling due to large distances, misalignments and tissue losses. The latter is often neglected at the low MHz range and aims to find the frequency that maximizes the coil quality factor. The IPT coils are brought at resonance by adding a capacitor to match the driving frequency. This approach boosts the efficiency of the link under loosely coupled conditions [57]. The capacitor can be placed in parallel and in series with the inductor to match the load, leading to parallel and series resonance. The power requirements of the implantable devices are in the mW range, corresponding to a high impedance. Hence, parallel topology should be used in such applications for impedance matching.

Near-Field Capacitive Coupling

The near-field capacitive coupling has attracted less attention compared to IPT. However, simulation and experimental validation in air medium have shown its potential to perform at high efficiency at short ranges. Additionally, the low-cost fabrication process and reliability resulting from IC integration make this method attractive for miniaturized implants. CPT works on the principle of electric field coupling between two conductors in the near field. Each conductor provides a path for the forward and backward current resulting from the electric field change on the capacitor plates. It is the displacement current that is responsible for wireless power transfer across the capacitor plates, and it requires no medium.

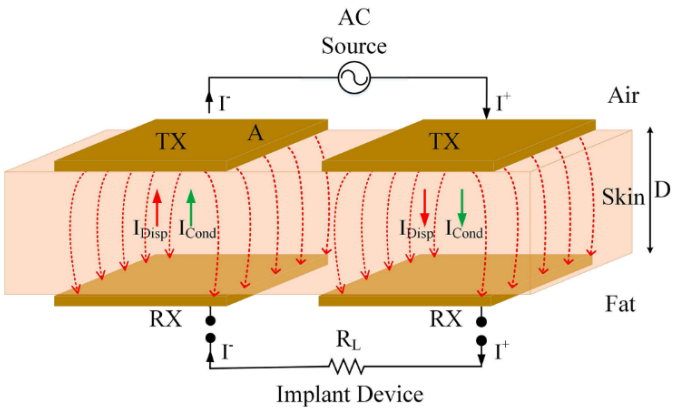

Figure 2.12: Schematic of the capacitive power transfer scheme. An AC signal drives the capacitor plates and the time-varying electric field generates displacement currents that provide energy to the implant device. Figure taken from [56]

When an excitation voltage drives the capacitor plates, a current proportional to the mutual impedance will transfer to the receiver side. The impedance seen by the source is due to the reactance by the

capacitive plates, and its value is proportional to distance. Intuitively, the impedance decreases for a shorter distance, which eventually results in a higher current. Due to the size limitations and the distance between the plates, the effective capacitance is small, limiting the displacement current and hence the power transfer capabilities.

Considering a pair of conductor plates with area A and separation distance D, the displacement current I_{disp} results in response to a time-varying voltage V(t) to accommodate the current continuity. The electric field between the capacitor plates induces the conduction current in the surrounding tissues. The following equations express both currents

$$I_{disp} = \epsilon_r(\omega)\epsilon_0 A \frac{\partial \vec{E}}{\partial t} \tag{2.2}$$

$$I_{cond} = \frac{V(t)\sigma(\omega)A}{D} \tag{2.3}$$

Where ϵ_0 and $\epsilon_r(\omega)$ are the permittivities of free space and the frequency-dependent relative permittivity, respectively and $\sigma(\omega)$ is the conductivity of the medium. The displacement current is the effective way for power transfer to the load and needs to be kept more significant than the conduction current, which accounts for the system losses. Both equations indicate the conflicting parameters that define both currents. This means that increasing the displacement current will also increase the conduction current. Thus, optimization is required to achieve an efficient way for wireless power transfer while considering the application's geometrical and safety constraints.

In CPT, the tissue losses consist of conduction and relaxation losses leading to a significant degradation in power link efficiency. To achieve a high link efficiency, CPT requires a high operating frequency in the order of a few tens of MHz. However, at higher frequencies, their contribution becomes significant compared to IPT. The former is due to the dispersive tissue nature and increases with frequency. Relaxation losses are due to the collision of molecules that occur upon polarization reversal. When the frequency increases, the time it takes for a molecule to polarize is significant, resulting in more collisions and, thus, higher relaxation loss. When the applied alternating electric field matches the relaxation resonance -usually in the low GHz regime-the relaxation loss maximizes. Thus, an optimal operating frequency exists based on the tissue type and thickness. Minimizing the tissue losses is imperative since it contributes to high link efficiency and minimizes the specific absorption rate required for safe operation. The exposure limit is set to $2W/kg$ [56].

Acoustic power transfer

Acoustic power transfer is based on the principle of ultrasound waves to carry energy wirelessly. Unlike the IPT and CPT, APT relies on the medium and its elastic properties. Acoustic waves can carry energy through the tissue to implanted devices, which convert it into electric energy through a transducer. As shown in Figure 2.13, a US system consists of an ultrasound oscillator and two transducers, the oscillator generates an alternating electric field that perturbs the transducer membrane, in turn, converts energy to pressure waves. The frequency range typically used is between 200kHz-1.2MHz. Owing to the low travelling speed in tissue (1500-2000 m/s), the wavelength at this frequency range is small, allowing for miniaturization of the receiver and deep penetration depth. The piezoelectric receiver, RX, is typically placed within the main radiation lobe to tap most of the acoustic energy and convert it back into electrical energy.

The wave directivity depends on the transducer diameter and signals wavelength ratio. Thus, its directivity can change to capture most energy upon changing the transducer diameter. Different excitation techniques have also been reported in the literature to affect the directivity of radiated energy. For instance, Gaussian excitation at a frequency of 650 kHz demonstrated a reduction in side lobes and less variations in the pressure field magnitude within the near field compared to Bessel and uniform transducer excitation [56].

Three loss mechanisms define the power transfer efficiency of APT. The first one occurs due to tissue absorption of travelling waves. In that case, the acoustic wave decays exponentially with the distance, and its intensity over a distance (d) is expressed by the Lambert-Beer law:

$$I_d = I_0 e^{-2ad} \tag{2.4}$$

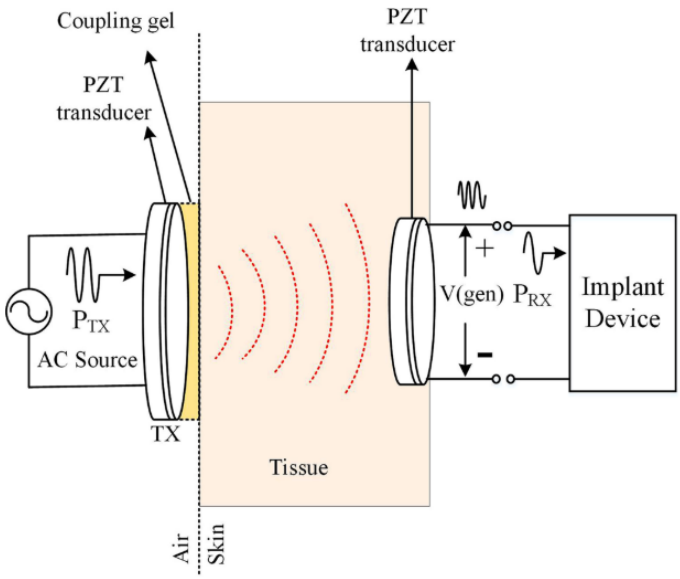

Figure 2.13: Acoustic power transfer schematic. An ultrasound oscillator perturbates the membrane of a transducer, which in turn results in pressure waves. Figure taken from [56]

where I_0 and I_d express the initial and final intensity through a medium with absorption coefficient a expressed in $dB/(cm \cdot MHz)$ for a distance (d). The second loss mechanism is due to PZT conversion losses when acoustic energy converts into electric power and vice versa, this loss depends on the fabrication process. The third loss mechanism is due to impedance variations that the wave undergoes when travelling through different mediums. When a wave propagates through mediums with different acoustic properties, part of the wave energy will reflect in ambiguous directions, as a result of which the transmitted energy reduces. The biggest impedance mismatch occurs at the transducer-skin interface where $Z_{trans} = 31$ MRayls and $Z_{skin} = 2$ MRayls.

The long-term effects on the tissue due to acoustic wave propagation have not been reported, and the maximum intensity approved by the FDA is $7.2\,\mathrm{mW/mm^2}$ for diagnostic applications [56].

Comparison of WPT methods

We discussed three wireless power transfer methods that allow the miniaturization and longevity of a neurostimulator. In particular, we discussed IPT, CPT and APT operation principles. Fig. 2.10 shows that IPT, CPT and APT are the most suitable methods for a miniaturized implant.

Ultrasound can deliver high power at increased penetration depths providing the potential for further miniaturization of the implant. Also, the exposure limit set by SAR allows US transducers to transmit higher power compared to inductive and capacitive power transfers, which are constrained by FDA regulations. On the other hand, APT suffers from poor fabrication and integration on um-sized chips. Besides the potential of APT to provide power in large depths, its efficiency drops in near-field where the pressure field exhibits magnitude variations and makes the power transfer unpredictable. In addition, the acoustic wave needs to travel in the receiver direction, using beam-forming techniques for the energy to get transferred to the implant and mitigate spreading and energy loss. However, this makes the US susceptible to misalignments compared to the other methods.

Capacitive power transfer exhibits advantages in the fabrication and integration process compared to APT, which makes it a low-cost and reliable method for power transfer [54]. It is also less susceptible to misalignment. However, like IPT, this method is susceptible to EM interference. Nevertheless, it can offer high efficiency at small distances, but the plate size should be significant to keep the displacement current high.

Finally, the inductive link is the most used power transfer method. When the system is at resonance, it offers high efficiency and a larger operating distance. However, the efficiency and power demands drop when the receiver coil exceeds the transceiver dimensions. Denisov et al. [58] have compared the efficiency of APT and IPT. In his work, he used equal-sized transmitters and receivers and concluded

that, at small distances, IPT outperforms APT while the opposite holds at increased distances. Similarly, with CPT, the coupled receiver is sensed as a load on the primary side, which makes the transmitter load-dependent. The issues mentioned above can be mitigated using a multi-coil system that makes the system less susceptible to misalignments and less dependent on the load.

The selection of the power transfer method is application-dependent since the advantages and disadvantages of each method are different. For our system, we need to transfer power to two implants within 6-12 mm range since the receiver is implanted transcutaneously. Since their location is on the opposite side of the head, there would be no practical method to transfer energy from a common transmitter without losing excess energy. Therefore the system will consist of two implants powered by their respective transmitters. As shown in [58], the efficiency of IPT at this range is higher. Since the size of IPT does not violate the physical constraints imposed by the application, it seems the best solution for maximizing the system's efficiency.

2.5.1. Fundamentals of Inductive Power Transfer

In near-field inductive coupling, the wavelength at the chosen frequency is much larger than the dimensions of the coil, and time dependencies reduce to a quasi-static model for the magnetic field. That means that the signal applied to the coils is instantaneous at any point of the network, and the uniform magnetic field surrounding the inductance will be almost similar to the magnetic field as if a DC source generated it. In other words, the energy stored in the inductance ($E = 1/2LI^2$) is similar as if it was supplied by direct current. In those cases, the generated magnetic field can couple to remote devices within a distance approximately equal to the transmitter diameter.

When the wavelength of the signal tends to become comparable to the coil size, lumped element theory cannot provide accurate results. That does not mean we cannot use it, but its use requires some adjustments. For instance, at the low MHz range (shortwave radio range 3-30MHz), the current distribution at the wire cross-section changes, manifesting as an impedance variation. The modelling of this effect will be discussed in this section. Furthermore, at wavelengths comparable and lower to the coil size, we can no longer assume the inductance is a purely reactive element since the EM interactions spill over into the radiative Far-field regime and the coil acts as an antenna. Intuitively, that is due to the phase difference between emerging waves relative to other points.

Typical power transfer distances in biomedical applications are in the cm range. The wavelength of a signal that travels through air at 10MHz is approximately 30m. Hence, the transmission distance is orders of magnitude smaller compared to the wavelength, and the electromagnetic field equations reduce to the quasi-stationary expressions. In that case, the fields have low radiation and in the following analysis, the radiation losses are considered negligible and will not be considered.

1.5.1.1. Magnetic Fields

When a current flows through a wire, it generates a magnetic flux density. Assuming that the flow of charges remains constant in time and neither they deplete nor accumulate at any point, we can express the magnetic flux density with Bio-Savarts law [59]

$$B = -\frac{\mu_0}{4\pi} \oint_l \frac{Idl \times e_r}{r^2} \tag{2.5}$$

Where dl is the line vector along the path l and in the direction of current (I), r being the displacement vector from the current line integral to the point where we calculate the magnetic flux with a unit vector e_r and μ_0 is the magnetic permeability in a vacuum.

Typically, the shape of transmitting coils is circular, in which case the magnetic flux density at a point along the x-axis is given as follows

$$B_x = \frac{\mu_0 N I a^2}{2(a^2 + x^2)^{3/2}} e_x \tag{2.6}$$

N being the turns of the coils, I is the time-varying current at each turn, a is the radius of the coil, and x is the coaxial distance with the origin being the centre of the coil, and finally, e_r is the unit vector aligned with the X-axis. If the current varies, it will result in a time-varying magnetic flux density.

1.5.1.2. Induced Voltage on the Secondary Coil

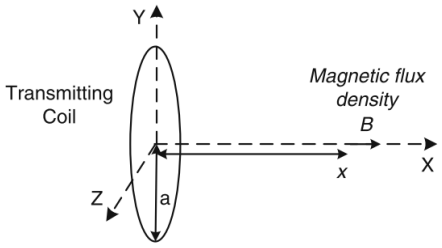

Figure 2.14: The magnetic field generated in response to current flowing in a loop wire. Figure taken from [11]

The time-varying magnetic flux that passes through the coil surface can be expressed as the surface integral of the normal component of the magnetic flux density over that surface.

$$\Phi = \int_{S1} \vec{B2} \cdot \vec{n}\, ds_1 \tag{2.7}$$

Where B_2 is the magnetic flux density generated by the current I_2 and the S_1 is the surface at which we integrate the magnetic flux with a normal vector $\vec{n}$. According to Faraday, when a time-varying magnetic flux is applied to a loop, it produces a voltage which is expressed as follows

$$V(t) = -\frac{d\Phi_m(t)}{dt} \tag{2.8}$$

Where $\Phi_m(t)$ is the time-varying magnetic flux across a coil and $V(t)$ is the time-varying induced voltage on that coil. This induced electromotive force across the secondary coil will generate a current flow that will produce a magnetic field in such a direction that it will oppose the change that produces it. Since voltage and current are applied to the secondary coil, power is transferred to the secondary. This is the so-called Lenz's law.

1.5.1.3. Self and Mutual Inductance

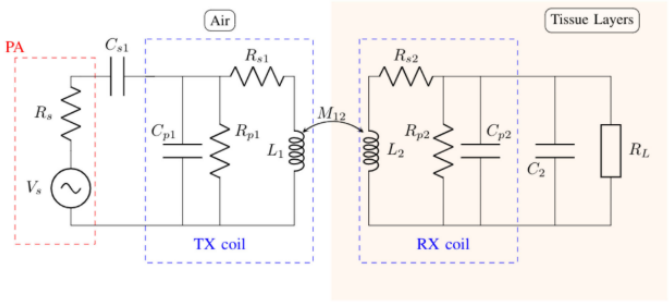

Figure 2.15: IPT Link. Figure taken from [54]

In fact, Lenz's law also applies to a single coil where the change of current will result in an inductive EMF polarized in such a way as to oppose the source that made the current change. This is an interesting coil property and depicts the so-called self-induction effect. The coil inductance L[H] depends on its geometry and scales approximately with the number of turns squared.

$$V = L\frac{di}{dt} \tag{2.9}$$

The mutual inductance, as discussed previously, expresses the link between the magnetic flux and the current generated across another closed path. This relationship is expressed by Faraday's law (2.7). Under the assumption of perfectly aligned, single-turn, circular filaments with radius r_i and r_j, the mutual inductance is given by Neuman's formula in the general case

$$M = \frac{\mu_0}{4\pi} \oint \oint \frac{dl_1 \cdot dl_2}{d} \tag{2.10}$$

The mutual inductance of two parallel, single-turn, circular filaments with radius r_i and r_j, with coil distance d and an offset ρ can be expressed by the following integral

$$M(r_i, r_j, \rho, d) = \pi\mu_0 = \sqrt{r_i r_j} \int_0^\infty J_i(x\sqrt{\frac{r_i}{r_j}}) J_i(x\sqrt{\frac{r_j}{r_i}}) J_0(x\frac{\rho}{\sqrt{r_i r_j}}) e^{(-x\frac{d}{\sqrt{r_j r_i}})} dx \tag{2.11}$$

"Where J_0 and J_1 are the Bessel function of the zeroth and a first order, respectively". This expression assumes that the wire-to-coil ratio (R/r) is negligible and is thus neglected. As a result, the coil radius is not included in this expression.

For parallel coils with perfect alignment, the expression reduces to

$$M(r_i, r_j, \rho = 0, d) = \pi\mu_0 = \sqrt{r_i r_j}\left[\left(\frac{2}{\kappa} - \kappa\right)K(\kappa) - 2\frac{2}{\kappa}E(\kappa)\right] \tag{2.12}$$

where

$$\kappa = \sqrt{\frac{4r_i r_j}{(r_i + r_j)^2 + D^2}} \tag{2.13}$$

and $K(\kappa)$ as well as $E(\kappa)$ are the complete elliptic integrals of the first and second kind.

An approximation of the self-inductance can be derived by the analytical expression (2.12). The expression is accurate only when the wire radius is much larger than the loop radius ($\frac{R}{r} << 1$) and can be approximated by

$$L(R, r) \approx \mu_0 R\left(ln\left(\frac{8r}{R}\right) - 2\right) \tag{2.14}$$

Usually, primary and secondary coils consist of multiple loops that are positioned at the coils' circumference. The total inductance is approximated as the product of the self-inductance and the number of turns squared. However, [60] proposed a coil in which the loops are placed concentric to enhance the coupling coefficient. Thus, a coil consists of turns with different radii. In that case, the inductance of a coil with N terms of radii Ri(i=1,2,...N) can be expressed as in (2.15) with the first term being the sum of the inductance of each turn and the second term being the sum of the mutual inductances between each turn.

$$L_{tot} = \sum_{N}^{i=1} L(R_i, r) + \sum_{i=1}^{i=N} \sum_{j=1}^{j=N} M_{ij}(R_i, R_j, d_r = 0)(1 - a_{i,j}) \tag{2.15}$$

where $a_{i,j} = 1$ for $i = j$, otherwise $a_{i,j} = 0$

This mutual inductance can also be considered as a unitless coupling coefficient k. We do that for practical reasons. For instance, the mutual inductance expression derived by Neuman's [59] is mathematically intractable when it comes to practical coils such as solenoid and disc coils because it has to take into account the number of turns and the shape of coils. Therefore, writing the line elements and the limits of integrations in any simple form is not easy. The following approaches correct this

- N turns: For coils with n_{prim} and n_{sec} turns the mutual inductance is scaled by $n_{prim} \cdot n_{sec}$. Respectively the self inductance L_{prim} and L_{sec} are scale by n_{prim}^2 and n_{sec}^2. The number of turns cancels out when we calculate the coupling coefficient. Therefore, we can use the expressions for the mutual inductance and self-inductance that assumes one-turn coils and calculate the unitless coupling coefficient.

- Coil shape: For the shapes of the coils, the distance between two solenoid coils differs for each turn as compared to a one-turn coil since the solenoid coils extend longitudinally and thus, the

coupling between the last turns becomes weak. This concern raises the question of which distance we should choose between the coils. Similarly, pancake coils increase radially and form an outer and inner radius. Thus, the question is which radius should be used to calculate mutual inductance. Coils shapes are therefore considered by taking the average distance and average radius to calculate the mutual inductance of a one-turn coil. The result is often multiplied by an empirical coefficient to correct errors.

$$k_{12} = \frac{M_{12}}{\sqrt{L_1 L_2}} \tag{2.16}$$

Using line integrals to calculate the mutual and self-inductance can give accurate results. It is, however, computationally inefficient and not practically over many design iterations. Knight [61] also presents a continuous analytical expression for an intermediate length-to-radius ratio solenoid (2.17) based on the current sheet inductance method. Due to the short coil length, the magnetic field cannot be assumed constant. For this reason, Nagaoka's empirical coefficient is used to correct for the magnetic field non-uniformity.

$$L = \frac{\mu_0 \pi r^2 n^2 \kappa}{l} \tag{2.17}$$

where μ_0 is the permeability in vacuum, r the coil radius, n the number of turns and κ the Nagaoka's coefficient as given in [59].

The inductance for PCB coils is given by [62].

$$L = \frac{\mu n^2 d_{avg}}{2}\left(ln\left(\frac{2.46}{\beta}\right) + 0.2\beta^2\right) \tag{2.18}$$

where d_{avg} is the average diameter relative the outer and inner diameter $d_{avg} = (d + d_{in})/2$ and the fill-factor $\beta = (d - d_{in})/(d + d_{din})$.

From the inductance expressions, it is clear that increasing the size can increase the inductance. As a result, the power transfer capabilities of the wireless link can increase. However, this is not as straightforward since an increase in the coil mean geometry will increase the coil resistance. The series loss of a coil consists of three parts:

$$R_{tot} = R_{DC} + R_{skin} + R_{prox} \tag{2.19}$$

Where R_{DC} is due to the resistive loss, R_{skin} is due to the skin effect and R_{prox} is due to the proximity effect. The latter two effects are frequency dependent and appear at the onset of shortwave radio frequencies. First, the skin effect is due to the high-frequency current-carrying components at the edge of the wire cross-section. This non-uniform current distribution results in a drop of the internal inductance modelled as a resistance. Second, the proximity effect resistance models the opposing current generated due to the magnetic field. When the current in each filament flows in the same direction, the magnetic field generated will oppose the current of the nearby filament. This effect becomes prominent when the pitch decreases.

The DC resistance of the coil is a function of the finite resistivity of the conductor and its geometry.

$$R_{DC} = \rho_c \frac{l_c}{A_c} \tag{2.20}$$

where ρ_c is the resistivity of the material, l_c is the length, and A_c is the cross-section of the conductor. The skin effect resistance for a solenoid coil is given by (2.21) and for PCB with a rectangular track is given by (2.22).

$$R_{skin} = \frac{l_c \rho}{\pi(d_0 - \delta)\delta} \tag{2.21}$$

$$R_{skin} = R_{DC} \frac{t_0}{\delta\left(1 - e^{\frac{t_0}{\delta}}\right)} \frac{1}{1 + \frac{t_0}{w}} \tag{2.22}$$

where δ is the skin depth defined in (2.23), d_0 is the wire diameter. Subsequently, t_0 is the PCB track thickness and w is the width.

$$\delta = \sqrt{\frac{2\rho}{\omega\mu}} \tag{2.23}$$

The proximity effect resistance for a single layer solenoid is given by (2.24), where H is the magnetic field experienced by the coil filaments normalised by the coil current I_0. Eq. (2.25) is an approximation that defines the proximity effect resistance for PCB coil.

$$R_{prox} \approx 2R_{DC}\pi^2\rho_0^2\left(\frac{2\rho}{\delta} - 1\right)\frac{H^2}{I_0^2} \tag{2.24}$$

$$R_{prox} = \frac{R_{DC}}{10}\left(\frac{\omega}{\omega_{crit}}\right)^2 \tag{2.25}$$

The critical frequency is when the current distribution along the conductor starts to become non-homogeneous.

$$\omega_{crit} = \frac{3.1}{\mu_0}\frac{(w+s)\rho}{w^2 t_0} \tag{2.26}$$

1.5.1.4. Inductive coupled coils

The previous section explained the self- and mutual-induction effects. In inductive coupled links, both effects act simultaneously at each coil. Therefore the emf of each coil is a result of two contributions: one by the coil current itself and one by the mutual inductance of the coupled coil. Thus, the equation for an inductive coupled link is given by

$$\begin{bmatrix} V_1 \\ V_2 \end{bmatrix} = \begin{bmatrix} L_1 & M \\ M & L_2 \end{bmatrix}\begin{bmatrix} \frac{di_1}{dt} \\ \frac{di_2}{dt} \end{bmatrix} \tag{2.27}$$

Those are the equations that constitute the transformer basis. Transformer coils are brought close to each other, and a bulky ferromagnetic material is often placed along the coils. Its properties enhance the magnetic field and provide a low reluctance path to the magnetic flux. As a result, the coupling coefficient is close to 1, and the efficiency is approximately equal to 100%. However, achieving high coupling at increased distances usually required in implantable biomedical devices is impossible, especially when geometrical constraints make using ferromagnetic materials impractical.

As explained before, real inductors are modelled with a series resistor that is a function of frequency. At the low MHz frequency, this resistance is not negligible. Therefore, the ability of the inductor to store energy is defined by the quality factor.

$$Q = \frac{\omega L}{R} \tag{2.28}$$

In other words, it expresses the energy loss as a proportion of inductor reactive impedance. An inductor with an infinite quality factor can store its energy indefinitely since the series resistor is infinitely high. In this case, there is no energy dissipation. This parameter will be used for the PDL and PTE analysis.

1.5.1.5. Resonant Inductive Topologies

Resonant arrangements increase energy transfer efficiency compared to non-resonant arrangements. Resonant tuning is done by connecting a capacitor in series or parallel with the transmitter coil. In a resonance topology, the energy that becomes available is stored and oscillated between the reactive elements until it is coupled to the secondary circuit. However, the non-ideal inductors dissipate energy across the coil resistance.

The tuning capacitor is placed in series or parallel with the capacitor. Thus, a wireless power transfer link has four different topologies. The topology selection should match the driving circuit or the load, which depends on the application. The resonant topology selection is addressed in the literature, but they draw different conclusions [57] [63]. In essence, parallel resonance offers high impedance, so they

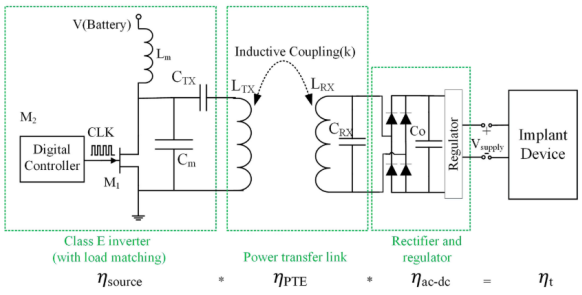

(a) A typical series to parallel wireless power transfer with the corresponding circuitry. Image taken from [56]

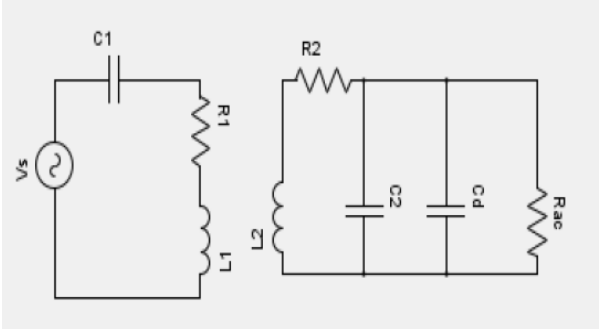

(b) An AC series-to-parallel power transfer link model with the including the inductor losses, parasitic capacitance of the rectifier and the AC equivalent model.

should be chosen when connected to a high-impedance load or when a circuit drives them with a high output impedance that behaves like a current source. Alternatively, for a series-resonance topology, the load impedance should be small, and the driving circuit should have a low output impedance and behaves like a voltage source. In that sense, the resonance of the tank is not damped, and energy is transferred efficiently. Due to low power dissipation, implantable biomedical devices have a high output impedance. This is why the parallel topology is often used on the receiver side [64] [65]. On the other hand, class-E or class-D amplifier drives a series resonant coil on the transmitter side to achieve impedance matching.

Fig. 2.16a show a typical system level diagram of a wireless power transfer link. The link consists of a series-to-parallel resonant topology. At the transmitter side, a class-E amplifier induces power to the system. Power is rectified and regulated at the receiver side to supply a constant voltage to the implant. Fig. 2.16b shows the equivalent AC model of the power transfer link. It includes the coil series resistances R_1 and R_2, C_d accounts for the rectifier added capacitance and R_{ac} is an equivalent AC resistance. Its value should represent the power dissipation that happens in the load, and the circuitry employed given by

$$R_{ac} = \frac{V^2}{P_{electronics} + P_{load}} \tag{2.29}$$

$P_{electronics}$ represent the power dissipation that occurs in the AC-DC conversion and P_{load} is the power dissipation that happens in the load.

1.5.1.6. Analysis of the Inductively coupled link

After we have discussed the conversion of geometrical to electrical parameters and presented the AC model of the link, we can analyse the link impedance to give insight into the PTE and PDL. The most fundamental principle in an inductively coupled coil is that the current induced in the secondary through mutual inductance is sensed as a series reflected impedance connected on the primary side, given by (2.30). Intuitively, the value of this impedance relative to the coil resistances and the coupling will define how much energy is consumed on it. Subsequently, we will provide the expression that gives a clear view of the inductive coupled link dynamics and the optimal performance we can achieve.

$$Z_{refl} = \frac{(\omega M)^2}{Z_s} \tag{2.30}$$

Where Z_s is the impedance of the secondary coil as seen by the induced EMF. In Kirchhoff's voltage law, this voltage is expressed as

$$E_{ind} = -j\omega M I_1 = I_2 Z_s \tag{2.31}$$

The principle of induced voltage on the secondary is illustrated in Fig. 2.17. Then, applying Kirchhoff's voltage law at the circuit in Fig 2.16b, we can obtain the equations that describe the interactions between the two loops (2.32).

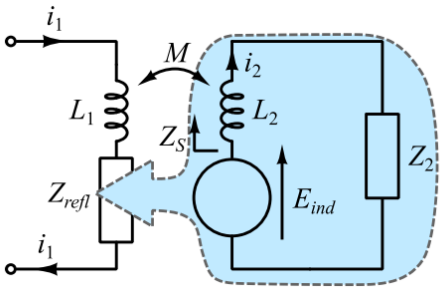

Figure 2.17: Lumpled element circuit model illustrating the concept of secondary induced voltage and the reflected impedance. Figure taken from [62]

$$\begin{bmatrix} V_1 \\ 0 \end{bmatrix} = \begin{bmatrix} R_1 + j\omega L_1 + \frac{1}{j\omega C_1} & j\omega M \\ j\omega M & R_2 + j\omega L_2 + \frac{1}{j\omega C_2} \end{bmatrix} \begin{bmatrix} I_1 \\ I_2 \end{bmatrix} \tag{2.32}$$

From this matrix, we can derive a useful expression for the link impedance, voltage transfer function and efficiency of the system. Taking the inverse of the matrix in (2.32) we can express the currents of the two loops as in (2.33)

$$\begin{bmatrix} I_1 \\ I_2 \end{bmatrix} = \frac{1}{Z_1 Z_2 + \omega^2 M^2} \begin{bmatrix} Z_2 & -j\omega M \\ -j\omega M & Z_1 \end{bmatrix} \begin{bmatrix} V_1 \\ 0 \end{bmatrix} \tag{2.33}$$

Taking the ratio of the input voltage and current gives the input impedance as seen by the driver, which confirms (2.30).

$$Z_{input/link} = Z_1 + \frac{(\omega M)^2}{Z_2} \tag{2.34}$$

2.5.2. Power Transfer Efficiency of an Inductive Link

The power conversion efficiency of the inductive link is an important metric. Maintaining a high efficiency means that most of the power sent from the transmitter is delivered to the load. Even if we achieve increased power transfer capabilities, this does not ensure efficient power transfer. Nevertheless, the efficiency is limited to below 50% when the maximum power theorem is satisfied. It was discussed in the previous subsection that, in practice, coils are subjected to losses due to the proximity and skin effects and tissue losses. We will now discuss, in more detail, the effect of transmitter-receiver mismatch and that of loose coupling. It is often argued that loose coupling is related to low efficiency. However, the coupling coefficient defines the rate of energy transfer and not the efficiency. On the other hand, the lossy parts of the system relate to efficiency. Therefore, in a loosely coupled system with high Q-coils, even if the energy transfer rate is low, the energy will be stored at the primary.

Fig 2.18 illustrates the power path of an inductive power transfer link from an external power source to the implanted load. The system consists of a battery-powered Power Amplifier (PA) that conveys energy to the primary coil, which is coupled to the receiver by inductive coupling. The received energy is rectified and then regulated by a switched-mode power converter or a linear drop-out regulator to connect directly to the tissue or a current source. Fig. 2.18 illustrates the energy loss that takes place along the entire power transfer path. The total efficiency of the system is the product of each stage which is expressed as follows:

$$\eta_{total} = \eta_{PA} \times \eta_{link} \times \eta_{AC-DC} \times \eta_{DC-DC} \times \eta_{NS} \tag{2.35}$$

Where η_{PA}, η_{link}, η_{AC-DC}, the η_{DC-DC}, and η_{NS} are the efficiencies of the power amplifier, the inductive link, the AC-DC converter, DC-DC converter and the neurostimulator respectively. The link efficiency η_{link} consists of the following product $\eta_1 \times \eta_{trans} \times \eta_2$, while the load efficiency, η_L represents losses of the implanted circuitry given by the product of each circuit efficiency $\eta_{AC-DC} \times \eta_{DC-DC} \times \eta_{NS}$. Implantable biomedical devices with a high link efficiency translate to less heat dissipation, hence less

tissue-related adverse effects. Since the power demands of the implant are satisfied with lower transmitted power, it offers better compatibility with the EM exposure standards.

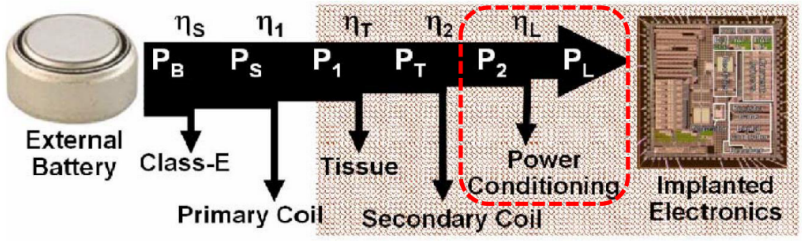

Figure 2.18: Power transfer flow from the external battery to the tissue. Figure taken from [53]

There have been many different approaches in order to optimise total efficiency. Primarily, we can divide them into three categories. The first one involves the design of the power amplifier for efficient energy transmission. In inductive power transfer, the attention is focused on the design of class-D or -E [66] [67]. However, we do not discuss this approach in this literature review. Secondly, it involves the optimisation of link efficiency. The literature on this topic is extensive and includes coil design, theoretical analysis and coil optimization [68] [69] [70] [53] [71] [57]. Since the inductive link is the interface where the implant receives its energy, we will review the fundamental principle of the link to understand what is essential to keep in mind to maintain high efficiency (i.e. topology, optimal load condition, frequency of operation). The final approach involves optimising the rectifier, and regulator [72] [73]. In the literature, all these sections are researched individually. However, we will observe next that a holistic approach to the system is critical for high system efficiency.

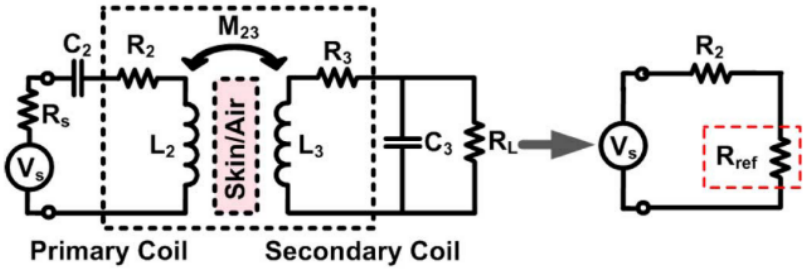

Figure 2.19: Two-coil inductive coupled coils for wireless power transfer and the equivalent circuit at resonance. Figure taken from [74]

Theory of Two-Coil Inductive Link Fig. 2.19 shows a two-coil resonant inductive link. The system consists of a source V_s, two coils L_2 and L_3, and the load. The source supplies energy to the secondary coil coupled due to the mutual inductance of the coil pair (M_{23}). A part of this coupled energy splits between R_3 and R_L. The system is tuned with two capacitors at the source driving frequency $f_0 = 1/(2\pi\sqrt{L_2C_2}) = 1/(2\pi\sqrt{L_3C_3})$ to boost the efficiency. Due to the energy coupling, the secondary circuit is sensed as a load on the primary side. For that reason, it is modelled as a reflected impedance in series with the power supply given by

$$R_{Ref} = k_{23}^2 R_2 Q_2 Q_{3L} \tag{2.36}$$

where k is the quality factor shown in (2.16), $Q_2 = \omega_0 L_2/R_2$ is the unloaded quality factor of the transmitter, and $Q_{3L} = Q_3 Q_L/(Q_3 + Q_L) = R_P/\omega_0 L_2$ is the quality factor of the receiver. $Q_L = R_L/\omega_0 L_3$ is the load quality factor, R_P is the parallel equivalent impedance of the coil ac resistance, and the load $(R_{P3}R_L)/(R_{P3} + R_L)$, where $R_{P3} = Q_3^2 R_3$ is the parallel transformation of the series coil resistance. The reactive components cancel each other at the resonance frequency, and the circuit is simplified, as shown in Fig. 2.19. For the subsequent analysis, the impedance R_2 incorporates the output impedance of the power source, R_s. The efficiency is given by the power division between R_2 and R_{ref}. The power

that dissipates at R_{ref} is the transmitted power that divides between R_{p3} and R_L. Therefore, the effective power that eventually ends up in the load can be expressed by the following potential divider expression [75].

$$\eta_{2-coil} = \frac{R_{ref}}{R_2 + R_{ref}} \frac{R_{p3}}{R_{p3} + R_L} = \tag{2.37}$$

$$= \frac{k_{23}^2 Q_2 Q_{3L}}{1 + k_{23}^2 Q_2 Q_{3L}} \frac{Q_3}{Q_3 + Q_L} \tag{2.38}$$

This analysis ignores any losses to the surrounding medium. Nevertheless, at the low MHz range, the tissue dissipation mechanisms are usually considered negligible [66]. In both (2.37) and (2.38) the first terms express the power division between R_2 and R_{ref} (primary-secondary efficiency, $\eta_1 \times \eta_{link}$) and the second term expresses the power division between the parallel parasitic resistance R_{p3} and R_L (secondary efficiency, η_2). In (2.38), the link efficiency is expressed in terms of the coils' coupling coefficient and quality factors. From (2.38), we observe that increasing the load quality factor has the opposite effect on the efficiency of each part. Depending on the quality factor, an optimum load exists that we will discuss next.

Since the efficiency is the ratio between load power and the power delivered by the source, we can express the power delivered to the load (PDL) by multiplying the efficiency with the power available from the source $P_s = V_s^2/(R_2 + R_{ref})$

$$P_{L,2-coil} = \frac{V_s^2}{2R_2} \frac{k_{23}^2 Q_2 Q_{3L}}{(1 + k_{23}^2 Q_2 Q_{3L})^2} \cdot \frac{Q_3}{Q_3 + Q_L} \tag{2.39}$$

Optimum load condition: Intuitively, the efficiency will increase in (2.38) if the unloaded quality factors (Q_1, Q_2) increase since unwanted coil losses reduce. The equation also implies that coupling enhances efficiency. However, this is quite misleading since the coupling defines the energy exchange between the coils, not the energy dissipation mentioned previously. In essence, if the coils are lossless, the coupling would not increase efficiency.

Finally, the load quality factor (Q_L) has the opposite effect on the primary-secondary and secondary efficiency. Increasing its value will increase the primary-secondary efficiency since the reflected resistance will increase and more energy will couple to the secondary. However, in that case, the efficiency of the secondary coil decreases since energy starts to dissipate more at the secondary coil losses. Therefore, there is an optimum load $R_{L,PTE} = \omega_0 L_2 Q_{L,PTE}$ for a given coil pair and coupling that extracts most of the energy from the resonant tanks. We derive $Q_{L,PTE}$ by differentiating (2.38) with respect to Q_L.

$$Q_{L,PTE} = \frac{Q_3}{\sqrt{(1 + k_{23}^2 Q_2 Q_3)}} \tag{2.40}$$

Alternatively, to maximize PDL, we can find the reflected impedance that will match the primary coil resistance ($R_2 = R_{ref}$) for a certain k_{23}. This condition will limit the link efficiency to less than 50% since half of the power will be dissipated in the primary coil resistance. We can find the maximum load $R_{L,PDL} = \omega_0 L_3 Q_{L,PDL}$, by taking the derivative of (2.39) with respect to Q_L

$$Q_{L,PDL} = \frac{Q_3}{1 + k_{23}^2 Q_2 Q_3} \tag{2.41}$$

Alternatively, the critical coupling $k_{23,PDL}$ is often reported in the literature. It is the value at which R_{ref} becomes equal to R_2 to satisfy the maximum power transfer condition. The following equation provides this value

$$k_{23,PDL} = \frac{1}{\sqrt{Q_2 Q_{3L}}} \tag{2.42}$$

Each condition is satisfied with a different set of coupling and electrical parameters. Thus, we can conclude that we cannot satisfy the maximum PTE and PDL conditions simultaneously, which also

becomes apparent from (2.38) and (2.39). Moreover, PTE and PDL are strongly dependent on the linear load impedance. We will notice next that the circuit presents a time-varying load, and often the pick-up circuits exhibit non-linearities that, in reality, are modelled with a linear resistor. Additionally, the application predefines the implant load (R_L), which could differ from the optimal link loading.

Multiple techniques have been proposed in different parts of the system power flow to mitigate this issue, as shown in Fig. 2.20. Firstly, multiple coils have been proposed to accomplish an optimum condition for PTE and PDL. This approach can perform an impedance transformation by adjusting the coupling between the relay coils relative to the driver and load coil. Secondly, a tuning system and Q-modulation techniques are used to fix the system at optimal load conditions. Last but not least, novel architectures for power management are employed that adapt to optimal conditions for efficient operation. Next, we will review some of these methods provided in the literature.

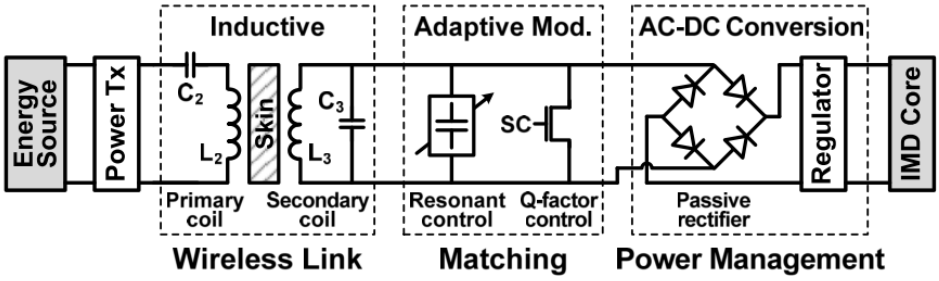

Figure 2.20: Multiple techniques that are employed in the power flow of a system to increase efficiency. Figure taken from [76]

2.5.3. Impedance Transformation

As already indicated, load matching improves the performance of the inductive resonance. That means energy is efficiently extracted by the resonance tank while avoiding dissipation in coil losses. The load, however, is defined by the application. Therefore, it could be different by the optimal load for the resonance link or dynamically change over time to eventually deteriorate the efficiency. In order to compensate for these changes, impedance matching techniques are used that sustain good resonance coupling.

The multi-coil approach provides a broader range for load matching, where relay coils are used between the primary and secondary coils. Their coupling with the main coils gives additional freedom to optimize PTE and PDL. Other works have proposed impedance matching circuits by using additional reactive components.

1.5.3.1. Multiple coils

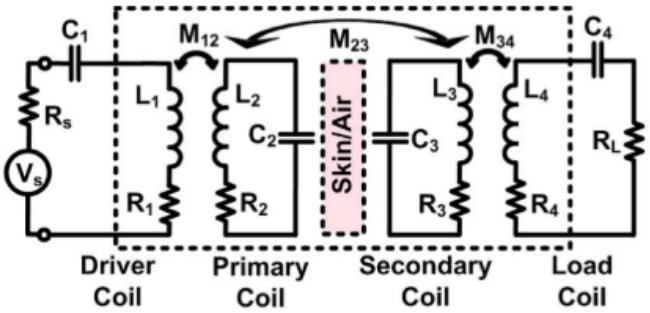

Figure 2.21: Circuit model of 4-Coil wireless power transfer inductive link. Figure taken from [74]

Four-Coil Power Transfer Inductive Link: [77] [78] proposed a four-coil inductive link that obtains high efficiency for an increased power transfer range. However, they emphasized the design of high

quality-factor coils that make them susceptible to displacements. Sample et al. [79] has proposed an asymmetric four-coil link consisting of two identical driver and load coils, as well as the primary and secondary coils with the same quality factor. The coupling between the loop coils with the primary and secondary coils was used as a lever to maximize the power transfer range. Decreasing the loop coupling would decrease the power transfer range at the expense of efficiency. The link operates at the so-called over-coupled regime if k_{23} value is above critical coupling. In this area, the resonance of the system shift due to a phenomenon called frequency splitting. For this reason, an adaptive frequency technique can be used to tune the system back into resonance. Ramrakhyani et al. [80] have also presented a four-coil link with high-Q Rx and Tx coils that obtains high efficiency and better displacement resilience. Kiani et al. [74] provided an analysis of a four-coil inductive link that shows an increase in PTE compared to a two-coil link but fails to obtain high PDL.

In the following analysis, we provide the expressions for PTE, (2.43), and PDL, (2.44). Essentially, the rationale is the same as for the two-coil link. The load impedance reflects to each coil, and for each of these coils, we calculate the delivered power until it reaches R_L [74]. To simplify the expression, we neglect coupling between distant coils (k_{13} k_{14} and k_{24}) since their effect is negligible to the overall system performance.

$$\eta_{4-coil} = \frac{(k_{12}^2 Q_1 Q_2)(k_{23}^2 Q_2 Q_3)(k_{34}^2 Q_3 Q_{4L})}{[(1 + k_{12}^2 Q_1 Q_2) \cdot (1 + k_{34}^2 Q_3 Q_{4L}) + k_{23}^2 Q_2 Q_3] \cdot [1 + k_{23}^2 Q_2 Q_{3L} + k_{34}^2 Q_3 Q_4]} \cdot \frac{Q_{4L}}{QL} \tag{2.43}$$

$$P_{L,4-coil} = \frac{V_s^2}{2R_1} \frac{(k_{12}^2 Q_1 Q_2)(k_{23}^2 Q_2 Q_3)(k_{34}^2 Q_3 Q_{4L})}{[(1 + k_{12}^2 Q_1 Q_2) \cdot (1 + k_{34}^2 Q_3 Q_{4L}) + k_{23}^2 Q_2 Q_3]^2} \cdot \frac{Q_{4L}}{QL} \tag{2.44}$$

Fig. 2.22 shows the plotted values of PTE and PDL as a function of k_{12}, k_{23} and fixed k_{34} to maximize PTE. The 4-coil Inductive link gives an additional degree of freedom on the drive side with k_{12}. When its value is large, the reflected impedance on the driver coil increases dramatically, maximising the PTE. Moreover, as shown in Fig. 2.22a, the PTE obtains better tolerability to coupling variations between the primary and secondary coil. However, the increased reflected impedance caused by k_{12} drastically reduces PDL. That is obvious in Fig. 2.22, where the high overlap values are limited at a certain range.

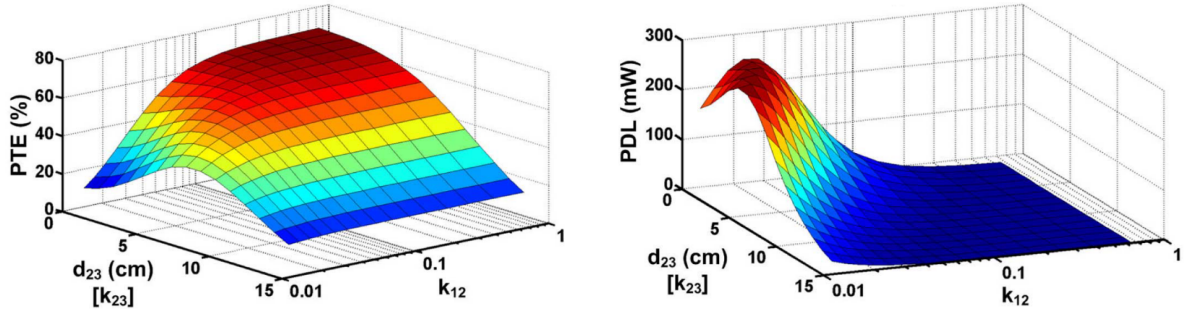

(a) (b)

Figure 2.22: (2.22a) Power Transfer Efficiency (PTE), and (2.22b) Power Delivered to the Load (PDL), of a 4-Coil Inductive link for varying coupling coefficients k_{23}, k_{12} and $k_{34} = 0.22$. Simulation from [74]

Three-Coil Power Transfer Inductive Link: Fig. 2.23 shows the 3-Coil inductive link that consists of L_2 coil on the transmitter side and coils L_3 and L_4 on the receiver side. k_{34} can be used for impedance matching to transform any load to the optimal impedance that maximizes PTE [74]. This is in contrast to the 2-coil link that with a given set of L_2, L_3, and k_{23} maximum PTE can be achieved only with the optimal load value $R_{L,PTE}$ which can also differ from the application-specific R_L.

The expressions for PTE (2.45) and PDL (2.46) are provided, neglecting k_{24} due to its negligible effect

$$\eta_{3-coil} = \frac{(k_{23}^2 Q_2 Q_3)(k_{34}^2 Q_3 Q_{4L})}{(1 + k_{23}^2 Q_2 Q_3 + k_{34}^2 Q_3 Q_{4L})(1 + k_{34}^2 Q_3 Q_{4L})} \cdot \frac{Q_{4L}}{Q_L} \tag{2.45}$$

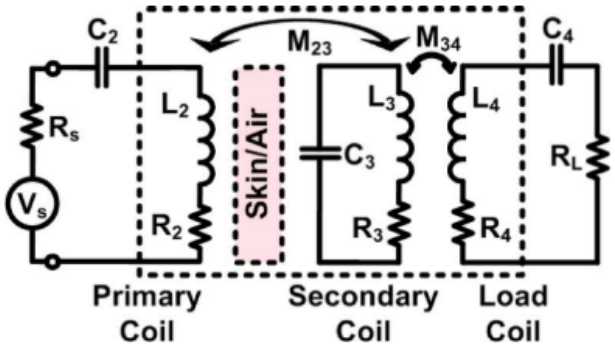

Figure 2.23: Circuit model of a 3-Coil power transfer inductive link. Figure taken from [74]

$$P_{L,3-coil} = \frac{V_s^2}{2R_2} \frac{(k_{23}^2 Q_2 Q_3)(k_{34}^2 Q_3 Q_{4L})}{(1 + k_{23}^2 Q_2 Q_3 + k_{34}^2 Q_3 Q_{4L})} \cdot \frac{Q_{4L}}{Q_L} \tag{2.46}$$

Both PTE and PDL are plotted in Fig. 2.24 as a function of k_{23} and k_{34}. In contrast with the 2-coil and 4-coil links, the 3-coil counterpart can be optimized for both PTE and PDL by choosing the right k_{23} and k_{34}.

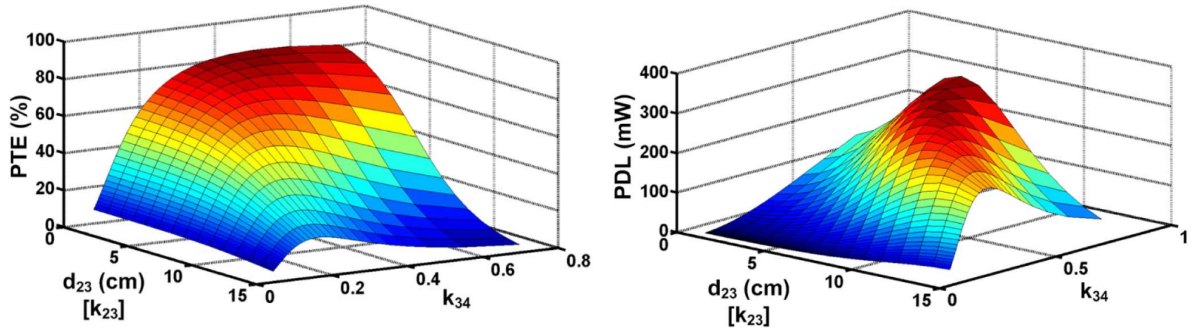

(a) (b)

Figure 2.24: (2.24a) Power Transfer Efficiency (PTE), and (2.22b) Power Delivered to the Load (PDL), of a 3-Coil Inductive link for varying coupling coefficient k_{23}, k_{34}. Simulation from [74]

Multiple coils provide a degree of freedom to transform any load to the optimal loading utilizing the coupling coefficient between the additional coils. However, this is a static approach and the load R_L can change significantly during operation. After coil fabrication and implantation, it is practically impossible to adjust the mutual coupling and geometry of the coil. Moreover, due to additional coils, the size and complexity of the implant are increased.

1.5.3.2. Load Matching Circuits

In order to increase the efficiency, previous studies have focused on improving the k-factor and Q to obtain $k^2 Q_1 Q_2 >> 1$ that will eventually result in 100% theoretical power transfer efficiency while neglecting the importance of loading [11]. However, the theoretical maximum can be reached only with an optimal impedance. For instance, in the resonant inductive coupling, the parallel capacitor C_2 only matches the reactive element of the link input impedance, leaving the real components unmatched. That is why the power transfer efficiency approaches the theoretical maximum for a small range of R_L and declines when the value is either too small or too large. Therefore, the load matching networks accomplish to maintain the resonance in the secondary circuit and transform the load to the real value.

Xue et al. [81] and Silay et al. [82] proposed an L-transformation structure by using an extra inductor and capacitor that resonates along with L_2 but also transforms the impedance. Therefore, the

impedance network does not dampen the resonance and sustains the load power transfer. Moreover, it also makes the link less susceptible to coupling and load variations while the efficiency remains high and the driving requirements for the source remain low. Finally, Martins et al. [83] presented an efficiency analysis and optimization of a multistage matching network. This paper considers a complex source and load impedances, unlike previous works.

Besides the benefit of providing the optimal load on the inductive link, impedance matching networks require additional components. Due to the operation frequency, the reactive components need to be large and off-chip. Additionally, they add losses, and as a result, they compromise efficiency.

2.5.4. Adaptive Circuits

We have already stressed the importance of optimum loading for efficient inductive power transfer. Multi-coil and impedance matching networks are two static techniques that implement load transformation. However, the reactive components will be off-chip at the low MHz range due to their size. High efficiency requires high-Q coils that come at the expense of increased size. Following the fabrication phase, it is no longer possible to modify the circuit, which is not in our favour, given that the implantable devices are exposed to a dynamic environment that can change the electrical characteristics of the coils. Also, variations in load impedance and coupling can lead to non-optimal operation

These changes can have an impact on both PTE and PDL. Responding to variations to keep the power and the impedance optimal ensures the correct IMD operation and decreases the unwanted RF exposure and heat dissipation in the implant that could otherwise lead to tissue damage. For that purpose, closed-loop systems are employed that can obtain high efficiency and constant input power in response to coupling and loading variations. Very broadly speaking, these techniques perform impedance transformation by changing some of the circuit characteristics. Subsequently, we classified some methods into four divisions: Frequency compensations circuits, Q modulation techniques, Switched-mode converters, and closed-loop power regulation circuits.

1.5.4.1. Frequency splitting adaptive systems

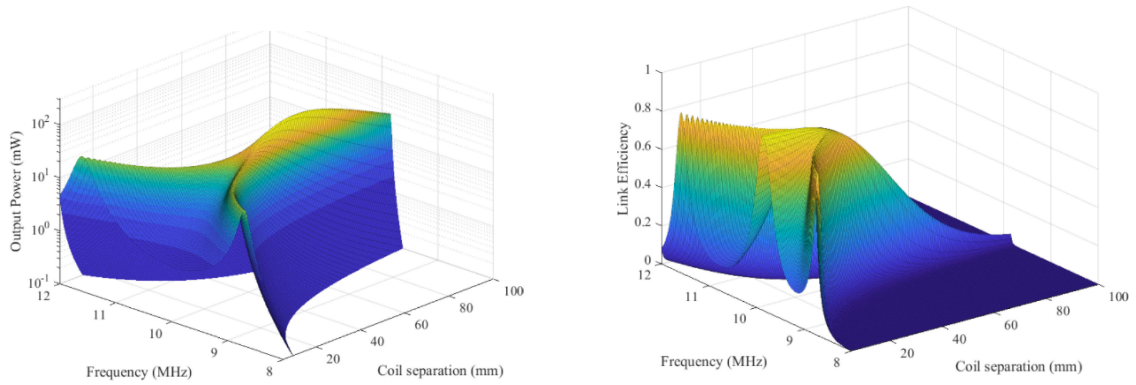

(a) (b)

Figure 2.25: Frequency splitting impact on PTE for a series to series (SS) resonant topology. Figure taken from [62]]

We have seen that power transfer efficiency and voltage gain increase when the transmitter and receiver are tuned at the same resonance under loose coupling conditions. In essence, tuning the coils at the same resonance frequency cancels the reactive component of the mutual inductance, and the reflected impedance appears real. However, as the distance between the coils decreases, the reactive component of the reflected impedance increases, which manifests itself as the frequency splitting phenomenon, in which the optimum resonance splits into a lower and higher frequency [63], [84], [85] [86]. The effect can be observed by plotting any link parameter as a function of frequency and distance. Fig. 2.25 shows simulated values for both PTE and PDL as a function of frequency and distance for perfectly aligned coils assuming a series-to-series topology. While it is possible to obtain high PTE and PDL at the resonance frequency of 10MHz, their peak value shifts due to the frequency splitting at

separations smaller than 40mm. As a result of distance variations, PTE and PDL will undergo dramatic changes if the circuit operates at a fixed frequency. It is, therefore, imperative to design adaptive tuning circuits for systems that could operate in the over-coupling regime to maintain high efficiency and keep the power level constant in the implant [87].

Some adaptive systems have been proposed to track the optimum resonance frequency by adjusting the inductance [88] or the capacitance [89] [32] [90] of either the primary or secondary LC tank. This method is convenient for correcting frequency deviations resulting from tissue- and encapsulation-related parasitic capacitance. Additionally, the electrical characteristics of the LC tank undergo significant changes due to implant deformations that eventually detune the link off-resonance [71]. However, the coil taps and the size of the capacitor bank array should be large to provide adequate resolution and increased frequency range. If the variable tunning network cannot accurately track the frequency, it compromises the efficiency rather than increasing it. Therefore, this technique is a tradeoff between size and accuracy. The accuracy, however, is prone to component variations that put an upper limit on the tracking resolution. Moreover, when the components disconnect from the tank, they discharge the resonant energy resulting in some energy loss [91].

An alternative approach compared to these methods is to compensate for the frequency variations by changing the frequency of the transmitter [92]. This method works by monitoring and correcting the phase difference between the power amplifier driving signal and the LC-tank voltage in response to coupling and loading variations. The difference depends on the load impedance of the power amplifier, considering that it can change from resistive to reactive depending on the resonance status of the link. When it operates in resonance, the reactive components cancel out, presenting a purely resistive load to the power amplifier.

Schormans et al. [93] employed a phase tracking technique that drives the system at an optimum frequency that compensates for coupling and load changes. It does so by monitoring the phase difference between the PLL voltage signal that drives the power amplifier and the voltage in the primary tank. Considering resonance conditions, the impedance seen by the power amplifier is resistive, presenting no phase difference between the driving and primary voltage signals. If there is a phase shift, the circuit is off-resonance, and thus a phase shift is presented between the two signals. Thus, the closed-loop detects and corrects any phase difference. However, this circuit ran under the supervision and did not perform fully autonomously. In [94], Schormans presented an active compensation circuit based on the optimum frequency tracking method, in which he included an additional loop that compares the primary voltage level with an offset voltage. If the primary voltage is higher than the offset voltage, the link is at resonance and the voltage is high owing to the high voltage gain characteristics of the resonant link. Unlike the other methods that use additional components to tune the coils back to resonance, the tracking system requires only a variable frequency synthesizer. One obvious advantage of this method is that the area of the receiver decreases if the system does not adopt a tuning component network. Conversely, the transmitter can become more compact by integrating the variable frequency synthesizer. Finally, frequency tracking systems measure the phase difference of the signals at the transmitter side. Unlike other methods, they do not need a communication unit to transfer data from the receiver.

1.5.4.2. Q-Modulation

Q-modulation is another technique that performs impedance transformation. Fig. 2.26 shows a typical lumped circuit model of a series-to-series resonant link where a switch is placed parallel to the load. By changing the duty cycle of the switch, the effective load of the circuit changes as well. The intuitive explanation is that when a load connects to a series resonant topology, it dampens the resonance, and the energy is not delivered to the load effectively. Therefore, by closing the switch, the current is free-wheeling in the LC tank, and energy builds up. When the switch turns off, the energy discharges to the load. Kiani et al. [95] proposed a circuit whose topology and operation are shown in Fig. 2.26. the switch closes for a period T_{on} at each zero-crossing of I_3. Once the switch is closed during Φ_1, the resonance of the LC-tank builds up, increasing the quality factor and capturing most of the energy sent by the transmitter. During Φ_2, the switch opens, and the LC-tank releases its stored energy to the load R_L. In that way, the system modulates the load to $R_{L,eq}$ to keep the efficiency of the system constant [95].

However, the switch must turn on twice within a cycle of the driving signal, and the timing must be accurate, not compromising efficiency. A sophisticated synchronization circuit is required to provide

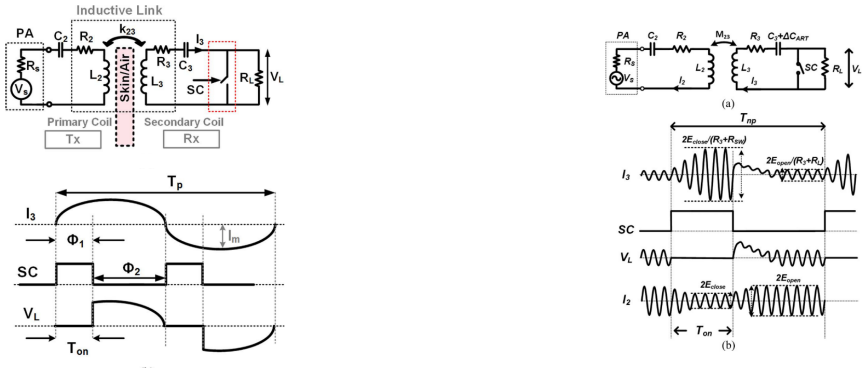

Figure 2.26: Q-Modulation technique to perform impedance matching. (2.26a) a system proposed by [95] that samples the current within a fraction of a cycle, and (2.26b) a system proposed by [96], SC switch samples the current for many cycles of the driving frequency.

accurate switching times and a clock signal that runs a few hundred times higher than the driving frequency to provide an acceptable resolution. Lee et al. [96] proposed a Q-modulation technique that switching takes place over multiple cycles eliminating the need for a sophisticated synchronization mechanism to control the zero-crossing switching. The system has also incorporated adaptive Rx resonance tuning to ensure that the LC tank remains at resonance. Combining both methods will ensure that the PTE remains at its peak while also dynamically adjusting the load. It is crucial for both Q-modulation methods that the switch resistance is low because it adds up to the loss of the Q-modulation system and degrades the efficiency.

Both designs work for a series resonant topology used to power lighter loads. The power requirement for a neurostimulator is usually a few mW which translates to an impedance of a few hundred ohms. In that case, a parallel resonance is appropriate to match the load. Although the rectifier introduces the concept of periodic switching that fluxes energy from the resonance tank to the load, the literature needs studies that assess the resonance build-up phenomena in parallel resonance topologies.

1.5.4.3. Switched DC-DC Converters for impedance transformation:

The following methods take advantage of the conventional topology for the power conversion of inductive energy rather than using additional circuitry. Instead, they adjust the duty cycle of switched-mode converters to perform impedance transformation. In that way, the inductive power transfer system presents the optimum load to the link to obtain maximum PTE and provide a fixed voltage supply in response to load and coupling variations. In [97], Pantic proposed a novel tristate boost converter to compensate a parallel resonant topology. Unlike conventional boost converters, this one has an additional switch that forms a loop around the inductor that turns on after the typical periods of current boost and power delivery to the load. The freewheeling period emulates an additional reactance. In this way, the tristate converter tunes to the resonant frequency, besides controlling the effective impedance.

Ahn et al. [98] did not consider the system as two different voltage conversion stages but analyzed them in conjunction. For instance, in inductive power transfer, it is encountered that the first stage provides an unregulated DC voltage, while in the second stage, a buck-boost converter converts the voltage ratio of D/(1-D) [99] [66]. Unlike this narrative, Ahn supports that we can modulate the load by letting the resonant current or voltage build up in the LC tank, depending on the topology. This is done when the first switch opens and disconnects the converter from the rectifier. Therefore, adjusting its duty cycle modulates the effective resistance and conveys more energy at the resonance tank, as shown in Fig. 2.27b. Although the system can adjust its duty cycle for coupling variations, it cannot correspond to load changes. In that case, the optimal Tx voltage has to be manually adjusted. The topology of this power path is not novel and analysis of switched-mode converters exists in conventional textbooks for inductive powering. However, it is the first time a paper discusses the amplification of the quality factor in response to duty cycle changes.

Fu et al. [100] [101] has presented a buck-boost converter using the conventional topology -rectifier,

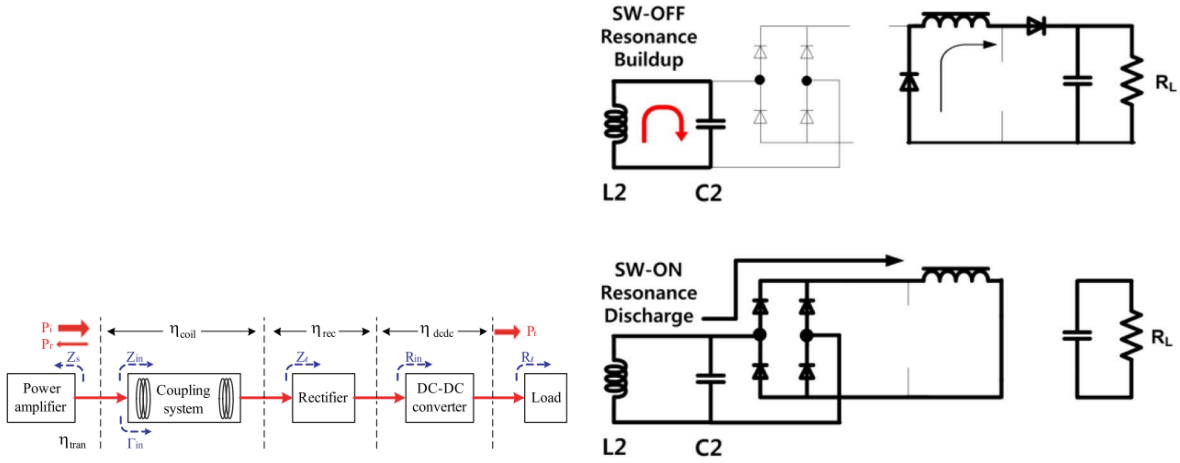

Figure 2.27: Power path of conventional inductive power transfer system Fig. 2.27a [100], and Fig. 2.27b Operation principle of resonance build up [98].

switched-mode converter- to provide the equivalent optimal load impedance Fig. 2.27a. This switched-mode converter tracks the optimal impedance and matches the rest of the circuit in response to coil displacement and changing load over time. In his work, he emphasized that the design procedure should focus on proper impedance matching between each stage of the power path flow instead of optimizing each sub-circuit itself. In other words, the complicated energy interaction between sub-circuits given the dynamic environment conditions (i.e. coupling and loading) will not entail maximum efficiency. As a result, his method minimizes the power reflection at each stage and thus obtains an efficient system. Undoubtedly, it is difficult to derive the exact input impedance of the rectifier due to its complex nature and nonlinearity. Unlike other works, Fu [100] has considered the nonlinear behaviour of the rectifier instead of providing the exact analytical expression for the optimal impedance.

In [102], Zhong used a switched-mode converter to emulate the optimum impedance by searching for the minimum input power for the given output power. The system uses two control loops: one in the transmitter and one in the receiver. The receiver loop keeps the output voltage constant in response to input voltage changes by adjusting the duty cycle of the switched-mode converter. Upon the change in the duty cycle, the control in the transmitter measures the voltage. If the new value is low, it will continue to step in the same direction. The feedback loop finds the optimum efficiency when the transmitter operates at a minimum voltage. In this system, minimum input voltage occurs when D=0.38 and separates the system into two operating regions. The relationship between the output voltage and duty cycle reverses at each of these regions. For instance, when D<0.38, the output power increases for increasing the duty cycle. While for D>0.38, the output power decreases when D increases which opposes the conventional relationship of voltage gain properties of the buck-boost converter. The operation of the converter was restricted to the right-side region, with 0.38 being the minimum boundary. Since the output voltage and duty cycle relationship is opposite to the standard buck-boost converter, the duty cycle is fed to an inverter to output the complement. However, the duty cycle boundary is not a convenient solution since it can change if the load and distance change leading to a non-stable searching procedure. Another stability issue can occur if the optimal maximum energy efficiency point shifts to the non-operating region due to frequency splitting. Related issues concern the work of Li et al. [103]. The perturbation-and-observation algorithm is also used by the works mentioned above [103] [100]. The speed of this algorithm is slow, and one perturbation-and-observation cycle can take up to 10s compared to the 3s run time in [100]. Moreover, these methods require bulky and expensive components such as an RF coupler, control hardware, and a 2.4GHz wireless communication module. A critical limitation of this approach is the limited operating range.

Ahn et al. 2016 [104] proposed a feedback control loop that automatically adjusts its actual load in response to coupling and loading variations to obtain maximum efficiency. The proposed system employs two loops: one that determines the current transmitter level and one receiver-internal loop

that senses the voltage and adjusts the duty cycle to keep it constant. Ahn et al. also proposed a novel two-switch boost-type converter arranged before the rectifier. The converter omits the inductor by exploiting the storage capacity of the LC tank. When the switches turn on, the rectifier disconnects and the current builds up in the resonance tank. Compared to [103] [101] [102] the system saves some space by omitting the inductor. Additionally, the feedback control operates much faster and for a wider coupling and load range than the perturbation-and-observation method. It also does not require bulky and expensive hardware such as an RF communication module, FPGA, or microcontroller. Yeo et al. [105] proposed a similar feedback control system as [104] but used a conventional power conversion circuit. Instead of LSK telemetry, he used Bluetooth communication to send the current data to the transmitter.

Using a dc-dc converter to track the optimum impedance is a good design choice to keep constant efficiency under a dynamic environment. However, certain limitations and constraints make this design procedure hard to implement in implantable circuits. Firstly, the maximum efficiency tracking algorithms are slow. In that sense, they are restricted from tracking the stimulation cycle in time, of which the period is in the order of a few hundred milliseconds to ten seconds [102]. Secondly, implementing closed-loop control requires bulky equipment that is practically impossible for implantable devices. Moreover, the works mentioned above had prior knowledge of the load resistance, while in the case of the neurostimulator, we need an accurate estimation of the load value since it depends on many parameters, making the design of a stable control loop challenging.

1.5.4.4. Closed-loop power control systems with back-telemetry

The topology of the following circuits consists of a rectifier that converts the AC signal to an unregulated DC value and a regulator that fixes the voltage over the load. The power on the receiver depends on the coupling between the coils, and any change in their relative position will result in voltage fluctuations. Such variations could lead to the failure of the implant due to inadequate power or excess heat dissipation that could damage the tissue. It also increases the voltage dropout across the regulator and severely degrades the system efficiency.

Therefore, closed-loop control is imperative for this system to adjust the power to the required level. Wang et al. [106] presented a closed-loop control system that keeps the receiver power constant from coupling and loading disturbances. A back telemetry link is used to send data from the implant back to the transmitter regarding the level of the rectifier output voltage. Subsequently, a digitally controlled dc-dc converter adjusts its duty cycle to supply the class-E amplifier accordingly. Similarly, Kiani [65] presented a system, but instead of producing a custom application-specific integrated circuit (ASIC), he developed a system that was built with commercial off-the-shelf (COTS) components. Unlike Wang[106], Kiani also derived a discrete-time model for the closed loop that provides accurate results.

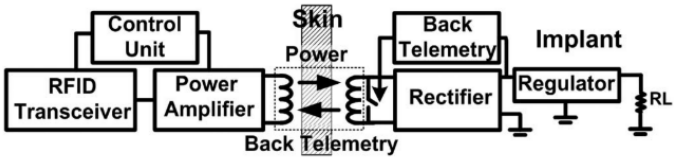

Figure 2.28: Closed-Loop inductive wireless power transfer system from [65].

Besides coupling and loading variations, the inductive link performance is also affected when the coils detune from the resonance frequency. Flexible substrates and tissue parasitics are the main reasons why the electrical parameters of the coils are usually affected. As for implants with high-quality factor coils, the performance of the link can decrease dramatically. Lee [96] along with the power-control regulation, introduced two additional loops for the resonance compensation of the two coils by employing a variable LC tank. As we already discussed, the power-controlled closed-loop systems consist of a rectifier and regulator on the receiver side. See Fig. 2.28. Using a regulator in the wireless power path chain decreases the chip area compared to switched-mode converters since there is no need for bulky reactive components. However, the efficiency of the linear drop-out regulator depends on the output-to-input voltage ratio. Therefore, as the ratio increases, the efficiency will degrade more. Thus, the closed-loop system achieves a constant efficiency by minimizing this difference for various

coupling and loading values but does not compensate for optimal coil loading. In other words, the closed-loop power adaptation prevents from dissipation of excess energy on the regulator. That is why the efficiency of the closed-loop system compared to the open-loop system increases at higher coupling. In contrast, at lower values, the efficiency is slightly lower, which reflects the energy dissipated in the closed-loop control circuit.

2.6. Goal of the Project and Research Questions

Based on the literature review, double stimulation at the occipital and supraorbital nerve is a possible treatment for diagnosed patients with chronic migraine or cluster headaches. However, the system must be implantable, miniaturized, and wirelessly powered to mitigate the adverse effects of the existing battery-powered devices.

In this chapter, we have reviewed the fundamental principles of the inductively coupled link and the peak performance that it can achieve. Additionally, we have reviewed the state-of-the-art circuits regarding the power management on the receiver side. It was observed that AC-DC conversion methods were used at any cost due to the constant voltage supply required at any modality of electrical stimulation. For instance, in voltage stimulation, a constant voltage will be supplied directly to the tissue, or in the case of constant current stimulation, a fixed voltage supply is required for the driver. Aside from that, such a topology can be unsafe or lead to inefficient operation and also imposes additional power losses due to the circuits employed for the AC-DC conversion.

Furthermore, we have reviewed the ETI dynamics and the effect of ultra high-frequency pulsed stimulation on tissue activation. Due to the capacitive nature of the tissue, this stimulation pattern can lead to tissue activation. This approach improves the efficiency, at least from the circuit design perspective -additional research is required to consider the losses taking place in the tissue for a holistic approach. Also, ultra-high-frequency stimulation improves efficiency, especially for multi-channel operations. Since such a stimulation pattern does not require a fixed voltage supply, we hypothesize that we can improve the efficiency by omitting the stimulator and bypassing the AC-DC conversion, which inherently imposes some losses on the system.

Last but not least, the stimulator should ensure adequate charge injection for the activation and keep the charge build-up within the safe injection limits to avoid any irreversible reaction. Given the unreliable nature of the wireless link, the received energy will vary over time. Thus, we aim to use a charge metering scheme to ensure adequate charge injection and tissue activation. Concerning safety, a charge-balancing scheme is also essential for the neurostimulator to prevent charge build-up rather than correcting in the subsequent stimulation cycles.

3

System Design: Ultra-High Frequency Neurostimulator

3.1. Neurostimulator System Level Design

The literature review highlights the complex network of neurons comprising the pain matrix that potentially facilitates pain suppression. In this regard, several control studies have been conducted to assess the effectiveness of stimulating the occipital and supraorbital nerves in mitigating pain in patients with medically intractable conditions. The outcomes of these studies suggest promising results for pain suppression.

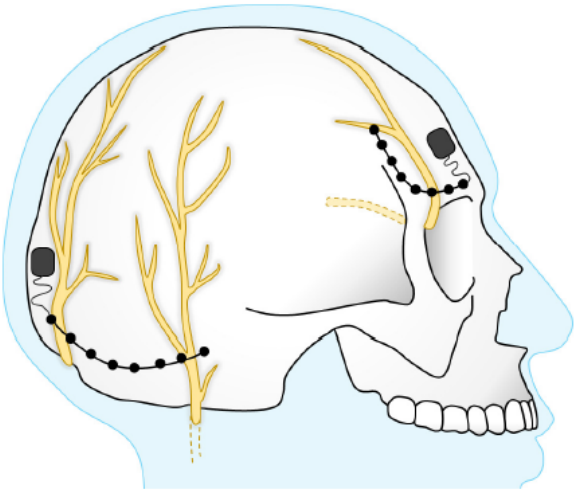

Figure 3.1: Location of the targeted nerves: Supraorbital and occipital nerves. Figure taken from [107].

As shown in Fig. 3.1, the supraorbital and occipital nerves are located in the frontal and occipital regions of the cranium. The nerves are located outside of the skull, and as a result, the implant would be minimally invasive. However, since both nerves are located far from each other, no practical wireless power transfer method can transmit power without imposing unnecessary losses to the system. For that reason, the number of implants placed will be powered independently by a corresponding transmitter. Each will target the neurons with an electrode array that can interface with these nerves.

Unlike other applications, such as DBS, the placement of the receiver coil is not a challenging task. As mentioned before, those nerves are located between the scalp and the muscle tissue, making the intervention minimal. However, the complexity of the surgical procedure arises from the fact that the occipital and supraorbital nerves extend bilaterally along the sides of the head. This presents two options: implanting a device for each nerve or limiting the number of implants to two, which would

deliver stimulation over a wider area, but require a larger electrode array and higher power demand per device. This report assumes two implants will be used, one for each occipital and supraorbital nerve.

In comparing different wireless power transfer methods, inductive energy coupling was considered a suitable solution for implants placed over the skull. Over short distances, the magnetic field maintains good coupling between the transmitter and the receiver, which yields relatively good power efficiency. Moreover, for short distances, the coil size can be kept small. As a rule of thumb, the diameter of the transmitting coil should be equal to the power transfer range. Ideally, an equally sized receiver coil will maximize the link efficiency, but it minimizes the displacement tolerance. Alternatively, a smaller receiver coil will decrease the coupling and, thus, the efficiency while providing some displacement tolerance. These parameters will be further discussed in the section regarding the stimulator requirements.

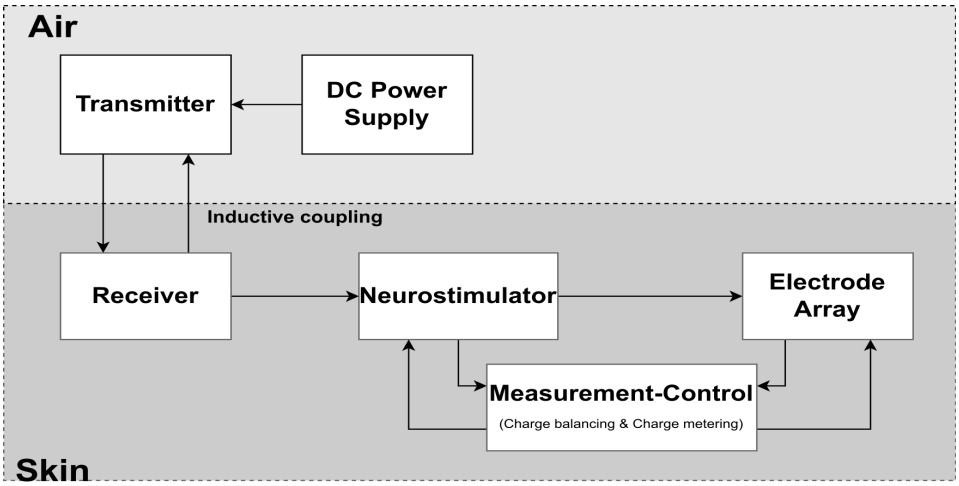

Figure 3.2: System level block diagram of a neurostimulator.

Fig. 3.2 shows the system-level block diagram of each implant. The external part consists of the DC power supply and the transmitter that sends energy to the receiver, that is implanted transcutaneously. The connection between the transmitter and receiver blocks is bidirectional because the energy oscillates between the two parts, and the neurostimulator conveys the available energy to the electrodes. A measurement and control block is responsible for the safe and efficacious operation of the neurostimulator. It does so by keeping the residual voltage at zero volts and ensuring that the activation thresholds of the nerves are reached.

The following sections will describe possible architectures conveying energy to the electrodes while avoiding severe power efficiency degredation. Subsequently, we will propose our system. A charge balancing and metering scheme is also proposed for our circuit to ensure safe and efficacious stimulation.

3.1.1. Requirements

- The proposed stimulator can deliver charge for a range $100\Omega < R_{\text{tissue}} < 3\text{k}\Omega$
- The circuit should be able to deliver 500nC within 250μs. This corresponds to a 2.5mA average current.

3.2. Evaluation of Power Efficiency at the Power Conversion Path

3.2.1. Energy Loss in Neurostimulators

Constant current stimulation (CCS) employs a current driver in the power path to generate a constant current. This method is the most preferred due to its relative safety and the established methods for charge balancing. However, their efficiency is poor due to the power dissipation across the current drivers, which are designed to operate with a high voltage supply to accommodate large electrode impedances (Fig. 3.3a). As a result, the power demands increase enormously compared to the re-

quired energy for neurostimulation. In order to minimize the dissipation across the current drivers, state-of-the-art current-mode stimulators employ adaptive power supplies to track the highest supply voltage channel, as shown in Fig. 3.3b. As a result, the channels with the highest demand will operate with minimum power loss. However, the other channels will still suffer from poor efficiency due to power loss on the drivers.

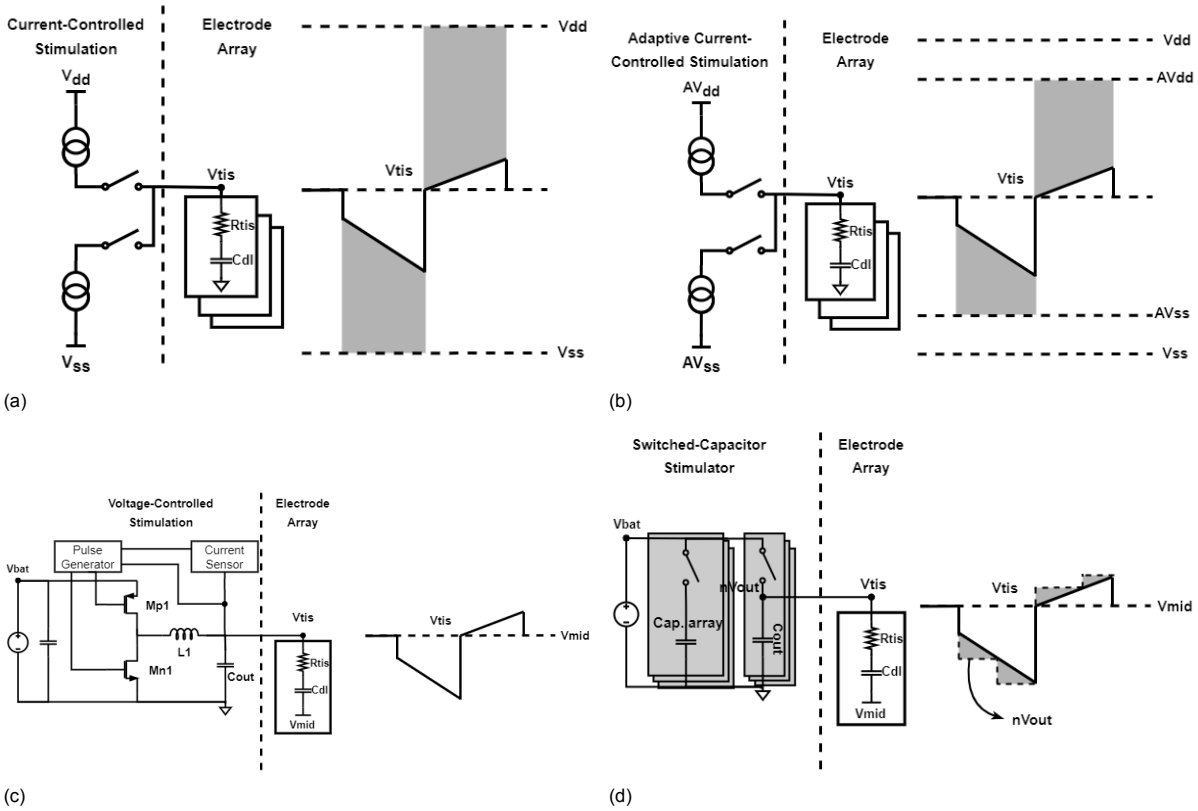

Figure 3.3: Stimulator topologies based on (3.3a) constant-current stimulation, (3.3b) adaptive constant-current stimulation, (3.3c) voltage-controlled stimulation, (3.3d) Switched-capacitor stimulator. The biphasic stimulation waveform shows the power demand of each topology, and the grey area illustrates the power dissipation.

Contrary to current-mode stimulation, voltage-mode stimulation is claimed to be more efficient but suffers from poor charge control and is significantly susceptible to changes in electrode impedance. However, maintaining a constant voltage across the electrode-tissue interface (ETI) while the ETI is still uncharged will lead to excess heat dissipation across the electrode resistance. Fig. 3.3c, shows a voltage-controlled stimulator using a switched-mode inductive converter (SMIC) and the feedback loop that measures variations of voltage across C_{out} for short time intervals to measure the current across the load and keep it constant. In this way, the SMIC output voltage is maintained just as high as the ETI voltage, as the waveform indicates in Fig. 3.3c.

Switched-mode converters have an output filter capacitor to filter the high-frequency component and supply a constant voltage at the output. Unlike conventional electronics, where the load is modelled with a resistor, the electrode-tissue interface also includes a capacitive component that models the dual layer formed at its interface. Ideally, this capacitor should have no energy stored or minimal energy at the stimulation onset, and its potential should therefore be zero or almost zero. Right at the beginning of the stimulation cycle, the output filter capacitor discharges current at the load. Sharing charge between capacitors can lead to energy loss, with a loss of 50% of the original stored energy when the capacitors have identical values. Moreover, since the electrode capacitance is charged, the supplied current is constantly changing. For a switched-mode voltage converter to efficiently drive an electrode, it must do it adiabatically by changing its output voltage to maintain a constant output current.

SMICs come with an absolute minimum of two external components; an inductor and a filtering capacitor. The inductor boosts the voltage and avoids a direct connection of the battery to the load. It also serves as an energy transformation element to bypass inherent losses that would be present by the

direct charging of the filtering capacitor. A SMIC can vary the output voltage by adjusting the duty cycle to change the energy that flows to the output continuously. Due to the capacitive tissue behaviour, the same narrative discussed above applies at the output stage of a voltage-mode stimulator. The output voltage should follow the tissue voltage and maintain a constant current flowing to perform adiabatic charging of the dual-layer capacitance. This charging process requires fine current monitoring to adjust the duty cycle continuously. However, due to the filtering at its output, this measurement should be done independently for each channel. Thus this system needs to replicate each stimulation channel making its scalability impractical.

An alternative method for supplying voltage to the tissue includes switched-capacitor power converters (SCPCs). Switched-capacitor stimulators are similar to voltage-mode stimulators that use a switched-mode inductive converter at the output. Essentially, both techniques consist of the bulky capacitor at the output to filter and supply a constant voltage at the load. The difference between both converters is that SCPCs use a capacitor or a capacitor array before the filtering capacitor to make the conversion, as shown in (Fig. 3.3d). Therefore, the energy efficiency of charging a capacitor depends on the ratio of the charging and the initial voltage, assuming a shorter time constant than the measured time. In this case, the conversion is independent of the resistance between the capacitors losing half of the energy when the capacitor charges completely. However, SCPC does achieve efficiencies greater than 50% when considering small time steps at the expense of less transferred power per time step. In particular, its efficiency achieves 100% when the voltage reaches a steady state, as shown in Fig. 3.4b. Fig. 3.5 shows the transferred and lost energy normalised to the maximum transferred energy and the corresponding efficiency to the output voltage normalised to the input voltage. From the plots, we can conclude that energy efficiency is a function of the transferred energy. High energy efficiency comes at the expense of decreased transferred energy. This behaviour indicates that a larger capacitor or a smaller load is required to maintain high efficiency. Therefore, multiple capacitor topologies must connect in parallel to provide various conversion ratios to drive the electrode adiabatically. Additionally, those arrays should connect to an output filtering capacitor array to sustain the voltage at the output. The values of the filtering capacitors will depend on the tissue impedance. However, as a rule of thumb, a higher value will minimise the voltage swing and thus will keep the capacitor at a steady state and high efficiency.

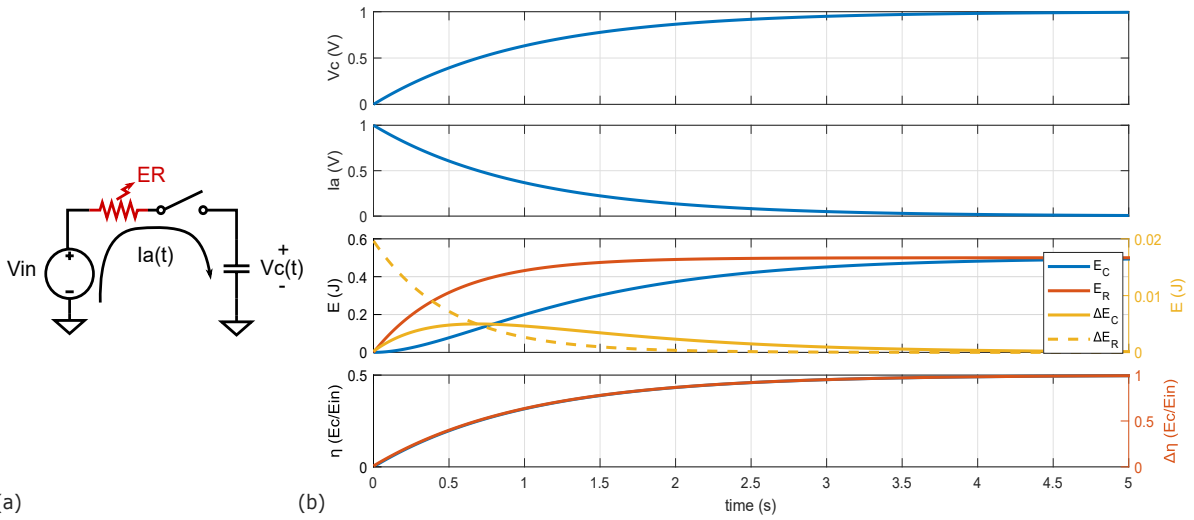

Figure 3.4: Charge process efficiency of a capacitor from a voltage source. The top graph shows the charging voltage across the capacitor. The second graph shows the charging current. The third graph shows the capacitor stored energy (E_C) and the energy dissipated across the resistor (E_R) - The value is independent of the resistor value. On the right y-axis, the transferred and lost energy were plotted by taking the difference ΔE_C, ΔE_R. Finally, the bottom plot shows the efficiency with and without considering small time steps. The energy efficiency increases when we consider small time steps and maximizes when the capacitor is fully charged. For the above simulations, the values $V_{in} = 1V$, $C = 1F$ and $R = 1\Omega$ were used.

For that reason, [108] used a bank of pre-charged off-chip capacitors to different voltages. They were connected in sequence to keep the voltage between the electrode and the capacitor small, minimizing losses by adiabatically driving the electrode. Fig. 3.5 illustrates this effect graphically, where at steady state, the energy lost in capacitor charging is much less since the potential difference is

negligible—implying that efficiency increases for small energy transfers. Essentially, SCPC can allow better integration and miniaturization when they supply resistive loads designed for a fixed voltage and output current. Nevertheless, the capacitive nature of the load leads to a changing voltage which needs to be tracked by a capacitor bank to perform a coarse adiabatic process making such a design complex and increasing the area.

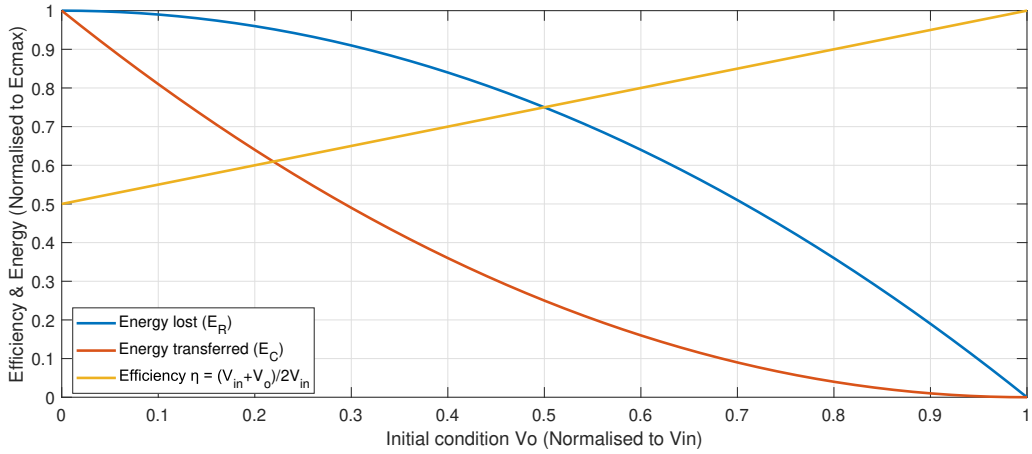

Figure 3.5: Energy transferred vs. Energy lost normalised to maximum energy transferred E_{Cmax} and the efficiency. The efficiency of the charging process increases when the capacitor is fully charged, but the transferred energy reduces dramatically. For the above simulation, the values $V_{in} = 1V$, $C = 1F$ and $R = 1\Omega$ were used.

3.2.2. Energy Loss in the Power Conversion Path

The previous analysis emphasized the power losses that occur at the last stage of the power path, assuming a constant voltage source. In order to convey a net positive charge to the tissue, several electronic circuits are involved in converting the AC to DC energy. This is due to the fact that the magneto-static field at the receiver input has a mean value of zero. Most commonly, the inductive link power path employs a rectifier, a switched-mode converter and current drivers at the last stage in the case of current stimulators. However, these systems add extra losses due to the conversion efficiency of each one of them, as depicted in region 4 of Fig. 3.6. Furthermore, to filter the output voltage and ensure stable operation, a large capacitor is necessary at the output of each stage. This requirement contributes to an increase in the surface area of the implant.

Ultra-high frequency pulsed stimulation is an alternative to current methods that supply energy conventionally. UHF pulsed stimulation would eliminate the need for voltage conversion circuits and the bulky capacitors required at the output of each stage. In addition, due to the zero average available AC magneto-static field in the receiver coil, UHF pulsed stimulation should operate as a voltage-to-current conversion element between the link and the tissue. By this mechanism, the neurostimulator can inject charge into the tissue, which leads to the generation of the action potential.

By bypassing the extra steps involved in the power conversion process, we believe that we can save some additional energy while still being able to stimulate the tissue. Fig. 3.7 conceptualizes a system-level circuit where the neurostimulator can convert a voltage input to a current output. The buck-boost converter used in [27] could make the conversion by charging the inductor and discharging it to the load. The inductor essentially converts a voltage input to a current output. Moreover, this topology omits the filtering capacitor at the output, resulting in the stream of UHF pulses released into the tissue and building up the necessary charge and voltage across the cell membranes to elicit an action potential of the cells involved.

3.3. Neurostimulator circuit level design

The system of the UHF neurostimulator consists of the following subsystems:

- *The Core Circuit* enables a power-efficient energy conversion from an alternating source with a zero mean to a stream of UHF pulses. The dynamic power supply is similar to a buck-boost converter without the filtering capacitor at its output. Thus, it generates a stream of high-frequency

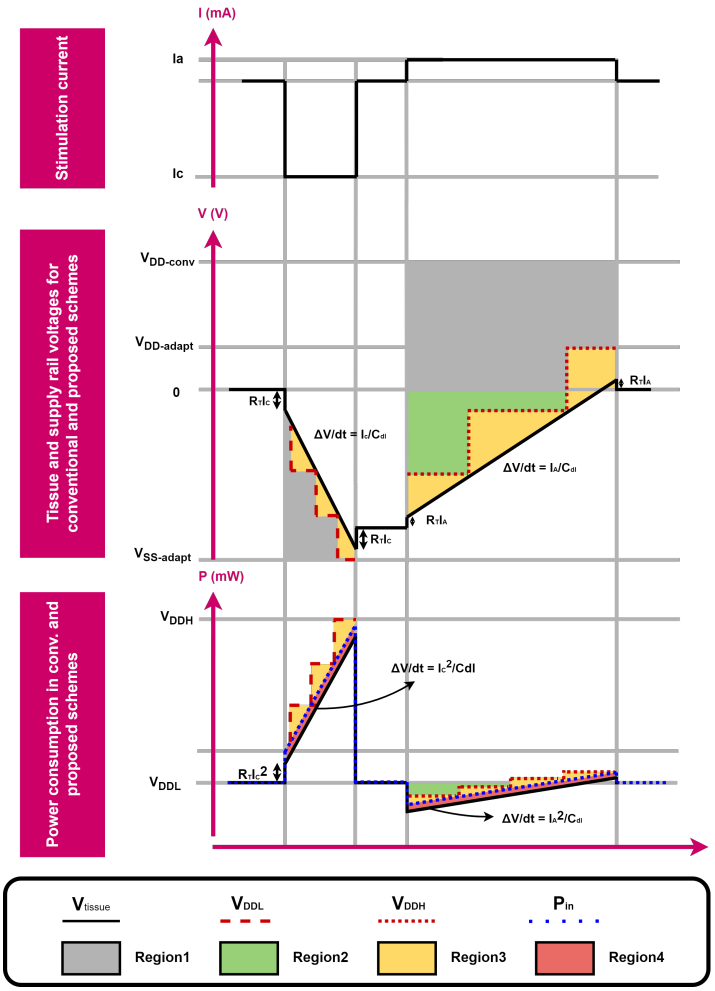

Figure 3.6: Tissue voltage and power consumption in response to biphasic current stimulation. Region 1 illustrates the energy dissipation induced by drivers in constant current stimulation. Region 3 illustrates the energy loss when the supply adapts to the tissue potential in a discrete step. Region 3 is the potential energy for recovery stored in the electrode capacitance. Figure was adapted from ([109])

pulses at the inductive link frequency. The inductor charges during the positive cycle of the input voltage and discharges at the negative cycle. Moreover, an H-Bridge is used at the output stage of the core circuit. The switches' configuration helps steer the current and form biphasic stimulation. In addition, it can operate in multiple channels by sending the pulses to different electrodes in a time-interleaving fashion. The most critical design specification for this block is circuit efficiency.

- *Charge Metering and Charge Balancing Schemes* are the circuits responsible for ensuring optimal charge injection level to the tissue and returning the residual voltage back to equilibrium.

- *Digital Control* is responsible for providing the logic to support the charge metering and balancing scheme.

3.3.1. Buck-boost converter stimulator

Fig. 3.8 shows a circuit-level diagram of one potential solution for the core circuit along with the waveforms corresponding to its operation. The circuit is a buck-boost converter that directly connects to the inductive wireless link instead of being connected to a battery power supply at its input. The forward buck-boost topology helps the converter store energy from the inductive link and release it into the load. As explained in the previous subsection, we omit the filtering capacitor. Thus, energy is converted into magnetic and released into the load avoiding inherently lossy conversion processes as in the case of switched capacitor converters.

The circuit operates in two phases. During Φ, switches SW_1, and SW_3 are closed, storing the available energy at the LC tank. This period corresponds to the positive cycle of the input sinusoidal wave. Hence, for a given input signal $V_{in}sin(\omega t)$, the voltage across the inductor can be expressed as follows.

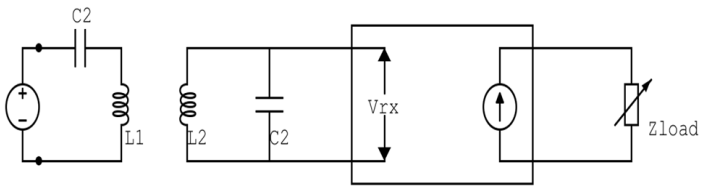

Figure 3.7: A system-level illustration of the neurostimulator input/output characteristics. The circuit should be able to convert voltage input to current output in a non-dissipative process.

$$V_L(t) = V_{in}\sin(\omega t)\cdot u(t) = L\frac{di_L(t)}{dt}$$
$$u(t) = \begin{cases} 1 & 0 < t \leqslant \pi/2 \\ 0 & t > \pi/2 \end{cases} \tag{3.1}$$

The current through the inductor is the integral of V_{in} over time divided by the inductance. Therefore, the resulting current is a cosine-like signal reaching its peak value when charging stops, as illustrated in Fig. 3.8. We can find the peak current value for a period $t = T_{on} = T_{res}/2$ assuming $V_{in} = V_{rms}$ which corresponds to $I_{peak} = \frac{V_{in}}{L}T_{on}$.

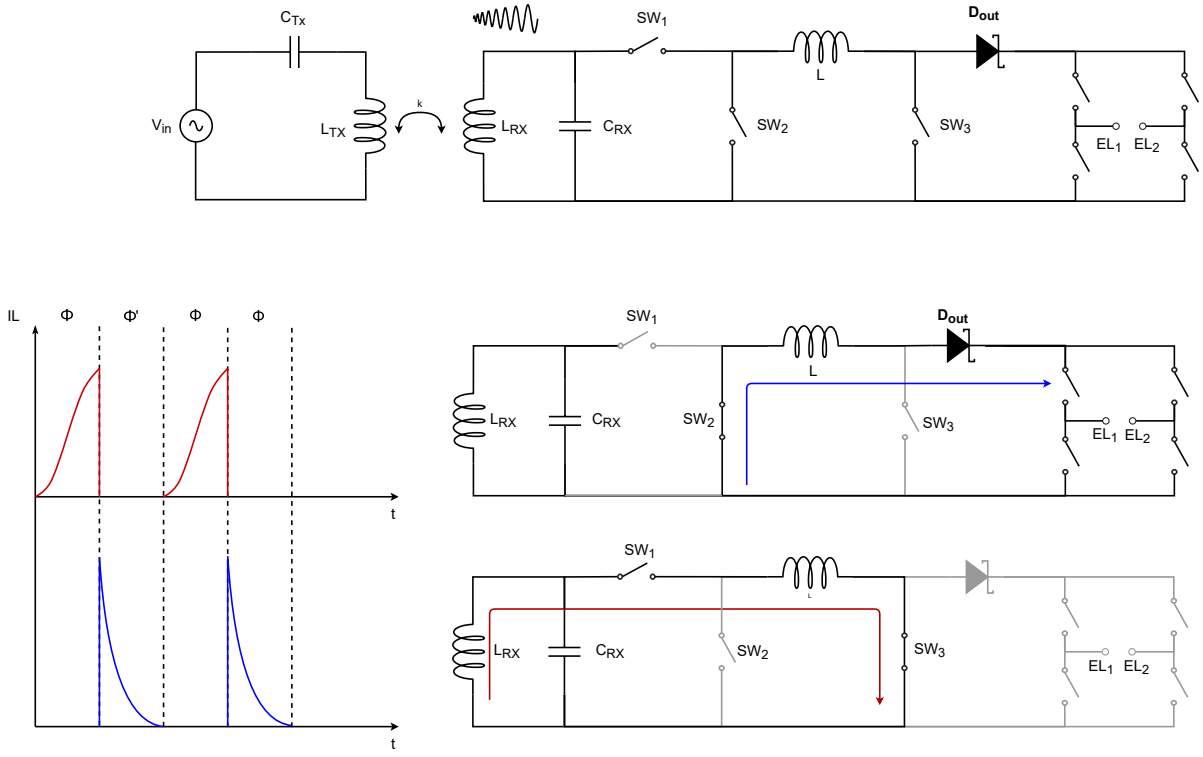

Figure 3.8: Circuit level schematic of the buck-boost converter.

During Φ', switches SW_1 and SW_3 open and SW_2 close, releasing the stored energy into the load via the H-Bridge. The energy is proportional to the duty cycle $d = \frac{T_{on}}{T}$, the inductor value (L), the amplitude and the frequency of incoming sine wave $V_{in}sin(\omega t)$. The converter should operate in discontinuous conduction mode to release all the stored charge. Hence the inductor current ideally reaches zero at the end of Φ'. In reality, due to the dual-layer capacitance of the ETI, the circuit forms an RLC during the discharging phase, which causes oscillations from the first pulse. However, given the values of the dual-layer capacitance are in the order of $1uF$, the voltage is low at the first pulses, and the reverse current is negligible. As the charge accumulates, a complete oscillation occurs, causing the reverse

currents to become predominant. The exact values of the load and the received energy are typically unknown, and coupling variations make it unpredictable when the current will start to flow back. If a large capacitor is present at the electrode-tissue interface, the time constant is large, and significant oscillations may never occur if its value exceeds the stimulation phase. Generally, the reverse current occurs at a value equal to the RMS input voltage when the circuit reaches a steady state to keep a zero average voltage across the inductor. However, it is usually assumed that τ is much longer than the stimulation phases, and energy resonance at the output of the buck-boost converter is unlikely. To avoid reverse current in the circuit, a freewheel diode is used because the input voltage, and the potential at which the reverse current occurs, are unknown. Later, we will examine the effect of the reverse currents compared to using a freewheel diode, of which the voltage drop across impacts the circuit power efficiency.

3.3.2. Symmetric buck-boost converter stimulator

In the first design, the circuit operated only for half of the period. In a way, it acts both as a half-wave rectifier and buck-boost converter. However, the half-period operation made us question the energy conversion efficiency. In particular, whether the LC tank acts effectively during the half period by building up the resonance and thus the energy conversion efficiency or the energy dissipates in power coil losses.

To investigate this scenario, we proposed a second circuit shown in Fig. 3.14. The circuit is a symmetric buck-boost converter that can flux energy from the tapped coil at any time within the input period. The circuit works as follows, during Φ_1, switches SW_1, and SW_2 are open, and the buck-boost converter coil is charging while it is parallel to the LC tank. The other half-circuit is in the discharge state, meaning that SW_5 turns on and inductor L_2 releases its energy while SW_4 and SW_6 turn off to disconnect the half-circuit from the coil. During Φ_2, switches SW_1 and SW_3 turn off, and switch SW_2 turns on, so inductor L_1 releases its energy to the output. At the same time, the other half-circuit connects the inductor L_2 to the coil by turning on switches SW_4 and SW_6.

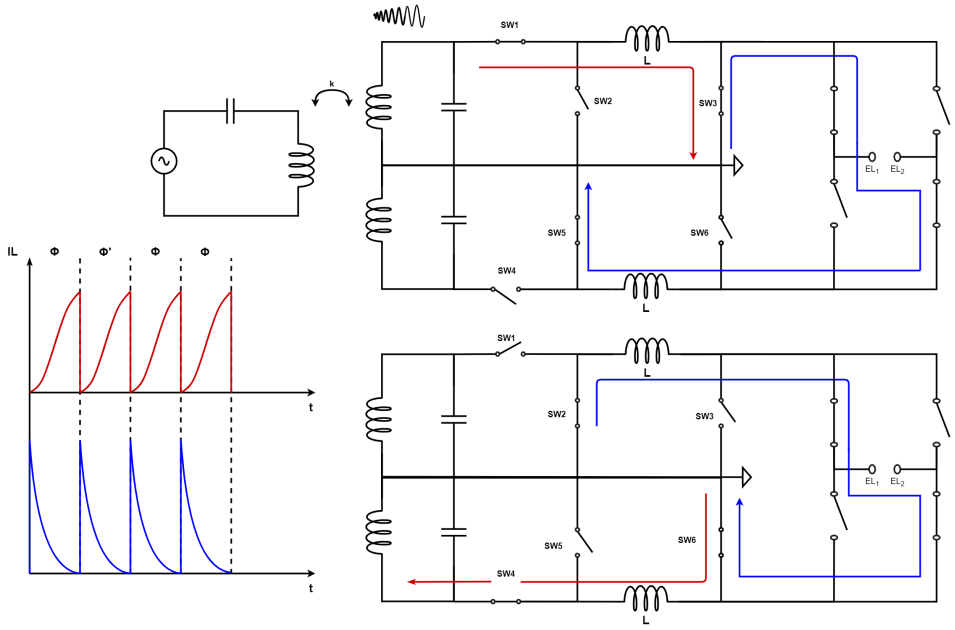

Figure 3.9: Circuit level schematic of the symmetric buck-boost converter

3.3.3. Simulations

Inductive Link Parameters

Before we start simulating the system efficiency, we must use an inductive link that can drive the buck-boost converter. In our case, we have used the inductive link designed in [62] that is able to supply 40mW at the receiver side. The coil's diameter and length were limited to 20mm and 5mm, respectively. Moreover, the resonance of the link was selected as 6.78MHz. The geometrical parameters

correspond to the geometrical constraints of our application since a coil with a diameter of 20mm can sustain relatively good efficiency up to 20mm, as well as the 5mm length, which is acceptable for transcutaneous implantation. To calculate the load, the authors assumed 13V at the output of a half-wave rectifier which can be translated to the following load

$$R_{Load} = \frac{V^2}{40mW} = 4225\Omega \tag{3.2}$$

This is the load seen after the rectifier. [66] calculates the equivalent resistance seen by the link by taking the average power consumption of the load and the diode and equating it with the RMS value of the coil. Assuming the voltage drop across the half-wave rectifier is negligible, the value of the AC load impedance is given by

$$R_{AC} = \frac{R_{load}}{2} \approx 2.1k\Omega \tag{3.3}$$

As previously mentioned, a parallel resonant topology is necessary for impedance matching to sustain the resonance when the load is high. Fig. 3.10a shows the Q-factor and parallel loss resistance ($Rp = Q^2 * R_{series}$) as a function of the wire diameter variation of a single-layer solenoid, given a fixed coil length. The number of turns also varies against the wire diameter to satisfy the length constraint. Besides the increase of the Q-factor, for an increase in the wire diameter, a drop is observed when the wire diameter is equal to 1.4mm. This is due to the series resistance that accounts for the solder joints and the PCB tracks.

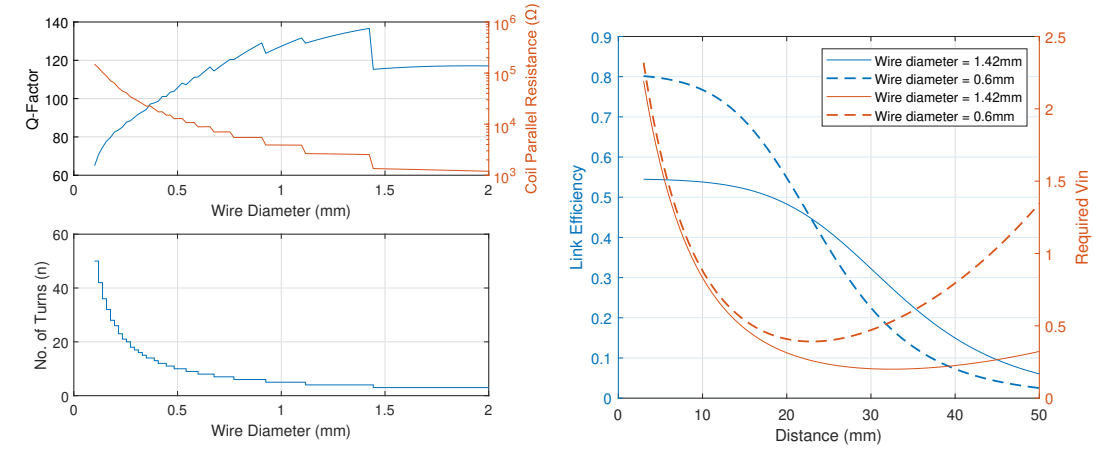

Figure 3.10: 3.10a Q-factor variation as a function of the wire diameter for a fixed coil length. 3.10b Inductive link efficiency as a function of distance for 0.6mm and 1.42mm wire diameter. The required input shown is to meet the 40mW power consumption.

Based on the maximum power transfer theorem, a parallel loss resistance equal to R_{AC} will result in a maximum power transfer. From Fig. 3.10a, this condition is satisfied when the wire diameter is approximately equal to $1.40mm$, and the parallel resistance is around $2.5k\Omega$. However, when the link maximizes the PDL, the link PTE limits to 50%. For higher PTE, a wire diameter that will give higher parallel resistance without compromising the quality factor is required. For a diameter of $0.6mm$, the quality factor decreases by 23%, and the resistance increases by 230%. Fig. 3.10b shows that the link PTE can be greater than 70% for the specified working range. Additionally, the required input voltage varies from 0.2V-2.5V to meet the necessary 40mW power consumption. As expected, the PTE for the 1.42mm wire diameter coil is limited to approximately 55% with a similar input voltage range. Moreover, the coil electrical parameters of both the transmitter and the receiver are given in Table 3.1.

In the following simulations, we will be simulating the buck-boost converter, including the inductive link at the input. For this purpose, ideal switches were utilized with minimal resistance settings of $R_{sw} = 1m\Omega$ and $R_{tis} = 1k\Omega$. To find the optimum value of the buck-boost inductor in terms of size and efficiency, we swept its value from $10 - 124\mu H$. The simulation was conducted under the worst-case scenario assumption, where the distance between the coils was set to $d = 18mm$. Additionally, the input voltage was set to $V_{in} = 0.42V$, thereby ensuring that the output voltage remains under 15V.

Electrical Parameters of Primary and Secondary Coil	Value
Inductance ($L_{TX,RX}$)	1.87μH
Series Resistance (R_S)	0.59Ω
Capacitance ($C_{TX,RX}$)	295pF
Resonant Frequency (f_{res})	6.78MHz
Self Resonance Frequency (f_{SRF})	90MHz
Parasitic Capacitance (C_{par})	1.74pF

Table 3.1: Electrical parameters of primary and secondary coil for the buck-boost converter stimulator.

Fig. 3.11a and 3.11b show the buck-boost converter's efficiency and the injected charge into the tissue. The inductor integration in power converters becomes challenging since the inductor technology is still unmatured. Therefore we need to keep its value small without compromising too much efficiency. For $10\mu F$, the efficiency is limited to 47%. However, it increases to 60% when L equals $22\mu H$. For larger values, the efficiency improvement is not proportional to the inductance. Additionally, in Fig. 3.11b, we observe that the buck-boost converter is able to inject around 550nC within $250\mu s$, which is within our requirements. Therefore, we will use the $22\mu H$ value for the next simulations.

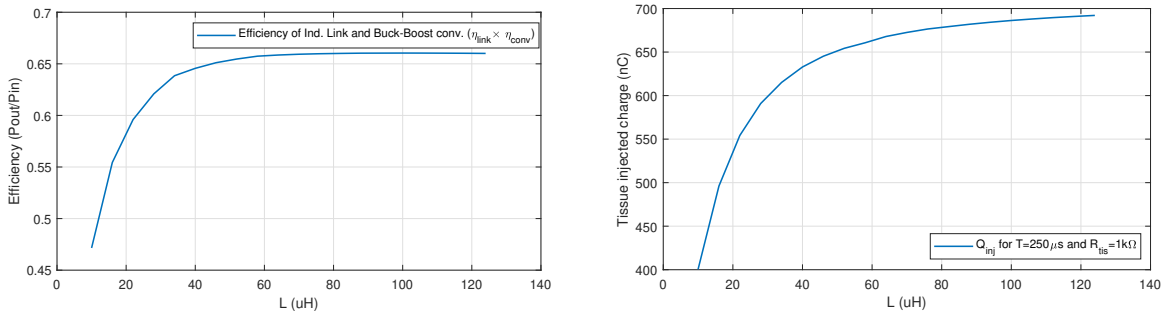

(a) (b)

Figure 3.11: Simulation of the buck-boost converter loading the inductive link. For the simulation, we used $k = 0.36$, $V_{in} = 0.42V$, $R_{tis} = 1k\Omega$ and $R_{sw} = 1m\Omega$. (a) Total efficiency against buck-boost conv. inductance value (b) Injected charge to the tissue with respect to inductance variations.

Buck-Boost converter efficiency comparison with and without a zero current detection scheme

During the discharge phase, the circuit forms an RLC resonant tank at the output. Due to the capacitance, not all the energy is dissipated in the tissue resistance, and as a result, energy starts to resonate back and forth. Usually, a reverse current is considered a loss. However, this energy is still stored in the circuit but does not become "immediately available" to the load. Moreover, if the circuit has stored energy, no more energy is supplied by the transmitter until the energy is dissipated by the load. Therefore, in this subsection, we will evaluate the performance of the circuit when reverse currents are taking place in the neurostimulator.

As explained in Subsec. 3.3.1, for each stimulation pulse, the energy will resonate. However, the energy resonance increases when the voltage across the capacitor reaches a steady state, increasing the reverse currents. The time it takes for the RLC output to reach the steady state is defined by its time constant, which is usually much larger than a stimulation phase. Additionally, the potential at which the current starts flowing back changes for each stimulation pulse until it reaches the steady point, where the average voltage across the inductor is zero. Fig. 3.12 illustrates the voltage across and the current through the inductor. V_{rec} is the rectified voltage during the charging phase and V_{out} is the output voltage during the discharging phase. When the output voltage reaches the average voltage, the dual-layer capacitor starts to supply the current, reversing its polarity. Under this condition, a steady current (I_{avg}) is flowing into the tissue.

It becomes evident that the link loading also changes when the circuit starts to operate under these conditions. Therefore we need to test whether this behaviour will degrade the link performance by

comparing a buck-boost converter with and without a zero-current detection scheme. To simulate the efficiency of the buck-boost converter, shown in Fig. 3.8, with a zero current detection (ZCD) scheme, we used a diode at the output. Although this will degrade the efficiency of the circuit, it is an easy implementation since the diode is self-controlled and will prevent the load-dependent reverse current that changes for each stimulation pulse. For the circuit, without the ZCD, we used a switch that operates with a 0.5-duty cycle. Moreover, all the switches were modelled with a $1m\Omega$ series resistance in order to be able to see the effect of the loading on the link itself.

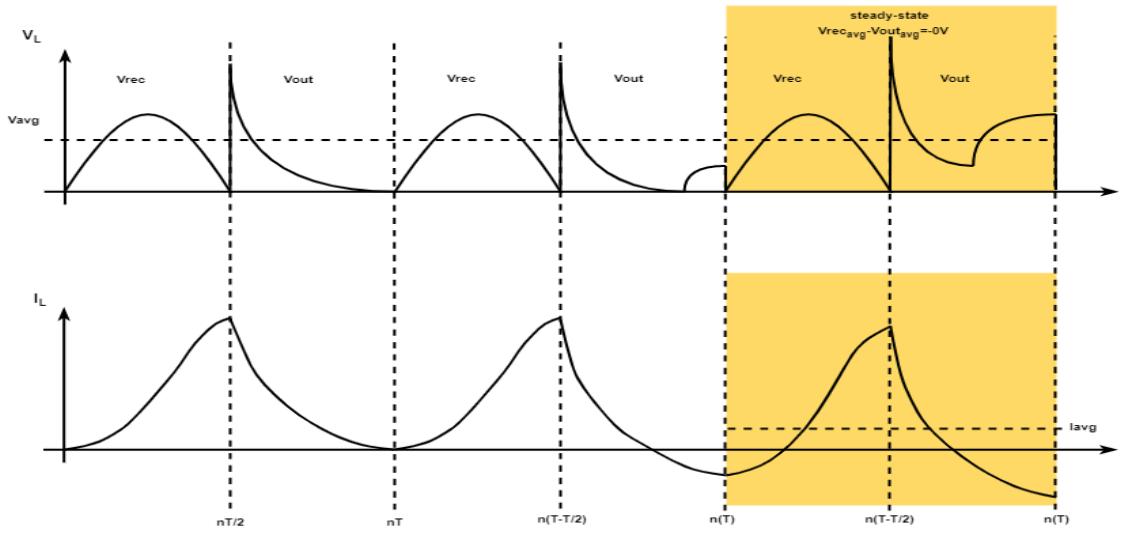

Figure 3.12: Voltage across and current through the inductor. The yellow area indicates the steady-state operation where the voltage across the inductor is zero and there is an average current across the inductor.

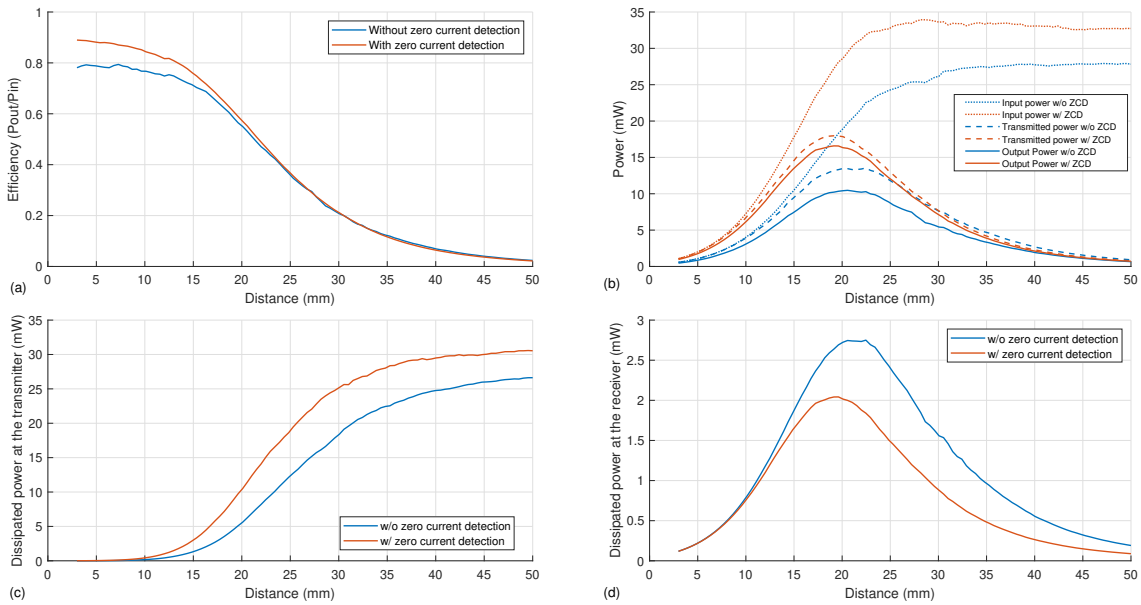

Figure 3.13: Comparison plots with and without the zero current detection. Fig. 3.13 a) compares the efficiencies between the two circuits. Fig. 3.13 b) shows the input, transmitted and output power for both circuits. Fig. 3.13 c) shows the dissipated power on the transmitter side and Fig. 3.13 d) on the receiver side.

Fig. 3.13 shows the efficiency and power levels at different parts of the circuit. In Fig. 3.13, we observe that both systems perform the same at mid- to large-range distances with a marginally better performance of the buck-boost converter with the ZCD scheme. The performance of the buck-boost

converter with zero current detection has improved efficiency by 10%. This is an expected result since the link has been optimized to operate with a specific load. Therefore, when the buck-boost inductor starts to resonate with the ETI, the average supplied current of the link is also changing. The difference between the efficiency improvement for the low- and mid-range distances can be justified due to the squared dependence of the reflected impedance. Therefore, when coils are placed close, the mismatch is enhanced. Fig. 3.13b) shows the input, the transmitted and the output power; when the coils are placed with approximately 20mm separation, the reflected impedance matches the primary coil series resistance and the efficiency limits to 50%. For longer distances, the loading is primarily affected by the transmitter series resistance which increases the input power and the transmitter dissipation while reducing the power levels at the receiver side, as shown in Fig. 3.13a) and 3.13b).

Symmetric Buck-Boost Converter Efficiency

Unlike the typical buck-boost converter, the symmetric circuit does not use a switch or a diode at its output to provide a path for the current to flow to the ground, as Fig. 3.14 illustrates. Inevitably, we cannot prevent the reverse current on this circuit topology. Fig. 3.14 shows the efficiency and power levels for the symmetric topology. Similar to the previous discussion, the efficiency of the circuit drops due to the different loading that the symmetric topology imposes on the link.

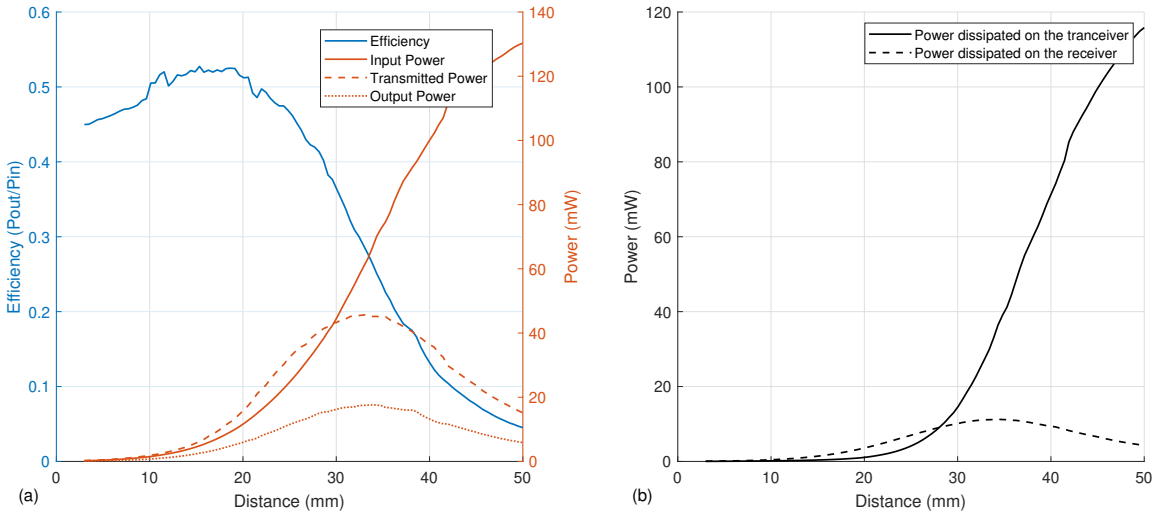

Figure 3.14: Symmetric buck-boost converter efficiency and output power with respect to distance.

The Effect of Mutual Inductance Between the Converter Inductors

The disadvantage of the symmetric inductor is the added bulky inductor to the circuit. Regardless of the area increase, an additional inductor can result in two things; Firstly, each inductor can couple to its symmetrical part and compromise the circuit operation. Consequently, the inductors should be placed orthogonally to each other to avoid any interference. Secondly, the inductors can mutually couple and enhance the circuit performance. To investigate the above scenarios, we have simulated the circuit's performance when both inductors mutually couple in opposite and identical polarity. Fig. 3.15 shows the effect of inductor coupling on efficiency. As the mutual coupling between the inductors increases, the symmetrical buck-boost converter operation changes, resulting in a load change. We also see the link efficiency drop for larger coupling between the inductors, reflecting the validity of the above point.

Besides the load transformation, we hypothesized the efficiency drop could be due to a change in the effective inductance. However, due to the complexity of the circuit and its discrete operation, it is difficult to estimate the shift in resonance analytically. Therefore, we have made a parametric analysis by adding an adaptive tuning capacitance, C_{adapt} : $(1pF, 500pF)$, with a resolution of $3pF$ parallel to C_2. Fig. 3.16 and 3.16 shows the efficiency of the simulation to the varying tuning capacitance and coupling coefficient. It becomes evident that the resonance frequency did not shift, which contradicts our prior hypothesis. Therefore, the link efficiency drops because the load shifts to a less optimum condition.

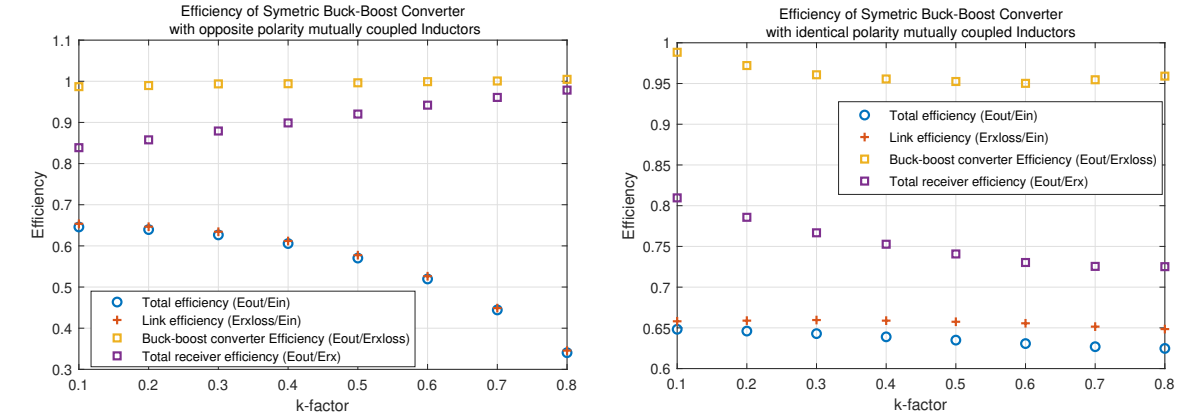

(a) (b)

Figure 3.15: Efficiency for the symmetric buck-boost converter under different coupling between its inductors. Fig. 3.15a shows the efficiency for different parts of the circuit when the inductors are coupled with opposite polarity and Fig. 3.15b for identical polarity mutually coupled inductors.

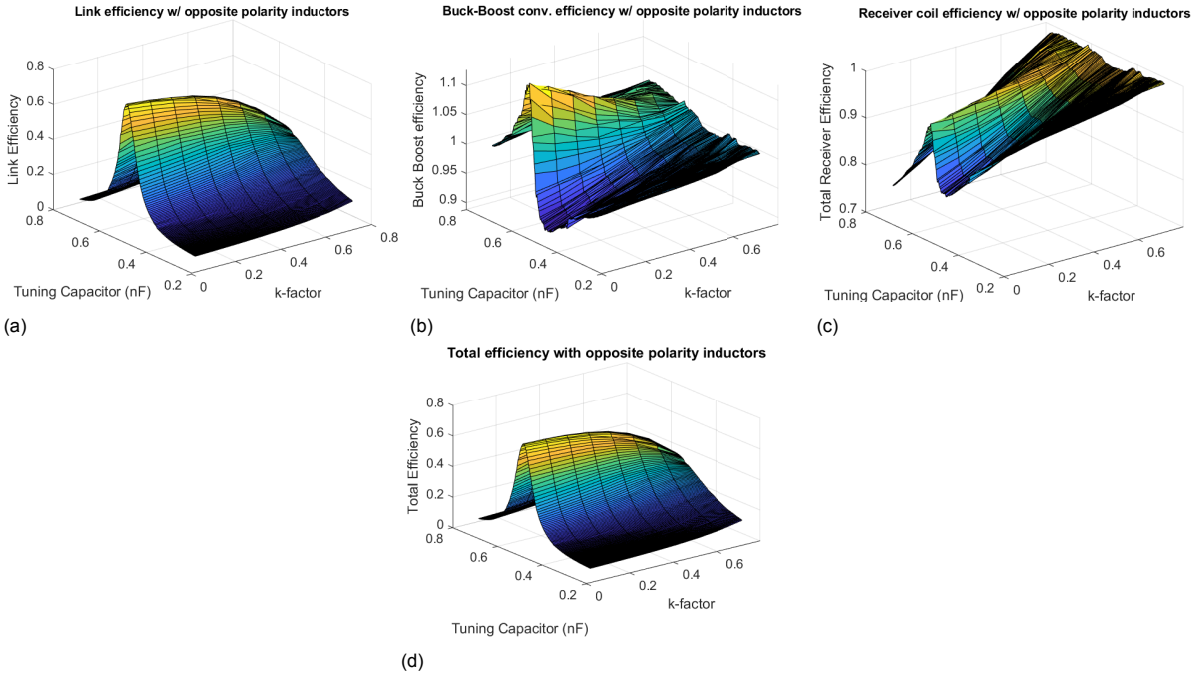

(a) (b) (c) (d)

Figure 3.16: Simulated efficiencies for mutually coupled inductances with opposite polarity to resonant capacitance C_{adapt} and coupling coefficient k. Fig. 3.16a illustrates the link efficiency, Fig. 3.16b shows the buck-boost efficiency and Fig. 3.16c is the total receiver efficiency accounting for the losses on the receiver coil. Fig. 3.16d shows the total link efficiency.

3.3.4. Proposed Design

Since efficiency is the most critical design criterion, we must compare the topologies to select which performs most efficiently. Fig. 3.18 shows the efficiency against distance; for reference, the inductive link efficiency with the $2.1k\Omega$ load is plotted. The buck-boost converter is evidently performing better than the symmetric topology for the designed range. It performs marginally lower than the inductive link due to the power dissipation across the diode used to mitigate the reverse current and because of inductance selection, as shown in Fig. 3.11. If a much larger inductance were selected, the efficiency of the buck-boost converter would be similar to the inductive link with the linear load at the expense of an increased off-chip size. As explained previously, the symmetric topology cannot prevent reverse current since a diode at its output would prevent the current to flow to the ground. This, however, limits the efficiency of the topology to approximately 50%, hence, we have also plotted the efficiency for a resistive load to compare the impact of the current. The blue plot, where no reverse current occurs,

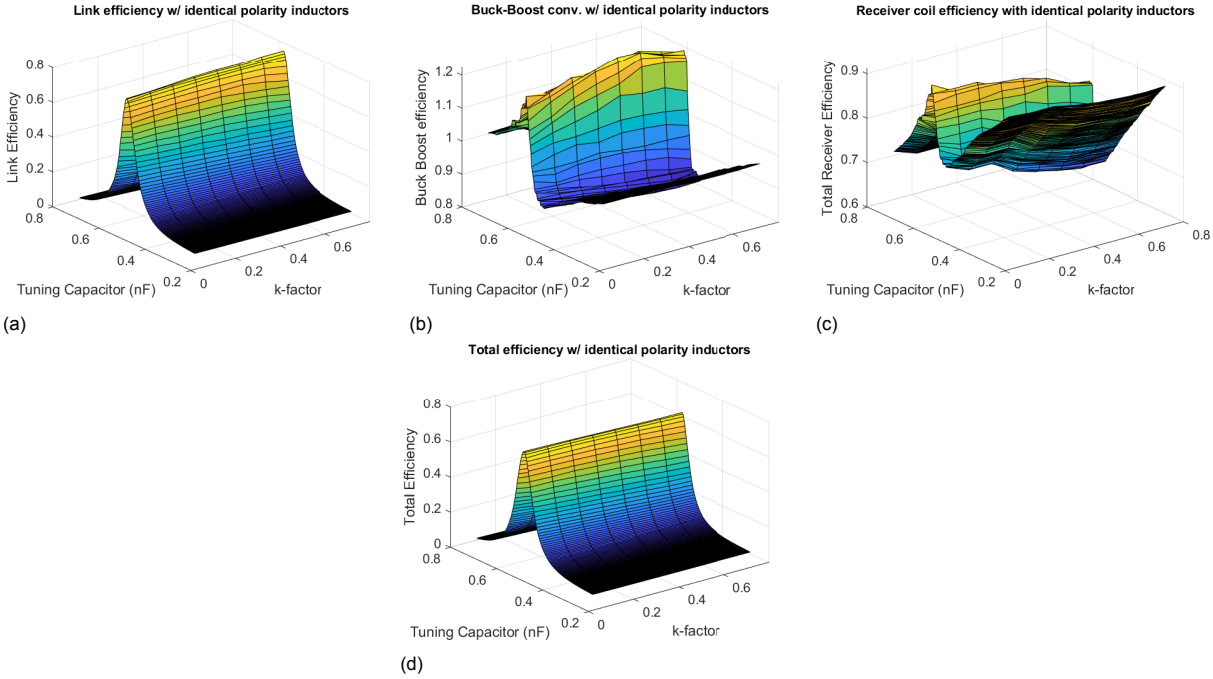

Figure 3.17: Simulated efficiencies for mutually coupled inductances with identical polarity with respect to resonant capacitance C_{adapt} and coupling coefficient k. Fig. 3.17a illustrates the link efficiency, Fig. 3.17b shows the buck-boost efficiency, and Fig. 3.17c is the total receiver efficiency accounting for the losses on the receiver coil. Fig. 3.17d shows the total link efficiency.

shows a better performance. However, the efficiency is still lower for the working range. Therefore, we have selected the buck-boost converter as the proposed neurostimulator to interface between the inductive link and the tissue.

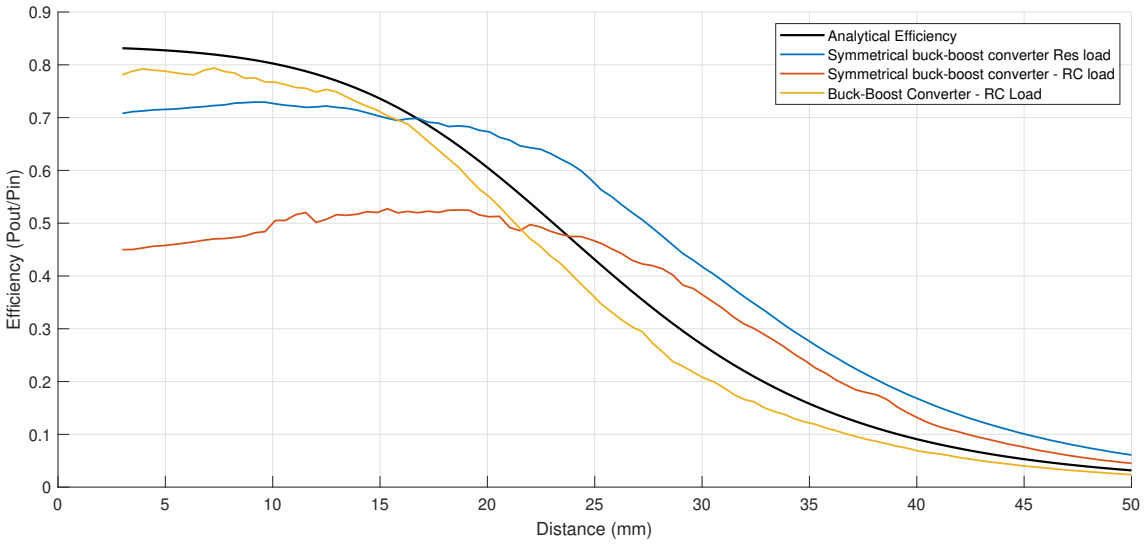

Figure 3.18: Efficiency vs distance for each of the proposed designs. The efficiency of the symmetric buck-boost converter is plotted for a purely resistive and an RC load to evaluate the effect of the reverse currents.

3.3.5. Activation efficacy: Charge Metering

Changes in the medium between the coils and coupling variations can affect the received power, which might compromise the stimulator's efficacy. For this reason, we adopted the circuit used in [107] to perform charge metering and ensure that the total charge is reached in each cathodic phase irrespective of the input power variations. This scheme adjusts the stimulation time depending on the input power

until the stimulator reaches the total charge. However, we have seen in subsection (2.4.2) that the charge threshold is a function of pulse duration. For example, an increase in pulse duration will result in a corresponding increase in the charge threshold, whereas a decrease in pulse duration will cause a reduction in the charge threshold. As a result, the charge threshold could vary from the defined total charge for stimulation with different power inputs. However, we assume that these variations are minor, and we consider that they will not affect the threshold level due to minor changes in stimulation time.

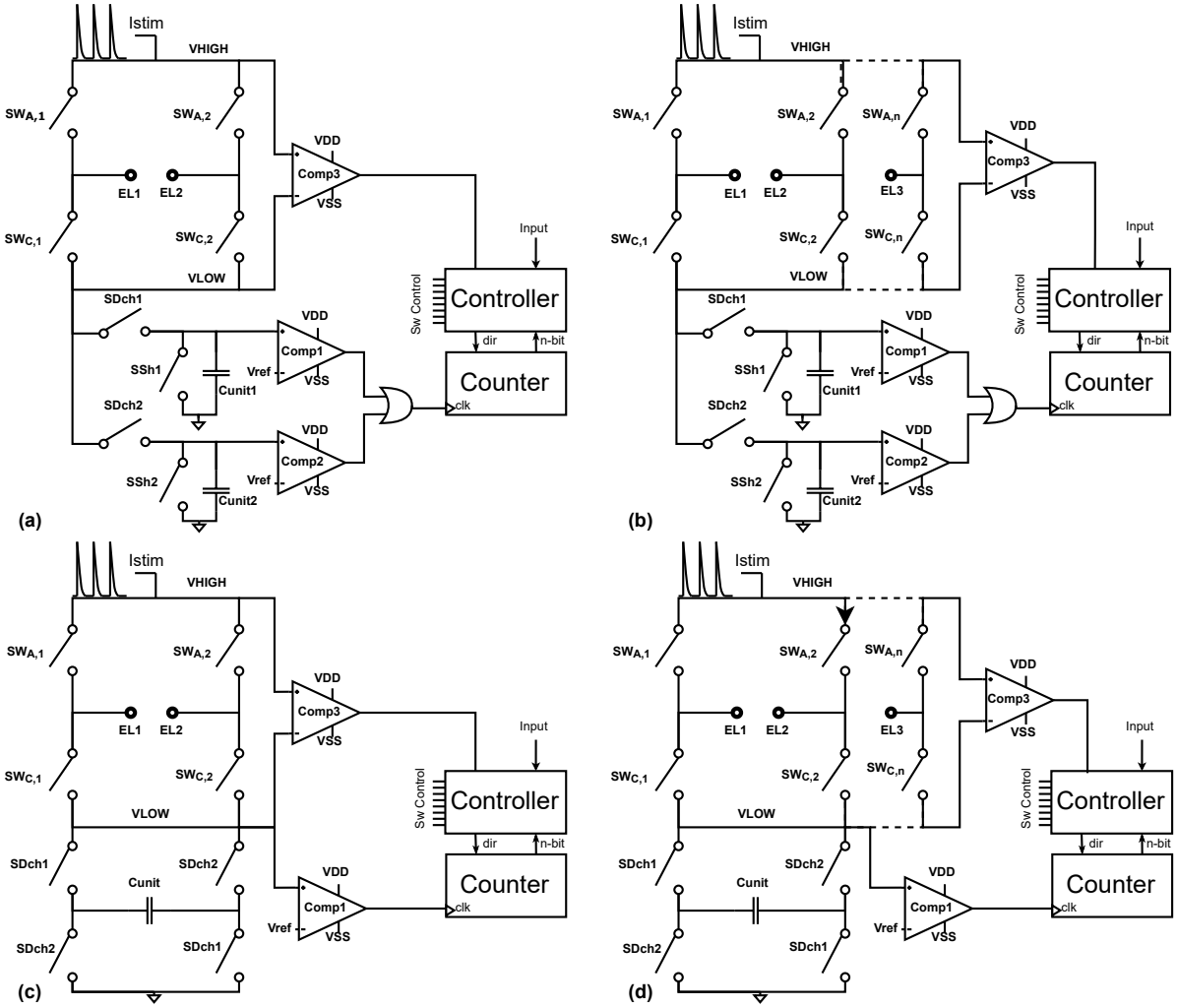

Figure 3.19: Charge metering and charge balancing circuit proposed by [107]. (a) Single channel configuration. (b) multichannel configuration. (c) Improved design with a single-channel configuration. (d) Improved design with a multichannel configuration.

The schematic of the charge metering circuit is presented in Fig. 3.19a). This circuit is connected to the low side of the H-bridge, which facilitates the control of the current flow. During the *Cathodic Phase*, switches $SW_{A,2}$ and $SW_{C,1}$ turn on, driving the electrode pair $E_{L1} - E_{L2}$ more negative. The electrode pair is then connected to the charge metering scheme, where two channels are used, each one connecting with a series capacitor $C_{unit1,2}$ that integrates the current that passes through the electrodes. When its value reaches a reference voltage, a comparator triggers to change the integration channel and discharge the charged capacitor. Those channels operate in an alternate fashion allowing for a charge and discharge phase for the capacitors. Each comparator trigger is fed to a counter to measure the total injected charge.

The precise charge metering operation is as follows. When stimulation starts, switch S_{DCh1} turns on and S_{sh1} turns off and connects C_{unit1} to the stimulating electrode E_{L1}, allowing for the current integration over the capacitor C_{unit1}. When the voltage across the capacitor reaches V_{ref}, the comparator triggers, and its output turns to *HIGH*. The counter uses this signal as an increment trigger, and the control logic uses that information to change the charging channels. Each time a comparator triggers, a

certain amount of charge has been reached, which is equivalent to $Q_{unit} = C_{unit} \times V_{ref}$. Subsequently, S_{DCh1} turns off, and S_{Sh1} turns on, allowing the capacitor to discharge, while S_{DCh2} turns on and S_{sh2} turns off to provide a conduction path for the current and continue the integration over capacitor C_{unit2}. Like the charging process of Channel 1, when the capacitor voltage reaches V_{ref}, a trigger is generated by *COMP2* and increases the number of counts. Every time a trigger event occurs, the charge metering channel alternates and this process repeats until a total charge Q_{tot} is reached given by (3.4) and is predefined by the number of counts, N, we want to reach.

$$Q_{tot} = N \times C_{unit} \times V_{ref} \tag{3.4}$$

The total charge is proportional to the number of counts, the capacitance and the reference voltage and we can alter it by adjusting each one of these parameters. Ideally, the reference voltage (V_{ref}) should be small in an IC implementation to allow for enough voltage headroom, better charge metering resolution, and minimized energy loss. On the other hand, the capacitor value should be small to reduce the chip area. However, selecting small V_{ref} and $C_{unit1,2}$ increases the number of counts, translating to higher operating speed and more high-frequency-related losses and charge metering error. Therefore, parameter selection need to be taken into consideration to minimize the losses and avoid unpredictable charge error scaling. In Subsection 3.3.7, we will elaborate on each parameter-related error in more detail.

In [107], the author presented an improved design as shown in Fig. 3.19c). This topology uses four switches, two of them to connect the capacitor at the low side of the H-bridge and the other two to the ground. In this way, the topology allows current integration at both sides of the capacitor. The advantage of this method is that it can operate with one charge measuring channel using one capacitor and one comparator, compared to the two-channel configuration shown in Fig. 3.19a). Additionally, since the capacitor is connected at the low side of the H-Bridge, it can integrate the current over different stimulation channels. This way, charge metering allows for good scalability since it can measure across multiple electrodes using the same channel.

The difference between single and multichannel operation would be that in the latter, each count will be registered for a single electrode pair while stimulating in a time-interleaved fashion. Therefore, charge packets will be distributed across different electrodes to build the charge across the tissue. In order to do that, the control circuit must register the number of counts for each electrode. However, this concept was not evaluated during the proof of concept validation.

3.3.6. Active Charge Balancing Circuit Design

As mentioned in the literature review, the best way to balance charge is to monitor the charge accumulation across the electrode-tissue interface actively. Unlike the other methods where the charge is controlled a posteriori, dynamic offset regulation stops the stimulation when the residual voltage arrives at zero and prevents any charge accumulation. The challenge in electrical stimulation is that we can not directly measure the capacitance of the electrode-tissue interface. During constant stimulation (i.e., constant-current stimulation, constant-voltage stimulation), monitoring the residual voltage will also include the voltage drop across the tissue impedance. Thus this measurement is done after the stimulation cycle. In UHF stimulation, the current flows through the electrodes only half the period, so we can exploit the second half to measure across the electrode pair. When current is not passing through the electrode, the voltage across it corresponds to the voltage of the dual-layer capacitance. Therefore, this topology uses a comparator to connect at the nodes V_{HIGH} and V_{LOW}. Although this connection does not directly measure across the electrode pairs, it allows measuring across multiple channels without using additional comparators.

The charge-balancing scheme works as follows. As long as the number of pulses counted during the anodic phase is smaller than half of the number of pulses counted during the cathodic phase, we assume that the residual voltage is far from equilibrium, and thus we do not consider the comparator output. When the counter registers the first half of the counts, the *Safety Phase*, i.e., the charge balancing starts. Starting from that moment, the controller checks the output of the comparator every charging phase, i.e., when no current passes through the electrode pair. When the voltage across the dual-layer capacitance returns to equilibrium, the comparator triggers, and its output turns to *HIGH*. This information is used by the controller to terminate the stimulation and shorten the electrode to ground to passively discharge any residual charge resulting from the finite resolution of this charge-balancing scheme.

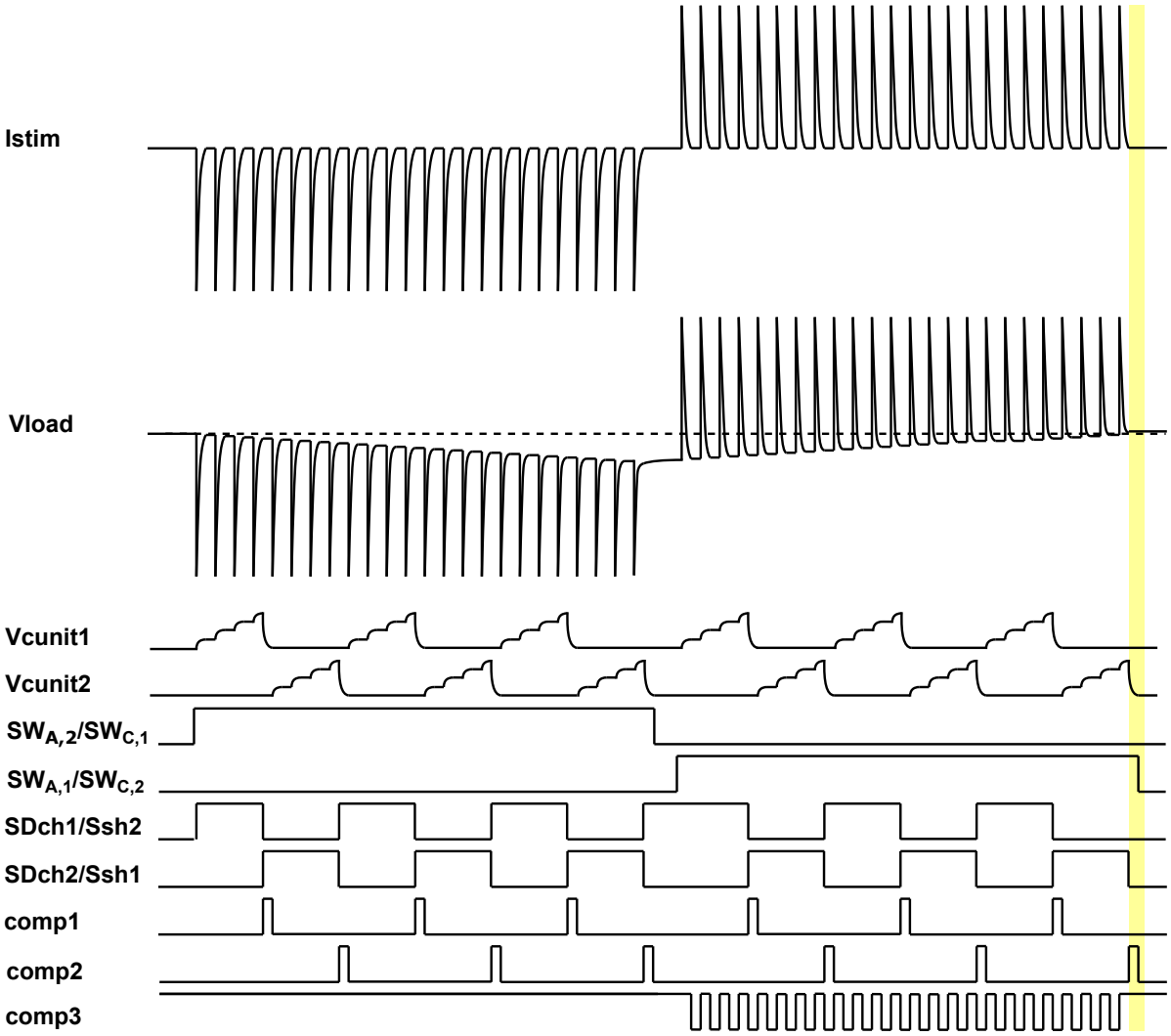

Figure 3.20: Behavioural Simulation of the Finite State Machine for the charge metering and charge balancing scheme during a biphasic stimulation.

Fig. 3.20 shows a behavioural simulation of the charge metering and charge balancing during a biphasic stimulation cycle. To begin with, I_{stim} shows the UHF stimulation pulses and V_{load} the voltage across the electrode-tissue interface. Additionally, V_{cunit1} and V_{cunit2} show the current integration across the charge-measuring capacitors. The following signals, $SW_{A1/C2}$, $SW_{A2/C1}$, $S_{DCh1,Sh1}$, $S_{DCh2,Sh2}$, represent the control signals for the switches, where the *HIGH* and *LOW* signals represent an open and close, respectively. $Comp_{1,2,3}$ are the comparator control signals used as an input to the controller for the charge-balancing and charge-metering scheme. The non-inverting input of $Comp_3$ connects to V_{HIGH} and the inverting input connects to V_{LOW}. Thus, during the cathodic phase the $Comp_3$ output is *HIGH* when $V_{EL1} - V_{EL2} = V_{load} > 0$ and *LOW* when $V_{load} < 0$, but during the anodic phase its output becomes *LOW* when $V_{load} > 0$ and *HIGH* when $V_{load} > 0$. The clk signal is the clock of the controller, $Counter_{Flag1}$ and $Counter_{Flag2}$ are the counter control signals to indicate that the stimulation reached the total charge during the cathodic phase and half the charge during the anodic phase. During the anodic phase, $Comp_3$ triggers each time the inductor discharges to the load. However, the controller tracks the output of the comparator during the charging phase. To prevent a false trigger, the controller tracks the output of the $comp_3$ twice. First, it waits for a positive trigger at the beginning of the charging phase, it then waits for a few more clock cycles and tracks its output again. If the signal remains positive the residual voltage is above zero and the controller terminates the stimulation. This process is illustrated with the yellow band in Fig. 3.20.

3.3.7. Circuit Non-Idealities and Charge Metering Error

So far, the ideal operation of the circuit has been discussed. However, the energy of the current-steered UHF pulses is not precisely known, and it is possible to reach V_{ref} during the discharging phase of the inductor. This is tricky in this design since a continuous and low ohmic conduction path is required for the current to continue to flow. However, even in the simulation with ideal components, a finite delay exists in the rising and falling times of the control signals, resulting in a large voltage spike in the V_{LOW} node. This operation is in contrast with the voltage-mode stimulator, where a switch can interrupt the stimulation and, consequently, the charge measuring process [107]. Thereby, in this design, an inherent error exists due to the current output. In order to track and provide an estimate of this error, we included a diode parallel to the charge metering channels as shown in Fig.3.21a). The results in Fig. 3.22a show the charge across the dual-layer capacitance Q_{cdl}, the measuring capacitances, $Q_{Cunit1,2}$, and the total calculated charge by the charge metering scheme (Q_{cm}). The bottom plot in Fig. 3.22a shows the charge Q_{diode} across the diode D_{cond} that is several orders of magnitude lower than the calculated charge Q_{cm}. In Fig. 3.22b, we calculated the error between Q_{cdl} and Q_{cm}, and the result indicates that the error accounts for about 0.2% of the total charge at the beginning of the stimulation while it drops for more counts. We expect that 0.2% error accounts for convergence issues of the LTspice, and thus the value is even lower as the result indicates in the more extended period. Based on the results of the simulations, we can conclude that the intrinsic error can be effectively kept at a minimum when compared to the amount of injected charge.

Additionally, in reality, the measurement accuracy is compromised due to the non-idealities of the circuit. The error occurs due to the finite switching speed, switching artefacts and parasitic capacitance. Therefore, it is critical to set the parameters given in (3.4) to measure the required total charge and minimize the error as a result of the aforementioned non-idealities.

The most apparent error is the time delay of the control loop to respond to a change. This delay is a function of several parameters. Firstly, the duration taken by transistors, acting as switches, depends on the time required for the gate capacitance to charge. Secondly, the comparator speed is limited by its finite propagation delay, which depends on the overdrive voltage. Thirdly, the control circuit delay in responding to the comparator input also contributes to the total delay. These parts are included in the red box in Fig. 3.21. This error is challenging to calibrate since it is not easy to determine its value. The resulting charge error is the integral of the UHF current pulses over the delay period and is expressed as follows

$$Q_{err} = \int_{T_{ch}}^{T_{ch}+\Delta t_{delay}} I_{stim}(t)dt = \frac{V_{error}}{C_{unit1,2}} \tag{3.5}$$

The error depends on the current amplitude and the frequency of the current stimulation. This is because the current pulses are periodic, and a faster pulse with more energy will increase the error. In other words, the error depends on the charging time T_{ch} that it takes for a capacitor to reach a charge packet ($= C_{unit1}V_{ref}$) given a capacitance value. Thus, a longer charging time would mean less measured charge, resulting in less error until the system responds to the comparator trigger. This manifests itself as a gain error and increases with the number of counts.

An additional source of error is due to the comparator bias current. The charge metering comparators connect to the measuring capacitor, increasing the measuring charge since this current does not pass through the tissue. Additionally, the non-inverting input of the charge balancing comparator connects to the V_{LOW} node, increasing the measured charge. Therefore, to minimize the error, it is essential to reduce the bias current of all the comparators. Although this error also scales with the number of counts, we can compensate for it.

Moreover, the presence of parasitic capacitance at the non-inverting comparator inputs *Comp1* and *Comp2* to ground result in a gain error in the measurement that is equal to $V_{gain,error}(t) = Q(t)/(C_{unit1,2} + C_{par})$. These parasitic capacitances result from both the nMOS switches and the non-inverting comparator inputs. This error cannot be calibrated since the exact value is not known, but care has to be taken in the layout process and in the selection of the components. Switching artefacts such as charge injection and clock feedthrough are sources of error when a switch is turned off. During the transition between the channels, the parasitic capacitances of the nMOS switches would attempt to discharge. Part of this charge will be stored on the sensing capacitor, resulting in an error independent of the C_{sence} values. Similarly, compensation techniques should be applied to minimize the switching artefacts.

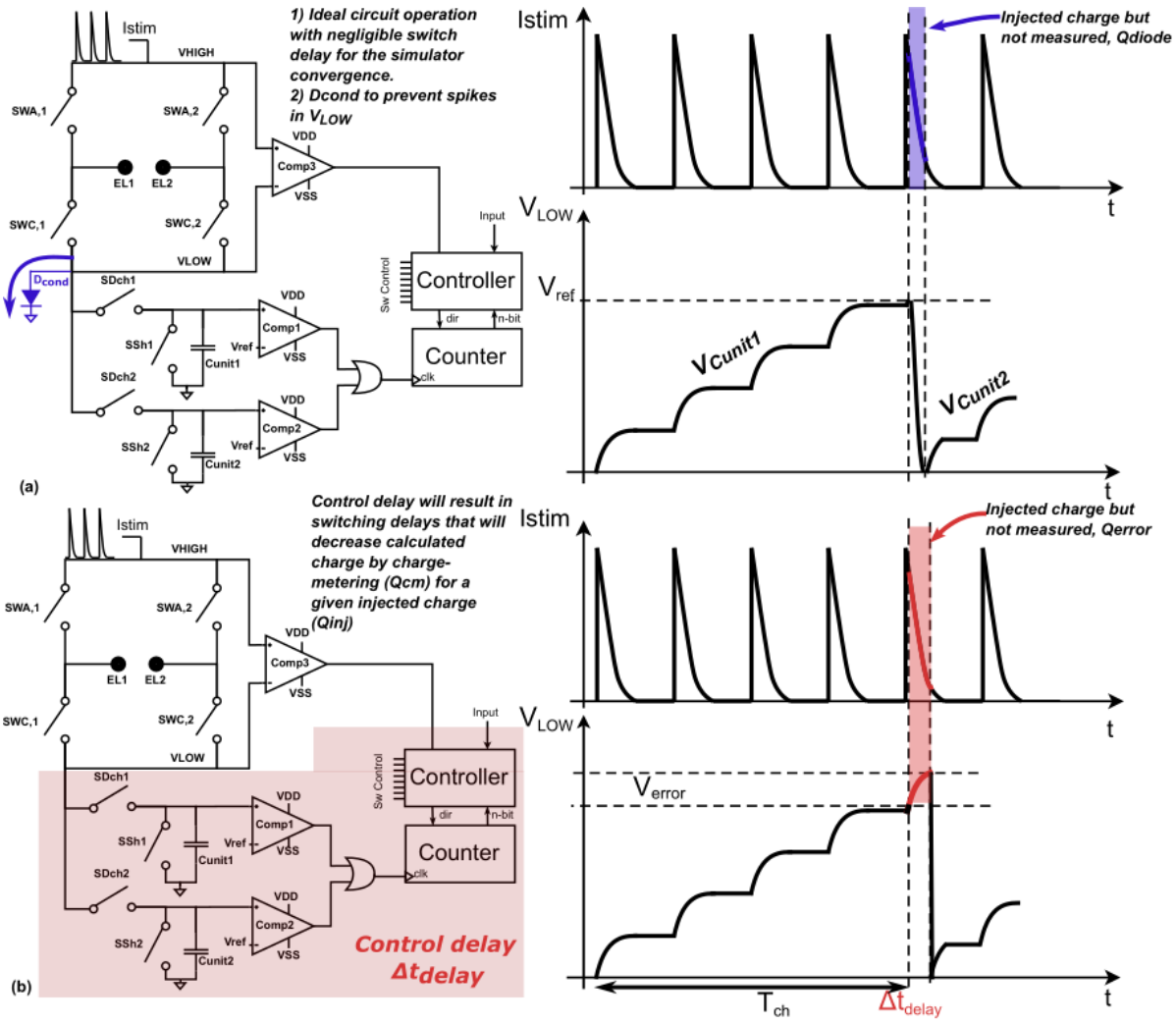

Figure 3.21: Charge metering errors. (a) The inherent error in charge metering arises from the failure to provide a continuous conduction path with low Ohmic resistance during inductor discharge, which is caused by the finite rising and falling time of control signals. (b) Error due to the delay introduced in the control loop.

3.4. Prototype PCB

To validate the proposed design, we designed a PCB prototype. Fig. 3.23 shows the schematic, including all the components used on the board. A Digilent CMOD S7 field programmable gate array implemented the digital logic of the circuit. Table 3.2 summarizes the list of components used for the following implementation.

3.4.1. PCB Implementation

The circuit operates with different switches for each part, i.e., buck-boost converter, H-bridge, and charge-metering. First, the switches used on the buck-boost converter and H-bridge were designed with an analog IC switch. The control of the analog IC switch is done by simply feeding the driving signal to the control switch. Thus we avoid using drivers that are required for high-side switching that otherwise would be essential for controlling a MOSFET. The buck-boost converter has been implemented with TS12A4516 and TS12A4517 by Texas Instruments for $Sw_{1,2}$ and Sw_3, respectively. Switch states are controlled differently for a given control signal; TS12A4516 is *OFF* when the control signal is low and *ON* for a high control input. The opposite holds for the TS12A4517 switch. Both switches operate with a $\pm 5V$ which is important due to the AC input voltage. The selection of dual rail supply switches is vital for the reliability and correct operation of the board. Otherwise, the negative voltage would conduct through ESD protection diodes. However, this selection limited the choices among fast switches. Thus,

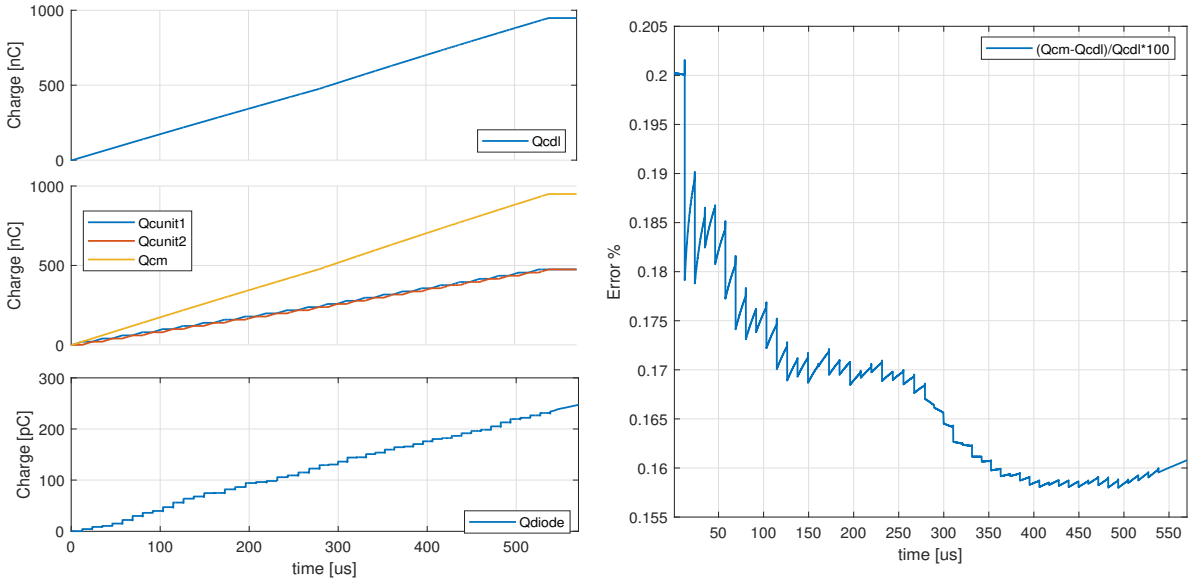

(a) (b)

Figure 3.22: Fig. 3.22a shows the current integration across the dual-layer capacitance (Q_{cdl}), switches SW_1, SW_2 (Q_{sw1}, Q_{sw1}) and the diode (Q_{diode}). Fig. 3.22b shows the error percentage.

we chose based on t_{on}, t_{off} which was 90ns. Operating at 6.56MHz with those specifications is practically impossible, so we scaled down the frequency to 500kHz, which is approximately 13 times lower. Subsequently, we scaled the inductor value proportionally to 300uH.

On the other hand, the H-bridge needs to operate with a high voltage supply due to the high voltage resulting in response to inductor discharge. This is important to avoid the conduction of ESD protection diodes. Besides the reliability concerns, the conduction of the diodes will also result in a charge measurement error since the charge will conduct to the supplies for the IC switches. For that reason, we also selected a switch based on a small charge injection value regarding the charge error. The ADG1201 maximum reported specification was -0.8pC which is suitable for our purpose. Finally, we used IRLM2030 MOSFET switches for the charge balancing scheme since they operate at low voltages and driving the switches directly by the FPGA is possible. MOSFET switches allow for much faster switching than analog IC switches, which is necessary when the voltage across the measured capacitor reaches the threshold voltage. In our design, the threshold is reached during the discharge phase, and we cannot interrupt the inductor from discharging it. Hence, it is critical to have fast switches and minimize any errors in the charge measurement. The selection of the MOSFETs was based on low total gate charge $Q_g = 1nC$ and low resistance, being $R_{ds(on)} = 154m\Omega$ as the maximum value specified under specific test conditions. For the capacitor, we used a pin socket to be able to change their values.

For the charge metering, charge balancing and clock extraction, we used the LT1715 comparator. A few considerations were taken into account for the selection of the comparator. First, the comparator has an independent input/output supply. This is important since we want flexibility on the input voltage range to test the circuit under different specifications and a 3.3V output to cohere with the FPGA specifications. Each comparator operates at different supply voltages; The comparator responsible for the charge balancing is driven by 12V to ground. The charge metering comparators are supplied with 5V to the ground. The clock generator comparator is supplied by $\pm 5V$ to avoid any current conduction to the supplies. The input bias current of the comparator was $2.5uA$, which was relatively high, limiting the accuracy of charge measurements. However, we can calibrate the error since its value is predictable. The charge metering comparator compares the measuring capacitor voltage with V_{ref} set to $200mV$. This voltage is generated by PMOD R2R, an 8-bit R2R Analog-to-Digital converter connected to the PMOD connector of the FPGA. The reference voltage is buffered by an AD8541 opamp to the input of the comparator.

The output stage of the buck-boost converter uses an RB425D Schottky diode based on its low

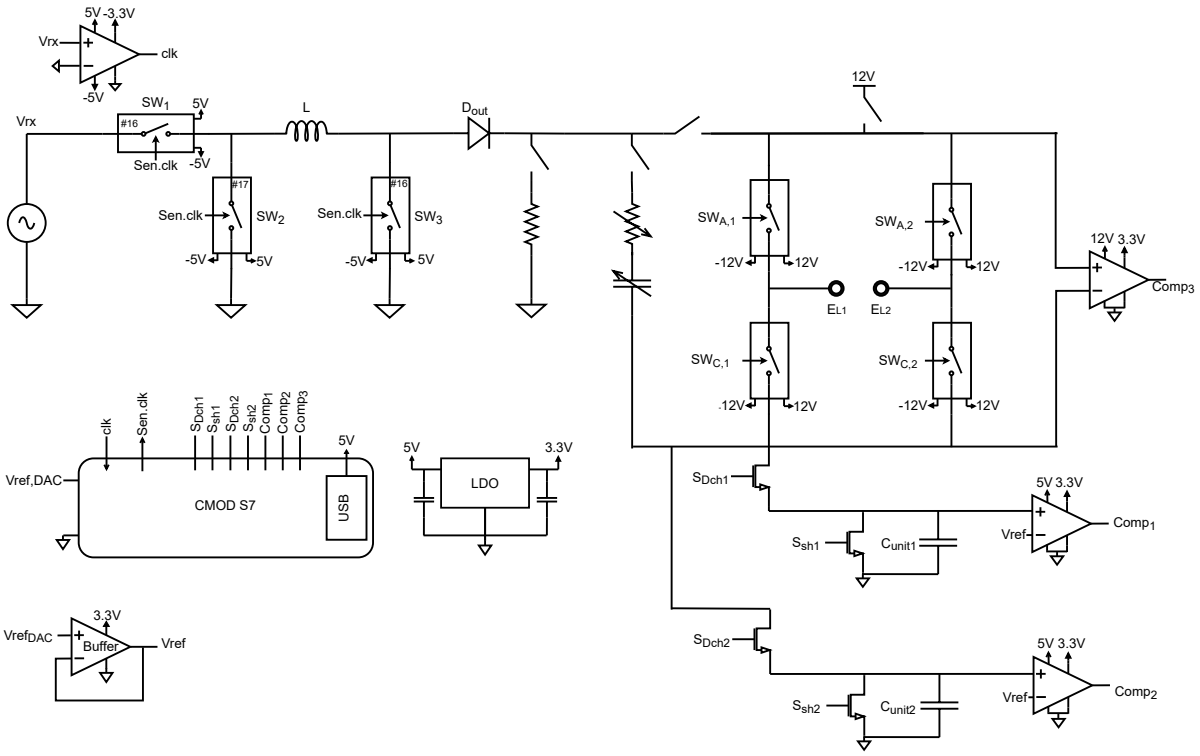

Figure 3.23: A circuit diagram of the PCB implementation. The converter and H-bridge use analog IC switches, and the charge metering is implemented with NMOS switches. The board includes an LDO to generate the 5V and 3.3V required for the comparators and a buffer to supply the voltage of the DAC converter to the comparator input. The rest of the voltages are supplied externally

voltage dropout at the current specification that our circuit operates, 10mA at $25°$ will result in around 260mV voltage drop. Also, the diode has a 6pF capacitance across its terminals, allowing fast turn-off to avoid reverse currents.

Due to the many different ICs required to satisfy each part of the board, five voltage supplies were needed. Three of them are supplied externally, and two are supplied by two low dropout regulators connected to the 12V connector. A ZLDO1117G33TA is used to generate 3.3V, and a ZLDO1117G50TA generates a 5V output. For the $-5V$, we preferred to supply it externally instead of using an inverting buck converter that could create interference due to the high-frequency switching.

Function	Component
$SW_{1,3}$ Conv	TS12A4517 SPST Switch
SW_2-Conv	TS12A4518 SPST Switch
Diode	RB425D Schottky
SW H-Bridge	ADG1201
Comp	LT1715
V_{ref} DAC	R2R - Resistor Ladder D/A Converter
V_{ref} Buffer	AD8541
Digital Control	CMOD S7 FPGA Evaluation Board
3.3V LDO	ZLDO1117QG33TA
5V LDO	ZLDO1117G50TA

Table 3.2: List of selected PCB components.

3.4.2. Digital Control

In order to implement the digital control of the prototype circuit, we have selected the Digilent Cmod S7 FPGA Module. We selected an FPGA module over a microprocessor to minimise the time delays

and, thus, the error. The FPGA synthesises the Verilog code to a digital circuit, processing the logic in parallel. In contrast, a microprocessor is constrained by the delay needed to implement each line of code separately. The board consists of 32 digital I/O pins; We have used seven pins to generate the switch's control signals and four input pins that get signals from the comparators. To generate a clock signal that is synchronized with the input signal of a buck-boost converter, an input pin is used for the output of the zero-volt detection ADC (clk). In addition, a jumper is employed to connect this node to a second BNC connector, which provides a square wave signal that is in phase with the input. This is done to ensure that the FPGA receives a square wave signal even if the comparator fails to provide a reliable one. The outputs of the charge metering and balancing comparators are also used as input to the board and control the FSM sequence, explained next.

The FPGA is responsible for providing the functionality of the four main processes: the switch control for the biphasic stimulation, the switch control for the charge metering scheme, the charge balancing and the counter. All the processes were implemented using a Moore Finite State Machine (FSM). The FPGA includes a $12MHz$ crystal oscillator used as a general-purpose clock. Within the process, most of the input signals are asynchronous, so a sequential logic block is always used to synchronise them. For example, the clock frequency is 24 times larger than the buck-boost frequency, which runs at $500kHz$, the same frequency as the input signal. Thus, in the worst-case scenario, it takes $8.333ns$ for an ideal system to update the signal, not considering the setup and hold time necessary for the register to be valid. Although this is a tolerable delay, we will need faster processes that require sampling multiple times a fast-changing asynchronous signals such as $comp_3$ detection. For that reason, we generated a $300MHz$ internal clock signal with a Mixed-Mode Clock Manager (MMCM) Module, which will be used for all the processes.

The most fundamental process of the board is biphasic stimulation. Without it, neither of the above processes can function. Fig. 3.24 shows the sequence of the state machine in a state diagram. It consists of 5 states: *IDLE*, *First Phase*, *IPD*, *Second Phase* and *Safety Phase*. When the system is powered up, we need to provide an initial state for each process. We use btn0, and the biphasic stimulation transits to the *IDLE* state. To start the stimulation, we use btn1 as the trigger signal, which will change the state to the *First Phase* starting the cathodic stimulation. At this point, the charge balancing also transits from the $IDLE_cb$ to $Charge_Channel1$ state to start measuring the charge. The charge metering consists of seven states, $IDLE - cb$, $Charge - Channel1$, $Charge - Channel1_{t1}$, $Charge - Channel1_{t2}$, $ChargeChannel2$, $Charge - Channel2_{t1}$ and $Charge - Channel2_{t2}$ as shown in Fig. 3.25. $Charge - Channel1$ and $Charge - Channel2$ are the charging states, thus switches $SDch_1$ and Ssh_2 are ON, while $SDch_2$ and Ssh_1 are OFF for the channel1 charging phase and the opposite for the channel2 charging phase. The states in between are time-controlled states that delay the switches to turn ON/OFF without compromising charge measurement accuracy. For example, $Charge - Channel1_{t1}$ turns all the switches off, and after a few clock cycles the timer makes the transition to $Charge - Channel1_{t1}$ turning Ssh_1 to discharge the C_{unit1}. A few clock cycles later, the state moves to $Charge - Channel2$. The same process repeats once the charge reaches the threshold; first, all the switches turn *OFF* and then S_{sh_2} turns *ON* to discharge the measuring capacitor.

The charge metering aims to measure the number of charge packets by tracking the triggers of $comp1$ and $comp2$. However, since the propagation delay of the comparators used for charge metering is in the order of 2ns, it can likely toggle before the FPGA executes the channel transition. For this reason, the compactor output signal is unreliable; therefore, it is not straightforward to measure the positive edges of the signal. To count the trigger reliably, we implemented two FSMs, each using *comp1* and *comp2* as an input signal that will generate a pulse once we sample the signal. The state diagram of this FSM is shown in Fig. 3.26, which consists of four states, *IDLE-PG-c1,2*, *Initial-Stand-c1,2*, *Activate-Pulse-c1,2* and *Wait-Loop-c1,2*. Similarly to the other FSM, the initial state is defined upon pressing btn0. Once the sequential process detects the $comp1, 2$ signal, it transfers to *Activate-Pulse-c1,2*, which generates a reliable signal pulse to track the counts. To avoid generating more than one pulse, the *Activate-Pulse-c1,2* state lasts for 21 clock cycles; after that transits to *Wait-Loop-c1,2* for six clock cycles before moving back to the *Initial-Stand-c1,2*. Once the counter reaches the predefined number of counts, it generates a signal $Flag$ equal to *HIGH* that makes the transition to the IPD phase of the biphasic stimulation. After a hundred clock cycles, the state proceeds to cathodic stimulation, and the same process repeats until the counter reaches half of the predefined counts to transit to *Safety Phase*. During the last state, the FPGA detects the output of $comp3$ during the charging phase of the inductor when no current flows to the output. However, near the transitions of the buck-boost converter,

the FPGA is subjected to noise caused by the zero-voltage detection scheme, and the residual charge at the $comp3$ input could likely result in oscillations at its output. Therefore we have implemented a fourth state machine that consists of four states, *IDLE-PG-c3*, *Initial-stand-c3*, *Delay-phase-c3* and *Activate-pulse-c3*, as shown in Fig. 3.27. The *Initial-stand-c3* state records the $comp3_reg$ signal when the charging phase start. If the signal is *HIGH*, the FSM transits to the time-controlled state, *Initial-stand-c3*. After 250 clock cycles, it moves to *Delay-phase-c3* and samples $comp3_reg$ again. If the signal is high, it moves to the *Activate-pulse-c3* to turn $comp3 - reg - reg - 1p$ *HIGH* for 250 clock cycles, which stops the stimulation, else the state moves back to *IDLE-PG-c3*.

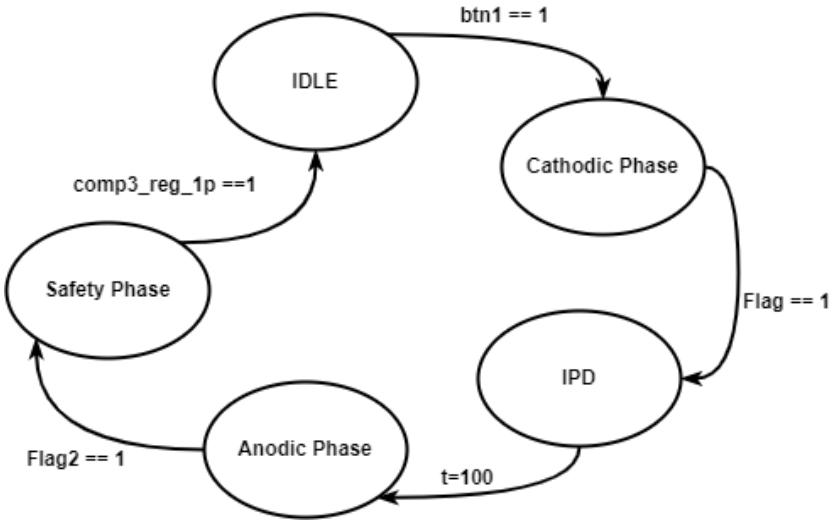

Figure 3.24: Finite State Machine (FSM) representation of the stimulation cycles. The FSM starts with pushing a btn1 and moves through different states -phases of stimulation which eventually terminate when residual voltage returns to zero

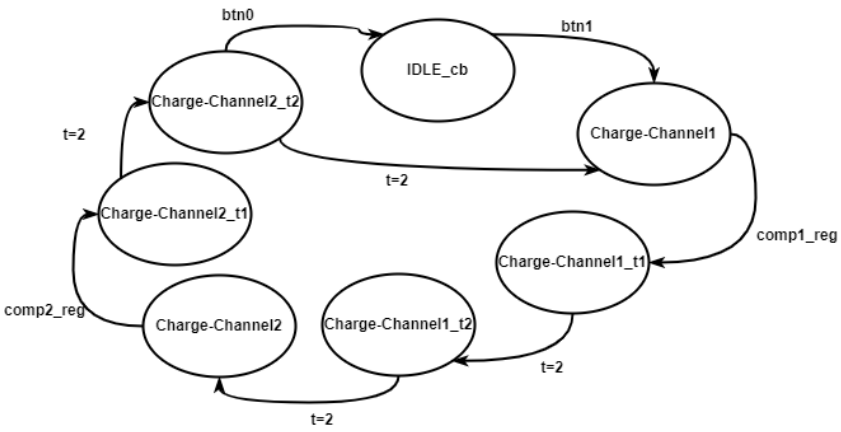

Figure 3.25: Finite State Machine (FSM) representation of the charge-balancing scheme. The initial state is registered when btn0 is pressed. *Charge-Channel1* and *Charge-Channel2* require an input signal from $comp1_{reg}$ and $comp2_{reg}$ respectively, to proceed to the next state. The input signal t indicates the clock cycle number that the timer needs to complete before a transition will occur to the next state.

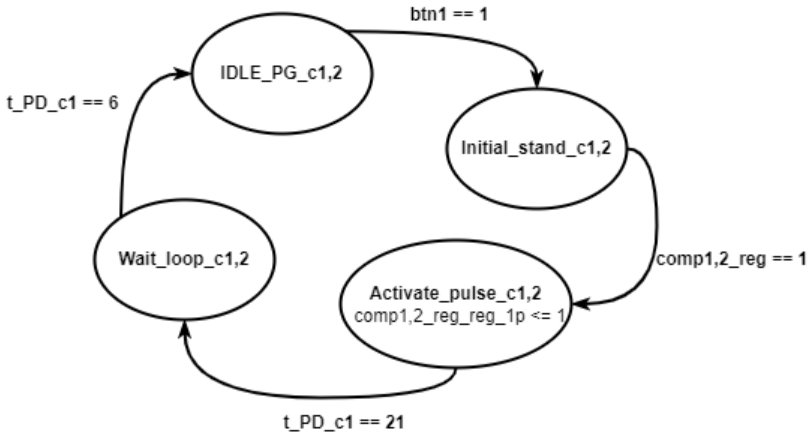

Figure 3.26: Finite State Machine (FSM) to generate a reliable pulse based on a $comp1,2$ trigger. In principle, this state machine samples until it detects $comp1,2$. Once it detects, it generates the $comp1,2-reg-reg-1p$ signal. The timer and *Wait-loop-c1,2* state ensure that only one pulse will be generated for each $comp1,2$ trigger.

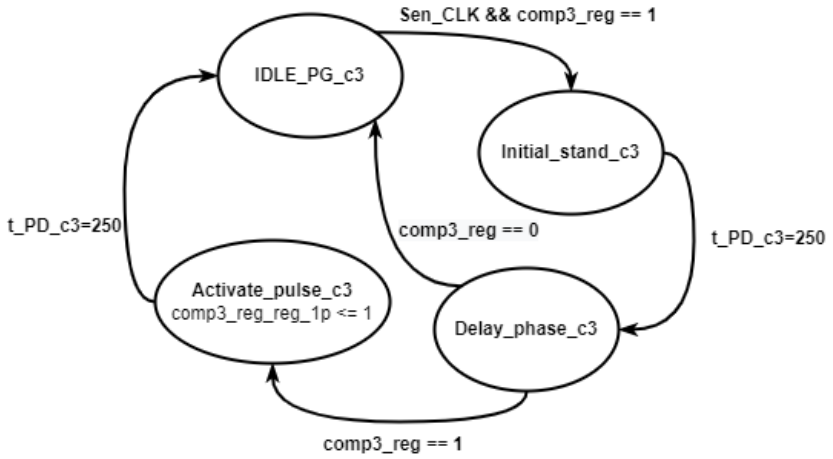

Figure 3.27: The charge-balancing finite state machine that samples the $comp3$ output twice to stop stimulation reliably. The exact operation tracks if the signal is *HIGH* during the inductor charging phase, and it waits for 250 clock cycles until it samples again. If the signal is *HIGH* it triggers $comp3-reg-reg-c3$ signal, else the process repeats.

4

System Validation

To evaluate the system's functionality, we followed the subsequent procedure. First, we simulated the functionality and performance of the circuit, starting with ideal components and then replacing them with manufacturer's models. Second, we designed a PCB prototype to validate the circuit performance further using a linear model and an electrode submerged into a phosphate-buffered solution.

4.1. Circuit Simulations

The final system presented in Fig. 3.23 was simulated with LTspice software. To validate its functionality, we first simulated the performance using ideal components and the inductive link as designed in Subsection 3.3.3. For all the simulations, we used a linear ETI model with $R_{tis} = 1k\Omega$ and $C_{dl} = 1\mu F$. The simulation results are shown in Fig. 4.1.

$V_{EL1} - V_{EL2}$ represents the voltage across the linear ETI model. The second plot shows the residual voltage across the dual-layer capacitance C_{dl}, reaching the $480mV$ minimum value corresponding to the injected charge of $Q_{inj} = 480nC$. For the charge metering scheme, we selected two $100nF$ capacitors with a reference voltage $V_{ref} = 200mV$. The number of counts was set to $N = 24$, resulting in the programmed charge $Q_{cm} = N \times C_{unit1,2} \times V_{ref} = 480nC$. The injected and programmed charge are equal, validating the correct circuit operation. Fig. 4.1 illustrates that upon reaching a count of $N = 24$ for both $comp1$ and $comp2$ triggers, the cathodic stimulation stops. Following this, an interphase pulse delay (IPD) of duration $0.115\mu s$ occurs before the initiation of the anodic phase, as indicated within the magenta box. Similarly, with the cathodic phase principle, the anodic phase continues until the integer number of half the counts is reached to enter the safety phase. During the *Safety Phase*, the $comp3$ measures across the ETI twice when there is no current through the load. We do that to avoid a false positive trigger caused by either injected stored charge during the buck-boost switching or oscillations that occur because of the RLC output. As expected, the stimulation stops when the residual voltage returns to zero, and no undesired behaviour is observed. This is expected, given that the circuit models are ideal.

The circuit behaviour was also simulated with the manufacturer's models chosen for the PCB implementation. This time, we have increased the number of counts to $N = 24$. Similarly to the previous discussion, Fig. 4.2 shows the analog signals, $V_{EL1} - V_{EL2}$ being the output voltage across Electrodes 1 and 2, the voltage across the dual-layer capacitance V_{Cdl}, and the voltage across the charge measuring capacitors $V_{cunit1,2}$. It also includes the digital signals $comp1$, $comp2$, $comp3$ and $SafetyPhase$. As explained in Subsec. 3.4.1 we scaled down the input frequency such that the circuit will operate from $200kHz$ to $500kHz$ and also scaled the inductance to $300\mu H$, proportionally to scaling the frequency from $6.58MHz$ to $500kHz$. The results were obtained using a $500kHz$, $2.5V_{Pk-Pk}$ input signal and the tissue model parameters being $R_{tis} = 1k\Omega$ and $C_{dl} = 1\mu F$. The input voltage was limited to $2.5V_{Pk-Pk}$ to prevent analog IC switches from clipping due to the large output voltage.

In comparison to the ideal circuit, the outcomes depicted in Fig. 4.2 indicate that the dual-layer capacitor (C_{dl}) discharges into a resistance, as demonstrated by the non-linear relationship of the dual-layer voltage during the anodic phase. Furthermore, the faster charging rate of the unit capacitors at the anodic phase onset can also observe this behaviour. This can be attributed to the forward-biasing of the

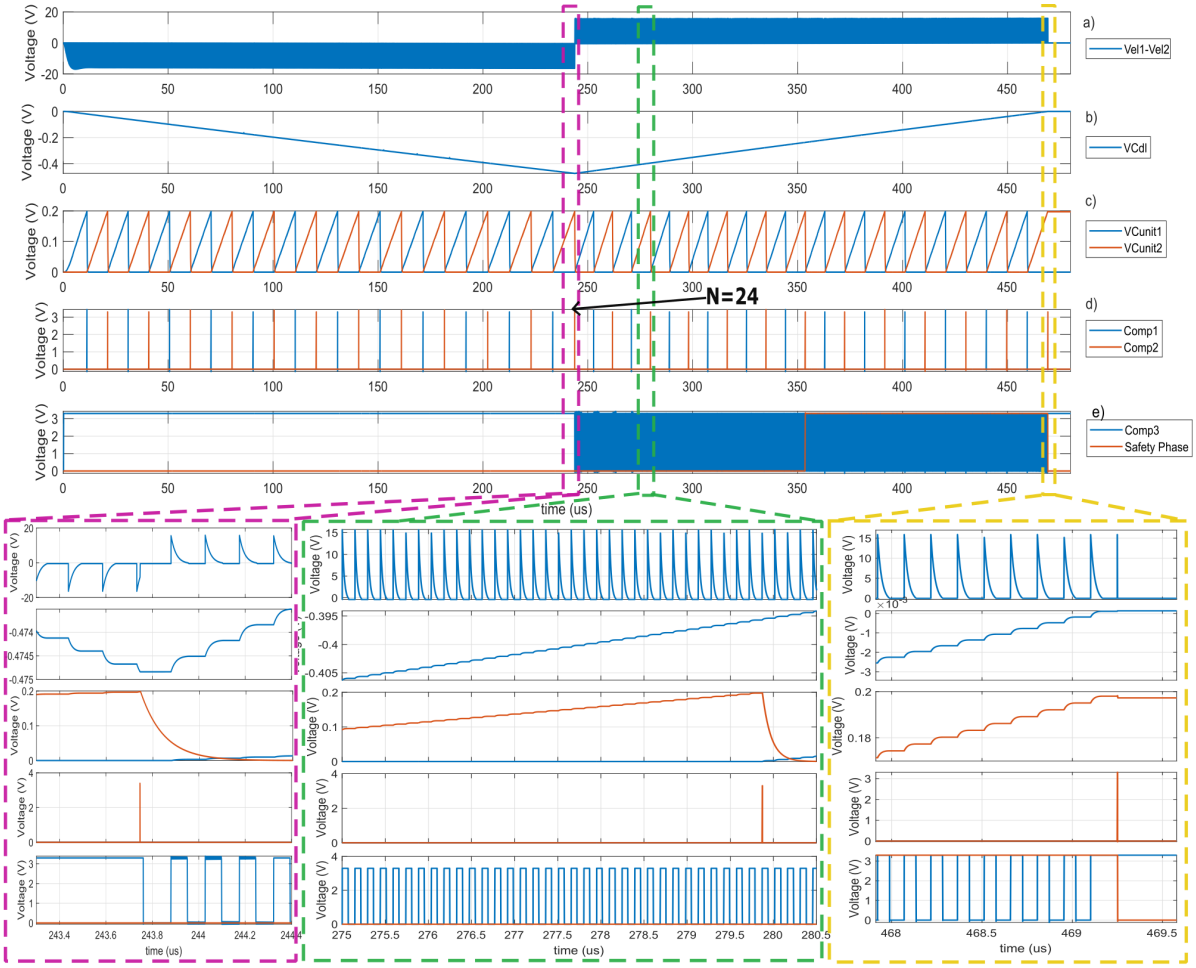

Figure 4.1: Simulation waveforms at each stage of the circuit. a) Electrode-tissue interface voltage $V_{EL1} - V_{EL2} = V_{load}$. b) Dual-layer capacitance voltage. c) Voltage over sense capacitors. d) response of the charge-metering comparators ($comp1, 2$). e) Output voltage of the charge-balancing comparator and indication of *Safety Phase* state period. The magenta box zooms in at the end of the cathodic phase for $N = 24$, followed by the IPD that lasts for $115\mu s$. The green box shows a zoomed plot when V_{unit1} reaches 200mV. The yellow box shows a zoomed-in figure where $comp3$ terminates the stimulation.

diode, D_{out}, which occurs during the charging phase of the inductor due to the change in polarity of the dual-layer capacitance. This, in turn, results in the current discharge into the ground. It is important that the electrode capacitance does not discharge during the cathodic phase, where we are interested in measuring the actual injected charge. It is not necessarily wrong for our design when it happens during the first counts of the anodic phase. However, it is critical that the diode will not be forward-biased when the residual voltage is close to zero volts because the conducting current will likely result in a false trigger of $Comp3$, compromising the charge balancing reliability. The charge metering scheme introduces negligible measurement inaccuracies due to switching delays as the results indicate that the charge unit capacitors charge from 0V to 202mV. The control circuit was implemented with ideal digital components and negligible time delays, and as mentioned earlier, we selected ultra-fast comparators with a 1ns propagation delay to minimize the control loop delay. We expect the FPGA selection will keep the control loop delay short, matching the simulation results.

Besides the fast circuit response, an error is introduced due to the bias current of the comparators. This difference can be seen by the discrepancy between the injected charge Q_{Cdl} and the programmed charge Q_{cm}. In the first case, we measure $493mV$ across the dual-layer capacitance at the end of the cathodic phase, that is, $493nC$ injected charge, while the charge balancing scheme estimates $Q_{cm} = 505nC$. The average bias current flowing out of the comparator is equal to $4.92\mu A$, and the cathodic phase lasts $1.089ms$; hence $Comp1, 2$ inject around $5.36nC$ additional charge. The inverting node of $Comp3$ also connects to V_{in} adding $5.36nC$ charge to the charge balancing scheme. This results in

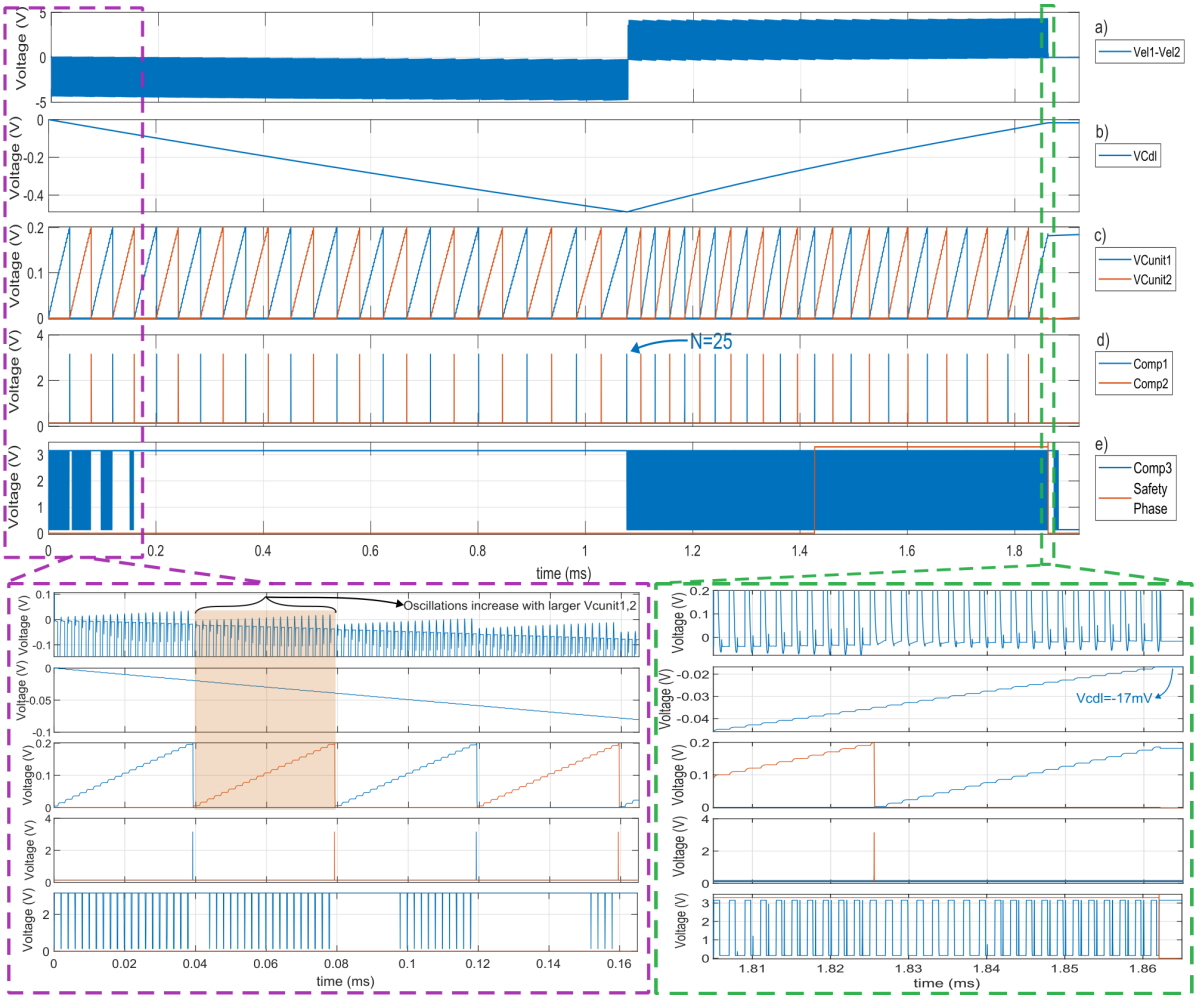

Figure 4.2: Simulated circuit functionality, including the component models used for the PCB implementation. a) Electrode-tissue interface voltage $V_{EL1} - V_{EL2} = V_{load}$. b) Dual-layer capacitance voltage. c) Voltage over sense capacitors. d) response of the charge-metering comparators ($comp1, 2$). e) Output voltage of the charge-balancing comparator and indication of *Safety Phase* state period. The purple box zooms at the first pulse, where toggling of the $Comp3$ occurs due to the oscillations at the output. Oscillations become larger for a larger voltage across $Cunit1, 2$ and C_{dl}, but the toggling of $Comp3$ fades off as the output voltage is superimposed on the V_{cdl}, which leads away from 0V. The green box zooms at the end of the stimulation, where the same behaviour occurs, as a result, the charge balancing stops the stimulation at -17mV.

$504nC$ measured value by the charge metering scheme, which is close to the $505nC$ mentioned before, assuming that $Vcunit1, 2$ shifts when the voltage is always equal to 202mV leading to this negligible discrepancy. The bias current error manifests as a gain error and increases for higher counts and lower stimulating frequencies as the integration time over the measuring capacitor increases. However, this error is predictable. We can either compensate by adjusting the number of counts to meet the required injected charge or use slower comparators with smaller bias current. From an application point perspective, this error should not matter as long as the charge linearly increases with the number of counts.

Contrary to the ideal behaviour of $Comp3$, where its output remains *HIGH* during the cathodic phase, it is observed that when component models are used, the output toggles until $0.16ms$. When the buck-boost converter injects charge at the output, a series RLC is formed, and as a result, a resonance occurs when the stimulation spike approaches zero volts. This resonance does not occur using an ideal diode with no recovery time, which is why we do not observe the same behaviour in Fig 4.1. The purple box in Fig. 4.2 shows that toggling starts at the beginning of the stimulation and occurs each time charge is injected into the tissue, at least for the first *charge packet*. For the following four counts, $comp3$ does not trigger at the first stimulation pulses because the resonance is small when the potential at the inverting node of $Comp3$ is low. As the potential increases, the resonance becomes more prominent, resulting

in the toggling of $comp3$. It is worth emphasizing that Fig. 4.2 shows the voltage across the electrode ($v_{EL1} - v_{EL2}$), which is slightly smaller compared to the differential voltage measured by $Comp3$.It is important to note that $Comp3$ does not precisely measure the ETI as it is connected at the nodes V_{LOW} and V_{HIGH}. Consequently, it can be observed that $Comp3$ triggers at a point when the voltage difference $V_{EL1} - V_{EL2}$ is lower than zero. This output behaviour was explained in Subsection 3.3.3. Intuitively, this effect can be thought of as if the stored energy at the output repels in order to preserve zero average voltage across the inductor L. Since the voltage across the dual-layer capacitor ramps up, the output voltage no longer oscillates below zero, and thus the output of $Comp3$ remains *HIGH*. Similarly, the green box zooms in on the graphs to illustrate the behaviour of the circuit during the anodic phase. In this case, the voltage across C_{dl} is reversed, and $Comp3$ measures a negative differential voltage when there is no current at the load, hence its output is *LOW*. When the charge is injected into the tissue $Comp3$ triggers *HIGH* since the differential voltage becomes larger than zero and decreases as the oscillation occurs. However, a second trigger is observed immediately after the first one due to the recovery time of the diode, which makes the non-inverting node slightly more positive. The stimulation eventually stops with a residual voltage of $-17mV$ since the measurement occurs during the recovery time of the diode. By introducing some delay at the sampling signal, the residual voltage can reduce to close to zero.

4.2. PCB Measurements in Linear Tissue Model

To validate the circuit operation, we have tested the PCB prototype with a linear load like the one used for the simulations, $C_{dl} = 1\mu F$ and $R_{tis} = 1k\Omega$. For the measurement set-up, we used a GW Instek GPP-4323 power supply to generate the three different supplies for the IC components, a $\pm 12V$ and $-5V$. We used a Tektronix 2014C oscilloscope with a 100MHz bandwidth and a 2GS/s sampling rate to measure the signals. To measure the injected charge across the load capacitance C_{dl}, we used a Pico Technology ta045 differential probe. To supply the AC input, we used a Rigol DG4202 waveform generator. The second channel was used to generate a square-wave signal in phase with the input to control the buck-boost switches. This signal was fed to the FPGA. The FPGA was powered by the laptop using a USB cable. Fig. 4.3 shows the measurement set-up block diagram. For the in-vitro measurements, the linear load was replaced by a pair of electrodes, and the differential measurement was performed across the electrodes.

Since the signal generator could not supply the required current, we used an AD822 op-amp as an external buffer to supply the buck-boost UHF stimulator, as shown in Fig. 4.3. This op-amp has a $3V/\mu s$ slew rate, resulting in distortion of the input signal when using a $500kHz$ frequency. Hence, the frequency was scaled down to $200kHz$ with a $1V_{pk-pk}$ input voltage for the following measurements.

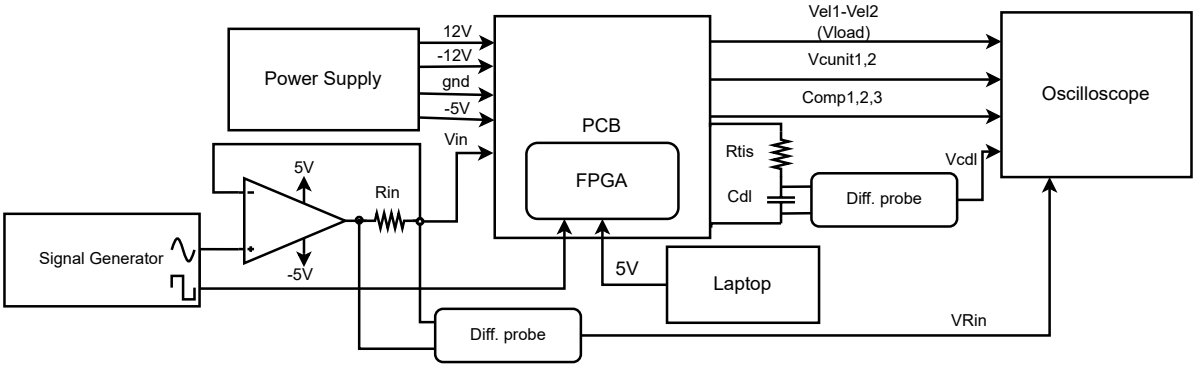

Figure 4.3: A block diagram for the measurements of the PCB using a linear electrode load. The test set-up consists of a power supply, an oscilloscope and a signal generator. A buffer is connected to the signal generator to obtain the required load current. Additionally, two differential probes were used to obtain the voltage across R_{in} and C_{dl}. These measurements were used to obtain the supplied current and charge, respectively.

Before starting the stimulation, the FPGA sets the state of the switches to ensure an initial condition for the comparators and zero volts across the measuring capacitors. Hence, S_{Dch1}, S_{Sh1} and S_{Sh2} are driven *HIGH* to connect nodes $V_{Cunit1,2}$ and V_{LOW} to ground. The H-bridge switches are left open to avoid charging the linear tissue model with the $Comp3+$ input bias current. For the charge balancing,

the total number of counts was set to $N = 14$, resulting in $280nC$ of injected charge for $V_{ref} = 200mV$ and $C_{unit1,2} = 100nF$. The waveforms for $V_{Cunit1,2}$ and V_{Cdl} are shown in Fig. 4.4. There are a few characteristics worth discussing.

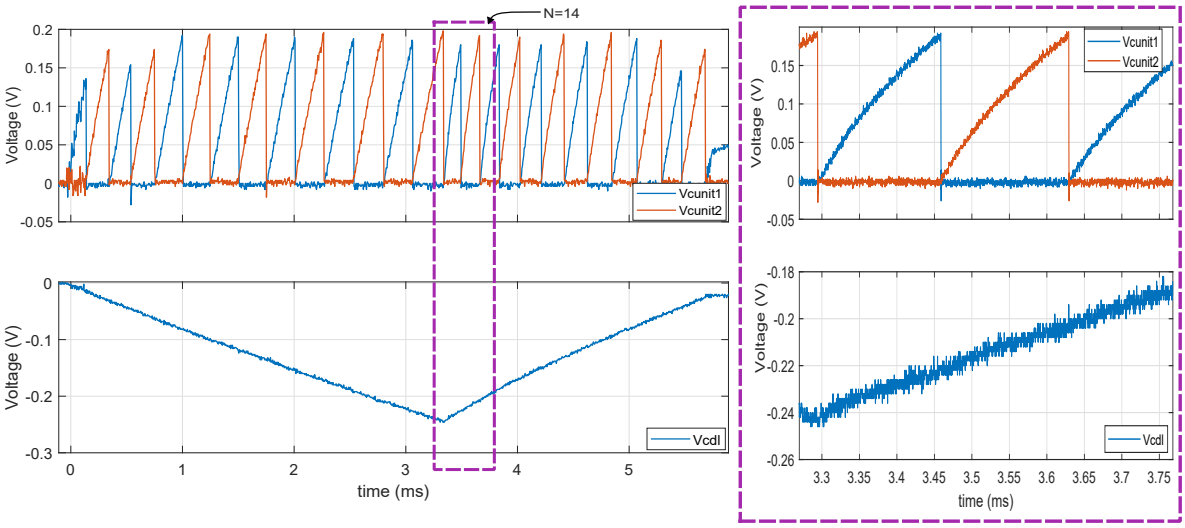

Figure 4.4: The voltage across the charge metering capacitors ($V_{cunit1,2}$) and across the double layer capacitor (V_{cdl}) of the linear electrode-tissue interface during a biphasic stimulation for $N = 14$ counts at the cathodic stimulation. The plot in the magenta box illustrates a shorter measurement for the last count during the cathodic and the two initial counts during the anodic phase to prove the sampling frequency limitation to capture the exact reference voltage.

Firstly, we would like to address the constraints imposed on the measurements by the oscilloscope. In Fig. 4.4, $V_{Cunit1,2}$ reaches a voltage inconsistent with each other, the trend becomes more evident at the beginning of the anodic phase where the rate of charging becomes faster. This behaviour is due to the limited sampling rate of the oscilloscope and becomes more pronounced for stimulation with a larger number of counts where data sampling must be done at larger time scales. To confirm this, we have captured the data for the last count of the cathodic phase and the first two counts of the anodic phase, shown within the magenta box in Fig. 4.4. The result indicates that the prolonged measurement in Fig. 4.4 fails to capture the $V_{Cunit1,2}$ peak value due to the limitation of the oscilloscope sampling frequency. Secondly, the voltage across the measuring capacitors $V_{unit1,2}$ does not reach the reference voltage during the first four counts. From our measurements, we have noticed that this behaviour correlates with the low voltage across the double-layer capacitor since it only happens at the start and end of the stimulation. As seen previously, at close to zero V_{Cdl}, $Comp3$ toggles due to the oscillations occurring at $V_{EL1} - V_{EL2}$ that is likely to interfere with the charge balancing finite state machine. There are two ways that $Comp3$ output can couple to $Comp1$ and $Comp2$. First, this can happen by the power supply, all outputs of the comparators are supplied by the 3.3V LDO. Additionally, it can couple through the FPGA pins. However, these signals occur in the nanosecond regime, which makes it hard to capture and safely answer the above hypothesis, thus, we support it with the following measurements. Initially, the $S_{cathode}$ state was configured to *HIGH* prior to the onset of stimulation. This action resulted in the generation of an offset voltage at the dual-layer capacitance due to the bias current, as depicted in Fig. 4.5. Since the V_{Cdl} starts at -52mV, the $Comp3$ stops toggling due to the oscillations, which likely stops the charge balancing switching.
Additionally, we inspected the correlation using $C_{unit1,2} = 10nF$ for the charge metering, meaning that more counts will be triggered simultaneously. Hence, according to the hypothesis, more counts will not reach the required threshold. Fig. 4.6 illustrates the $V_{cunit1,2}$, V_{Cdl} and $Comp3$ signal. As mentioned, the counts occur much faster and given the limited sampling frequency, it is challenging to conclude whether $V_{Cunit1,2}$ reaches the reference voltage. Therefore, Fig. 4.6 illustrated zoomed plots for the first four counts to obtain safer conclusions.

The yellow and green boxes show the first and second counts; It is observed that both V_{cunit1} and V_{cunit2} last approximately $3 \times T_{stim} \approx 15\mu s$. Each time the buck-boost converter injects charge into the tissue, $Comp3$ triggers *HIGH* followed by toggling and a metastable state. The oscilloscope fails to capture the V_{cunit1} and V_{cunit2} levels for the first two counts that reach $Vref = 200mV$. This becomes

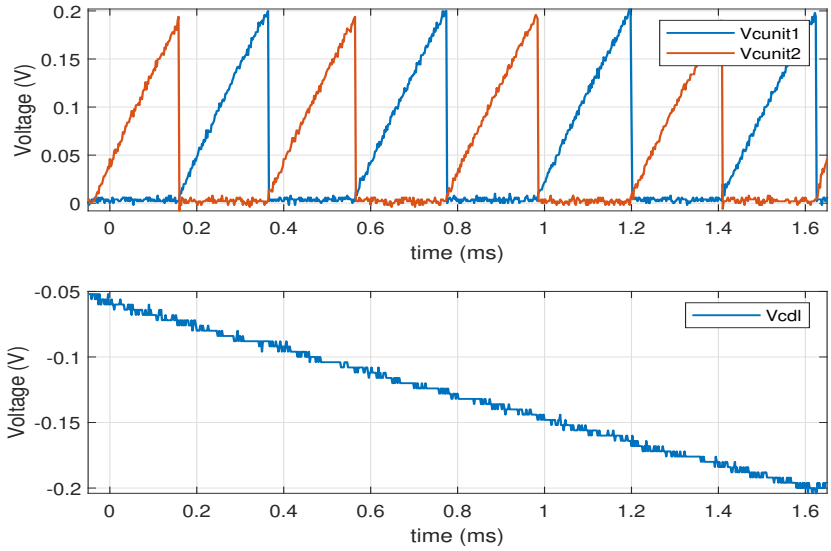

Figure 4.5: V_{cdl} starts with -52mV offset due to the bias current when the $Scathode$ is set to *HIGH* upon starting the stimulation. Starting the stimulation with an offset voltage results in the proper charge-balancing operation for the first pulses. The V_{cdl} offset stops the $Comp3$, which likely compromises the charge balancing reliability.

obvious by the stimulation frequency and the $Comp3$ signal indicating that the stimulator injects current, resulting in a correct channel change of the charge-metering. In contrast, the third and fourth counts shown in the magenta and blue boxes last for a non-integer value of the stimulation period. From Fig. 4.6, it becomes apparent that the channel shift occurs due to the oscillations of the $comp3$ output.

Another important consideration is that charge-balancing comparator $comp3$ stops the stimulation when the double-layer capacitor is in the range of $-15mV$ to $-20mV$, similar to the simulation value seen earlier. In literature, different values are reported for the water window that depends on the electrode material, size and stimulation parameters. For example, in [110], a 2mm Pt electrode immersed in PBS solution exhibited a water window from -0.6V to 0.8V. However, these values are significant and Faradaic reactions can occur at lower values. For this reason, stimulation devices consider the safety limits to range from $\pm 50mV$ to $\pm 100mV$ [111], [112], of which the absolute value is still higher than our obtained residual voltage. Similar to the previous discussion, we suspect that due to the RLC output and the non-ideal diode characteristics, some oscillations occur even at the beginning of the charging phase resulting in a false trigger that terminates the stimulation. In simulations, we introduced some delay to accurately sample the residual voltage and bring it back to zero. However, due to the timing constraints imposed by the FPGA, the HDL could not be synthesized when using additional delay.

Besides the inconsistency observed on the first pulses, the intensity linearity in response to the count number must remain the same. To verify it, we have measured the voltage across the dual-layer capacitor V_{cdl} for multiple counts ranging from 10 to 24, as shown in Fig. 4.7. Due to timing constraints on the FPGA, we could not synthesize the HDL for specific counts; thus, those measurements are not shown. The results in Fig. 4.7 indicate that the charge metering performs linearly with respect to count number. As previously mentioned, the charge balancing stops the stimulation around $-20mV$ for all the measurements. This inconsistency around the value indicates that the charge stored at both sides of the diode differs per stimulation resulting in recovery time changes. Thus, the value obtained by $comp3$ samples during each stimulation cycle exhibits a small degree of arbitrariness.

Moreover, as the residual voltage increases, we observe a non-linear behaviour. This behaviour occurs due to the diode's non-linear characteristics, and the effect becomes clearer for a larger injected charge. During the anodic phase, the capacitor reverses its polarity, and the diode becomes forward-biased during the buck-boost converter's charging phase, letting the capacitor discharge to ground. This is also the reason why the charging rate of the charge-measuring capacitors increases at the onset of the anodic phase. The diode conduction current decreases as the residual voltage decreases and the voltage across $C_{unit1,2}$ increases.

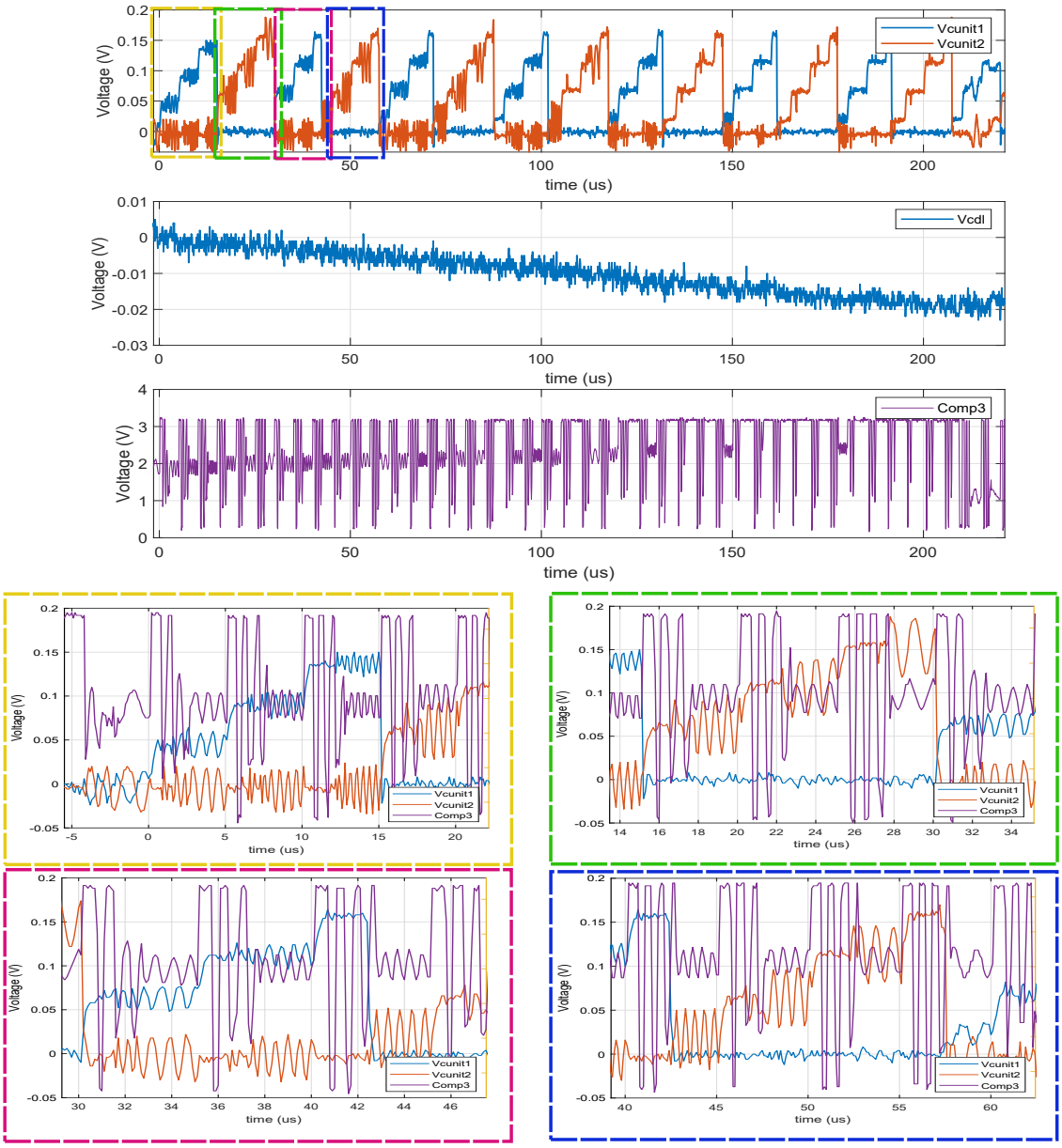

Figure 4.6: $Comp3$ response to charge metering operation for $Cunit1,2 = 10nF$ and dual-layer capacitor charging for $C_{dl} = 1\mu F$ and $R_{tis} = 1k\Omega$. The yellow and green boxes show the first two charge packets, which both last for approximately $3 \times 1/f_{stim}$ and stop at the next stimulation pulse, bringing the voltage equal to V_{ref}. The oscilloscope does not depict the accurate level. Still, the stimulation frequency and the wider $Comp3$ trigger imply it. The magenta and blue box show the third and fourth charge packet when the charge metering process is interrupted by the oscillations following the charge injection. This is evident by the $comp3$ output toggling in response to the oscillations and the arbitrary channel-changing time.

Another point worth mentioning is that the slope between some measurements varies. This is unexpected, given that the power input has remained constant for all the measurements. We suspect this behaviour could be a result of two things. First, as a result of a residual voltage at the dual-layer capacitance (C_{dl}) as the hold time between stimulation cycles was arbitrarily taken. This can result in different initial conditions between measurements and affect the charging process. The second consideration is that the power provided in the circuit is given by the buffer, which is limited by a finite gain bandwidth. Therefore, this makes the buffer unable to follow the sharp transitions resulting in a sharp peak at its output. This response could vary for each charging process resulting in an overall different power to the output.

To measure the accuracy of the charge metering, we generated a plot shown in Fig. 4.8 comparing

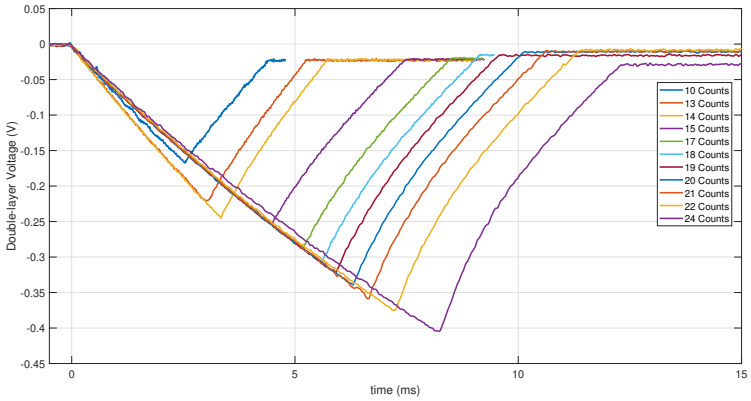

Figure 4.7: Dual-layer capacitor voltage for different counts indicating the stimulation intensity. The measurements were performed with $R_{tis} = 1k\Omega$ and $C_{dl} = 1uF$

the charge measured by the charge metering scheme Q_{cm} and the charge measured across the dual-layer capacitance Q_{cdl}. For some counts, we could not synthesize the HDL (i.e. 11, 12, 16 and 21); we have interpolated the data to show a linear trend. The results show an increasing linear trend for larger counts with small variability resulting from the stochastic error imposed on our measurement by the oscilloscope sampling frequency.

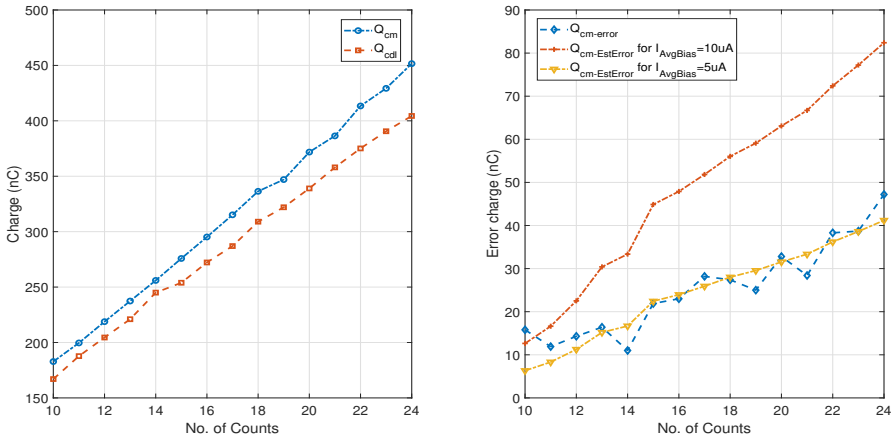

Figure 4.8: Stimulation intensities. Q_{cm} indicates the calculated charge as the sum of individual charge packets by the charge metering scheme. Q_{cdl} represents the actual charge measured across the dual-layer capacitance. The blue trace on the right plot shows the charge measurement error, $Q_{cm-error} = Q_{cdl} - Q_{cm-meas}$, and the red and blue trace show the estimated error for $10\mu A$, and $5\mu A$ $I_{Avg-bias}$ current, respectively.

Moreover, the results indicate a gain error as the charge metering measurement is 9.5% greater than the actual charge Q_{cdl} for $N = 10$ and 11.8% for $N = 24$. As previously discussed, this gain occurs by the bias current of $comp1$, $comp2$ and $comp3$. The datasheet for $comp3$ specifies that the bias current (I_{bias}) has a minimum value of $5\mu A$ and a typical value of $2.5\mu A$. Thus, a calculation of the bias current errors was made for both values. The charge metering $comp1, 2$ were connected alternately in the charge-metering scheme, contributing to the I_{bias} error. The non-inverting and inverting inputs of $Comp3$ were connected across the H-bridge V_{HIGH} and V_{LOW} node, respectively. The current injected by the non-inverting terminal was injected into the tissue and eventually measured by the charge metering scheme. However, the inverting terminal injected I_{bias} only to the charge metering scheme, increasing the error to $2I_{bias}$.

The time that the bias current integrates into the charge metering scheme can be used to approximate the error. From Fig. 4.7, it is known that the cathodic phase for $N = 10$ lasts 2.53ms. Thus, the error made by the charge-metering for the minimum bias current value of $10\mu A$ was calculated,

resulting in a $25.3nC$ error. The same calculations were carried out for all the number of counts and for both the minimum ($10\mu A$) and typical ($5\mu A$) bias current values as displayed in Fig. 4.8 with the red and yellow trace, respectively. As shown in red, the estimated error for $2I_{bias,min} = 10\mu A$ declines from the measured error for larger counts. However, as shown in yellow, the estimated error with $2I_{bias,typ} = 5\mu A$ fits better with the measurements, indicating a gain error of $2I_{bias,typ}$ will be included in the measured charge.

4.3. PCB Measurements in Vitro

To validate the proposed stimulator's functionality in vitro, we tested it using real electrodes immersed in a phosphate-buffered solution (PBS) to model the tissue environment. In Fig. 4.9, the stimulation waveform and the voltage across the charge-metering capacitors are shown for $N = 10$ and $Q_{cm} = 200nC$. The number of counts were reduced to capture the ultra-high frequency stimulation pulses applied to the electrode. A higher count number will result in a longer measurement time, making it more difficult for the oscilloscope to capture the stimulation pulses. Based on the results, it is expected that the electrode demonstrates similar impedance characteristics with the linear ETI.

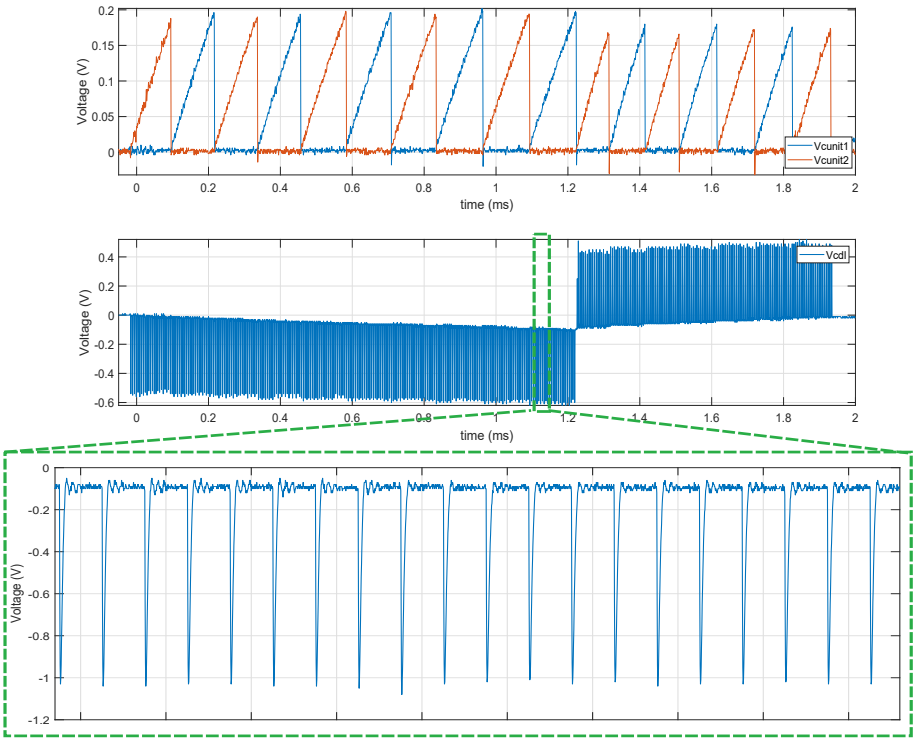

Figure 4.9: Stimulation waveform using real electrodes V_{load}, and the voltage across the charge-metering capacitors $Vcunit1,2$.

The measurements in Fig. 4.9 show that the stimulator can successfully apply ultra-high-frequency pulses and charge the capacitance of the electrode. From the magnitude of the stimulation pulse, we can estimate the capacitive part of the impedance given the measured charge. Neglecting the error introduced by the non-idealities, the injected charge Q_{Cdl} should be equal to Q_{cm}, that is, $200nC$. Therefore, given that the voltage build-up at the end of the cathodic phase is equal to $100mV$, we can estimate the capacitance to be equal to $C = Q/V = 2\mu F$. Moreover, we can estimate the resistance of the electrode. We know that in each cycle, the inductor is charged by $V_{in} = V_{peak}sin(2\pi f_{stim}t)V$, where $f_{stim} = 200kHz$, $V_{peak} = 0.5V$ and $L = 300\mu H$, the current stored on the inductor is given by:

$$i_L = \frac{1}{L}\int_0^{T_{stim}/2} V_{in}dt = \frac{1}{L}V_{peak}\frac{sin^2(\pi f_{stim}T_{stim}/2)}{\pi f_{stim}} \tag{4.1}$$

Equation 4.1, obtains the peak current stored on the inductor, which is equal to $2.7mA$. However,

the voltage integration occurs within a smaller period due to the switching delays, reducing the stored current. Moreover, the delays can result in power loss until the inductor discharges its stored energy to the output. Additionally, in our estimation, we did not consider the voltage drop across the switch used to charge the inductor, considering these assumptions, we can assume $I_{stim} = 2mA$. In order to accurately depict the peak output stimulation voltage, a shorter measurement was performed as shown in the green box in Fig. 4.9, where $V_{stim} = 0.9V$. Therefore, we can estimate the resistance to be equal to 450Ω.

The charge-balancing scheme stops the stimulation with a $-20mV$ residual voltage. This is similar to the residual voltage obtained in the simulation and measurements with a linear ETI. As previously discussed, $Comp3$ samples during the recovery time of the diode resulting in a false trigger. In the simulation, the residual voltage was brought back to zero by introducing an additional delay at the sampling time of $Comp3$. However, adding longer delay at the FPGA resulted in a non-synthesizable code due to violations of the time constraints.

4.4. Power Efficiency Analysis

The main goal of this thesis is to implement a topology that will efficiently inject charge into the tissue. Ultra-high frequency pulsed stimulation using inductive charging is a potential method that could achieve a theoretical efficiency of 100%. However, the implemented circuit suffers from conduction and switching losses that compromise the efficiency. In the following analysis, an estimation of the power efficiency will be given, and it will be validated with the simulation and measurement results. However, in the subsequent analysis, the gate charge losses are not included since the driving is done by the FPGA, which is powered by the laptop. Usually, in an IC, one power supply is used, responsible for driving the switches and providing the input power to the converter. Hence, the expression for the efficiency regarding the conduction losses is given by (4.2)

$$\eta_{cond} = \frac{P_{tis}}{P_{sw,bb} + P_{SW,H-b}} \tag{4.2}$$

$$\eta_{cond} = \frac{R_{tis} I_{stim}^2(t)}{R_{tis} I_{stim}^2(t) + 2R_{on,bb} I_{Ch}^2(t) + R_{on,bb} I_{stim}^2(t) + V_D I_{stim}(t) + 2R_{on,H-b} I_{stim}^2(t)} \tag{4.3}$$

Since the circuit operates in two phases with a varying current, its notation for the charging and stimulation phase current is $I_{ch}(t)$ and $I_{stim}(t)$, respectively. Hence, during the charging phase $I_{stim}(t) = 0$ while during stimulation phase $I_{ch} = 0$. Moreover, some charge is stored on the charge metering and the electrode-tissue interface capacitors. During the process of stimulation, it is possible to recycle the stored charge back to the circuit. However, the amount of energy that can be recovered is limited by the finite efficiency of the system and the electrical parameters of the electrodes [7][108]. For a good electrode design, there is not much charge build and thus possible to be recovered from the ETI. On the other hand, we have considered the voltage drop across the charge metering capacitors since it periodically tops to V_{ref} and shorts to ground. The average power lost due to the capacitor charging is expressed in (4.4).

$$P_{cm-avg} = V_{avg} I_{avg} = \frac{V_{avg} Q_{tot}}{T_{cath}} \tag{4.4}$$

Where the Q_{tot} is the total injected charge over the cathodic period T_{cath} and V_{avg} is the average voltage across the measuring capacitors, which is equal to $V_{ref}/2$. The average power dissipation is in the order of a few micro-Watts, while the average power dissipated in the electrode is in the order of a few milli-Watts.

For the efficiency measurements, we have considered the average energy transferred from the input source to the load for integer stimulation cycles. To obtain the input current, an 11Ω resistor was placed at the output of the buffer, and we measured the voltage difference across it using a differential probe. The resistor was placed within the buffer loop to correct for the voltage drop and supply the buck-boost converter with V_{in}, as shown in Fig. 4.3. Likewise, the power dissipation at the output was calculated by $\frac{1}{T} \int V_{load}^2 / R_{tis} dt$ using Matlab. As shown in Fig. 4.3, V_{load} was measured with a differential probe. The measurements were obtained for various loads (i.e. 500Ω, 680Ω, $1k\Omega$, $1.8k\Omega$),

and different input voltages, while the input frequency was kept fixed at $200kHz$. The results are shown in Fig. 4.10. As expected, the efficiency is higher for larger tissue resistance values since it dominates the conduction losses involved in the power conversion. As the resistance decreases, the on-resistances of the switches dominate the power losses. Similarly, the more energy is conveyed for larger input voltages, the less critical the conduction losses become. Moreover, the output voltage depends on both the input voltage V_{in} and the tissue resistance R_{tis}, hence, the measurements for $R_{load} = 1.8k\Omega$ were stopped when the peak voltage reached $5V$. Exceeding this voltage could result in the conduction of the safety diodes of the buck-boost converter or even damage the IC.

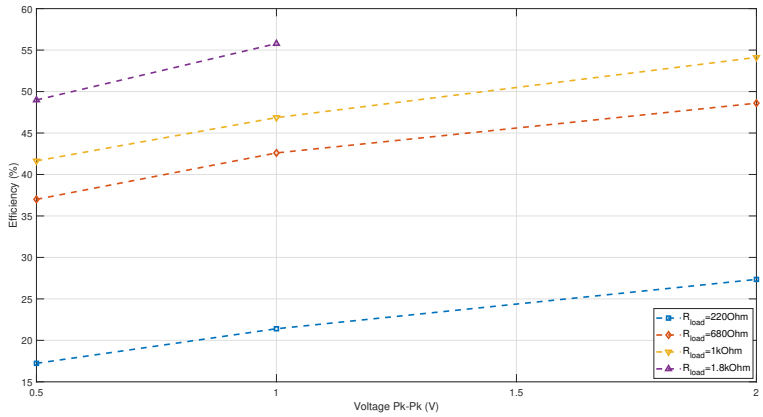

Figure 4.10: Measurement of the power-conversion efficiency.

As various power supplies provide power to the IC components, it is possible for a portion of the load power to be supplied as leakage energy. Although it is not anticipated that this leakage energy will have a significant impact on the charge injected into the tissue, we have performed simulations to precisely replicate the experimental setup. The results, shown in Fig. 4.11, follow the measured values with a slight overestimation. This overestimation is owed to a few things; First, the passive components used in the simulation are ideal and purely reactive, increasing the power savings compared to the actual circuit. Second, the simulations were done with minimal parasitic capacitance ($C_{par} = 1fF$) between the nodes and the ground. On the PCB, the actual capacitances between the nodes and ground are higher, and for each period, these nodes are charged and discharged, resulting in an efficiency drop. Additionally, the finite trace length increases the inductance on the signal path, negatively affecting the circuit's efficiency. This becomes especially relevant in ultra-high frequency pulsed stimulation where di/dt results in voltage drop across the power path. Finally, unlike the actual measurement, the $R_{load} = 1.8k\Omega$ were simulated for all V_{in} since the switches did not clip to the power supply.

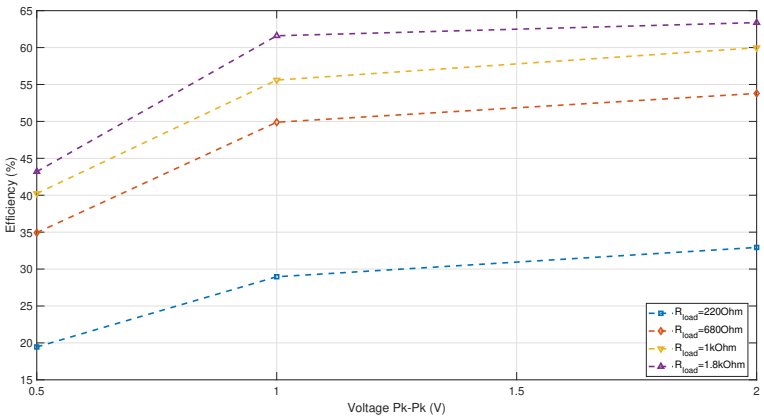

Figure 4.11: Simulated efficiency using the manufacturer component models

The present chapter presents the outcomes of a study that aimed to evaluate the feasibility of a UHF pulsed stimulator concept. The measured results indicate that the proposed charge metering and balancing schemes can provide effective and safe stimulation. Moreover, the peak efficiency of the circuit, which was the primary objective of the study, was found to be 55%, demonstrating the potential of an alternative stimulation paradigm.

In the upcoming chapter, the possibilities and limitations of the design will be discussed, and the efficiency of the UHF pulsed stimulator will be compared with other stimulator types.

5

Discussion & Conclusions

5.1. Discussion

The main research question in this thesis is whether using a circuit that directly relays the available energy from the wireless link into the tissue without intermediate filtering can increase the power efficiency in wirelessly-powered neurostimulation for chronic migraine and cluster headache patients. Based on the existing literature, inductively wirelessly-powered neurostimulators use a rectifier and a switched-mode power converter to regulate the received voltage into a constant power supply. The current methods inject constant current into the tissue. In the case of constant-mode stimulation, they do that with a current source at the output, while for a voltage-mode stimulator, a well-controlled power converter is required to track the changes in the current and account for them. However, the efficiency depends on the voltage ratio between the power supply and the tissue voltage and any difference will result in excess energy dissipation. Even more, this dependency can lead to lower efficiency, especially for multichannel stimulation, where the impedance of each channel is different. In the case of voltage-mode stimulation, the charge controller should be done for each channel individually, making the system's scalability more challenging. On the contrary, UHF pulsed stimulation has proven effective in neuron excitation and omits the voltage dependency at the output. Therefore, in this work, we have adapted this method to receive energy directly from the coil and inject it into the tissue, bypassing the conversion stages mentioned before. Finally, to obtain a well-controlled physiological response, the neurostimulator should be able to control the injected charge. Regarding safety, the charge accumulated at the ETI should be recovered back to zero after stimulation to avoid tissue and electrode damage. The study explores whether using a single circuit can improve the power efficiency by reducing the number of components and provide an effective and safe neurostimulation solution.

5.1.1. Charge metering

A novel charge metering scheme, presented in [107], was adapted to our neurostimulator circuit. The charge-metering circuit uses two capacitors to integrate the current into a voltage that represents the injected charge and two comparators to perform as a 1-bit ADC when a voltage reference is reached. By adjusting the comparator output counts N, the reference voltage V_{ref}, and the measuring capacitance value $Cunit$, we can adjust the total injected charge $Q_{Cdl} = N \times C_{unit} \times V_{ref}$. In this design, $Cunit = 100nF$ and $V_{ref} = 200mV$ were selected for $N \in [10, 24]$ resulting in $20nC$ charge resolution. Furthermore, this topology can be further reduced to a one-channel current integration by exploiting the charging time of the inductor. This leads to a reduction in the number of components required, resulting in the use of only a single capacitor and a comparator.

The measurements of the charge metering circuits have shown the ability to control the charge in linear ETI model and in *in-vitro* measurements. However, we have discussed that the delay of the control loop time, the bias current of the comparator, the parasitic capacitance introduced by the switches and the comparators and the switching artefacts due to the switches can limit the accuracy of the circuit. Therefore, those specifications must be taken care of when designing an IC. Our measurements indicated that the bias current of the comparator was the primary source of gain error, accounting for 11.8% when $N = 24$. The circuit could measure (Q_{cm}) a charge range from $182nC$ to $450nC$, including

the abovementioned error, while the measured injected charge across the dual layer capacitance Q_{cdl} ranged from $167nC$ to $404nC$. However, both values are smaller than the ideal injected charge, and this discrepancy occurs due to the charging of the parasitic capacitance at the nodes of the buck-boost converter, the H-bridge and the charge metering scheme. The tolerance of the measuring components will also add to the discrepancy between the measured and the ideal value. Besides the error due to the non-linearities, the system demonstrated a linear trend against the changes in the count number, which is essential when a physician uses the device to adjust the parameters empirically.

Testing the circuit with a smaller measurement capacitor, $Cunit = 10nF$, and $V_{ref} = 200mV$ resulted in oscillations by $Comp3$ since the charge rate of $Cunit$ was increased. A smaller unit capacitor translates to a higher potential at the input nodes of the $Comp3$ before the residual voltage of the dual layer increases. As a result, the oscillations at the output, due to the RLC, grow, resulting in toggling output. The fast-rising signal couples to the FPGA pins and interferes with the charge metering FSM. A feedback loop should be used to add hysteresis and avoid oscillations at the output of $Comp3$.

5.1.2. Charge Balancing

In this circuit, the charge balancing scheme consists of $Comp3$ that is connected across the load. While $Comp3$ is continuously connected to the load, only the data acquired at a frequency of f_{stim} are utilized by the FPGA, with the resolution of the charge balancing being dependent on the specific stimulation and electrode parameters. For $f_{stim} = 200kHz$, $V_{in-peak} = 1V$, $R_{tis} = 1k\Omega$ and $C_{dl} = 1\mu F$, the system obtains a resolution of approximately $400\mu V$. However, due to the limited delay that the FPGA could generate, $Comp3$ could only sample the voltage across the load during the beginning of the charging phase, which was affected by the recovery time of the diode resulting in earlier termination of the stimulation. Thus, the residual voltage obtained in the measurements ranged between $-16mV$ to $-20mV$.

Since $Comp3$ is connected across the load during all the stimulation phases, it makes the output trigger in response to every input activity and interferes with the charge metering. More specifically, it was encountered during the first and the last counts of the cathodic and anodic phases, that the $Comp3$ output will toggle in response to load oscillation as a result of the stimulus. The unpredictable output response is undesired because it could lead to the following hypothetical scenarios. Firstly, it can generate oscillations that couple through the FPGA pins, resulting in glitches on the designed FSM. Secondly, depending on the layout of the PCB, the noise can also couple between the ICs, generating EM interference and compromising the reliability of the circuit. For instance, in our layout shown in Fig. 5.1, the output of $Comp3$ is traced over the 3.3V power supply routed along the ground plane, as indicated by the green arrow. Similarly, the outputs of $Comp1$ and $Comp2$ are routed over the same trace, which capacitively couples them with $Comp3$. Therefore, when the $Comp3$ output toggles, it can generate a current along the power supply trace proportional to $C_{coupled} \cdot dV/dt$. With a very conservative $C_{coupled}$ value of $1fF$ and $1ns$ rising time, a $3.3\mu A$ current can couple through the trace, which could interfere with the sensitive FPGA input pins. There are a few suggestions that would mitigate this effect. If it is not feasible to avoid overlapping sensitive and fast-rising signals, or implementing a 4-layer PCB is not possible, it is advisable to include a decoupling capacitor next to the cross-sectional area. The exposed power trace has the potential to behave as an inductor, thus, it is beneficial to include filtering in the proximity where the two traces interact.

Furthermore, to mitigate any potential issues caused by EMI and maintain signal integrity, it is advisable to use a slower comparator to limit the bandwidth of the board. It is worth noting that the input of the comparator remains connected during the entire stimulation process. Hence, when designing an IC, it is preferable to enable and disable the comparator using a control signal to prevent the output of $Comp3$ from responding to its input and thereby reduce power dissipation.

5.1.3. Digital Control

For the digital part, a CMOD S7 was used with a clock frequency of $12MHz$, and five main FSM codes were created to complete the functionality of the circuit; two for the charge metering, one for the counter, one for the charge balancing and one for the stimulation.

Initially, the output signals of two comparators, $Comp1$ and $Comp2$, demonstrated a metastable output, resulting in unreliable signal counting. In an attempt to correct the issue, the output signals were fed into two cascaded D flip-flops to synchronize the signal and generate a clear logic *HIGH*. However, this approach did not resolve the issue either. For that reason, the clock frequency was

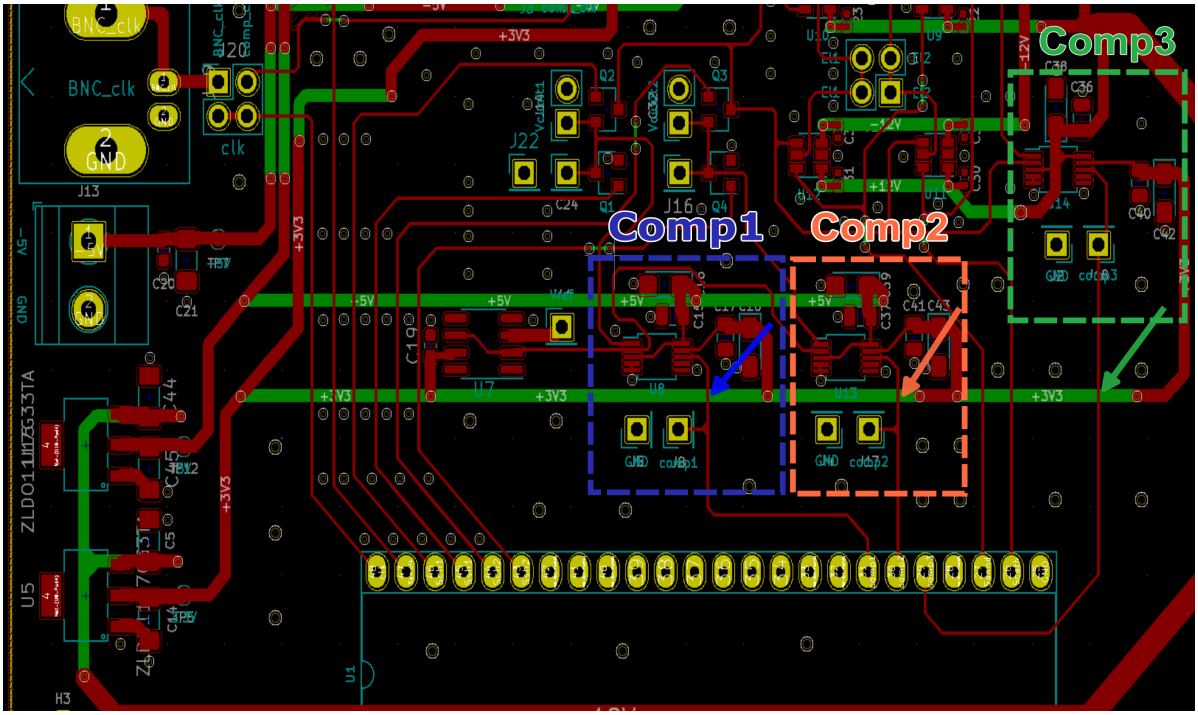

Figure 5.1: The layout of the PCB. The output traces of $Comp1$, $Comp2$, and $Comp3$ are routed over the $3.3V$ power supply, as shown with the blue, orange and green arrows, respectively. At the points where the nodes intersect, the power supply node is unfiltered, which can act as an antenna that couples energy caused by the oscillations of the output node of $comp3$.

increased to 300MHz, and two additional FSMs were designed, with four states each. By doing so, the output signals of $Comp1$ and $Comp2$ were sampled, and an output *HIGH* was generated by the FSMs if the input signal was *HIGH* regardless of its metastable condition. This approach enabled the generation of a reliable signal that could be accurately counted. The operation of the FSMs is as follows: it first starts from the *IDLE-PG-c1,2* state. When *btn2* is $HIGH$, it transitions to the *Initial-stand-c1,2* state. If $comp1,2$ output triggers *HIGH* within twenty-one clock cycles, it outputs *comp1-reg-reg-1p* equal to *HIGH* and then moves to the *Wait-loop-c1,2* state for seven clock cycles and drives the signal *LOW* before returning to the *Initial-stand-c1,2* state. Thus, the output generated by the FSMs was used as input to the counter for charge metering.

Increasing the frequency to 300MHz introduced timing limitations since the circuit could not process all the operations in one clock cycle. This is why some designs with different count numbers could not be synthesized (i.e. N: 11, 12, 16, 23, 24, 25). The most straightforward solution for this issue is to scale the clock frequency lower and adjust the timer registers introduced in *Comp1-reg-reg-1p* and *Wait-loop-c1,2*. By using a lower frequency, the allowed time for the digital circuit to complete an operation is increased. Although this solution could relax the time constraints, the relation operators introduced for the time register in different states of the FSM also impose complexity and slow down the digital circuit. To improve the performance, the relation operators should be broken down into smaller stages to minimize the complexity and allow for parallel processing in different pipeline stages, increasing the overall processing speed. As explained in Subsec. 3.4.2, relation operators are used in all main FSMs, therefore, adding pipelining stages should be applied to all of them to improve the time constraints.

5.1.4. Power Efficiency

The goal of the project was to improve the total efficiency of the stimulator by bypassing the power conversion stages used in conventional power management schemes and directly stimulating the tissue with non-regulated energy. By doing so, first, we hypothesized that the power conversion efficiency would increase since only one circuit is used. Moreover, the circuit can omit the off-chip filtering capacitors used at the output of the rectifier and the switched-mode power converter. Besides the increase of the area resulting from those capacitors, they also require complex circuitry to charge them adiabatically and preserve the efficiency of the system. Therefore, our topology uses a buck-boost converter

that utilises an inductor to flux energy and discharges it into the tissue. By fluxing the inductor only once at f_{res}, more specifically during the positive cycle of the sine wave, it effectively acts as a resistance that draws current from the LC tank. As a result, the efficiency of the system increases compared to the conventional system since only one buck-boost converter is used.

Additionally, the defluxing of the inductor makes the system independent of the driver losses that would otherwise be present if a current source were used. Alternatively, as mentioned, a capacitor should be controlled adiabatically in the case of a voltage mode stimulation. Furthermore, the stimulation is current-steered since the inductor directly discharges into the tissue. Therefore, by controlling the flowing current to the inductor, we control the injected charge into the tissue without depending on the tissue load. This method allows the stimulator to work with different electrode types and multiple channel configurations. However, in this design, care should be taken at the layout of the device to keep the parasitic capacitance at the output low and thus minimise the gate charging losses.

Our circuit was measured for V_{in} ranging from $0.5V_{peak}$ to $2V_{peak}$ and different $Rtis$: 220Ω, 680Ω, $1k\Omega$ and $1.8k\Omega$. For $R_{tis} = 1.8k\Omega$, the input voltage was limited to $1V_{peak}$ to avoid damaging the analogIC switches. The efficiency of the system increased for higher loads as the conduction losses impacted less, and the circuit demonstrated a peak efficiency of 56% with the measured values being in line with the simulations.

The efficiency of current mode stimulators is dependent on various factors, such as the number of channels, the impedance of the electrodes, and the target stimulation intensity. A rough estimate for a current mode stimulator is that it typically requires a current output of a few milliamperes to generate a sufficient stimulation potential at the tissue. However, this is just a rough estimate and the actual efficiency can vary significantly based on the specific requirements and constraints of the application. Additionally, the power management employed in WPT systems adds to the losses of the system. For example, the first circuit in a stimulation system is a rectifier that converts the AC signal to DC. Its efficiency is poor due to large voltage drops or increased reverse currents. However, an active rectifier with offset control can achieve a peak measured efficiency of 80%, as demonstrated in [113]. A switched-mode power converter is used after the rectifier to regulate the voltage to a fixed supply, which can achieve an efficiency of about $80 - 90\%$. Subsequently, we will calculate the theoretical efficiency of the neurostimulator with the fixed and adaptive power supply and compare it with the measured efficiency of our stimulator. For that purpose, we will consider two current drivers, a source and a sink, that provide a bipolar stimulation pattern. In order to estimate the efficiency of a current-mode stimulator with a fixed power supply, we will consider the linear model of the ETI with a series connection of R_{tis} and C_{dl} representing the tissue resistance and the double-layer capacitance, respectively, and the current sources providing the current through it, as shown in Fig. 5.2 a). On the other hand, Fig. 5.2 b) shows the stimulation current and voltage waveforms across the ETI for a biphasic stimulation with a pulse width of T_{stim}. The power transferred to the load during the cathodic and anodic stimulation can be expressed by the instantaneous power dissipated across the tissue resistance R_{tis} and the power provided to charge and discharge the dual-layer capacitance C_{dl} integrated over a stimulation cycle, as shown in Equations (5.1) and (5.2) for the anodic and cathodic phase, respectively.

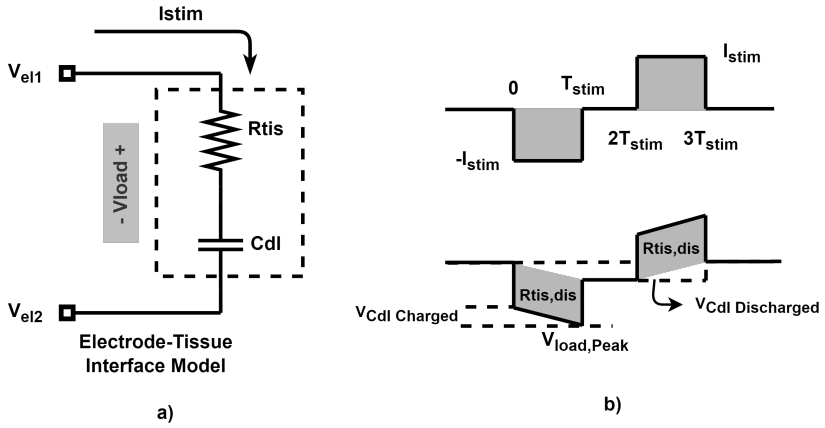

Figure 5.2: Simplified load model for efficiency analysis. (a) Linear ETI model with tissue resistance (R_{tis}) and dual-layer capacitance (C_{dl}). (b) Stimulation waveforms for current-mode stimulation.

$$P_{tis(cathodic)} = \frac{1}{T_{stim}} \int_0^{T_{stim}} -I_{stim}(I_{stim}R_{tis} - \frac{I_{stim}}{C_{dl}}t)dt \\ = I_{stim}^2 R_{tis} + \frac{I_{tis}^2}{2C_{dl}} T_{stim} \tag{5.1}$$

$$P_{tis(anodic)} = \frac{1}{T_{stim}} \int_{2T_{stim}}^{3T_{stim}} I_{stim}(-\frac{I_{stim}}{C_{dl}}T_{stim} + I_{stim}R_{tis} + \frac{I_{stim}}{C_{dl}}(t - 2T_{stim})dt \\ = I_{stim}^2 R_{tis} - \frac{I_{stim}^2}{2C_{dl}} T_{stim} \tag{5.2}$$

Therefore, the efficiency of stimulation power, with a fixed supply voltage VDD, is determined by the ratio between the power transferred to the load and the power drawn from the supply rails,

$$\eta_{fixed} = \frac{P_{tis(cathodic)} + P_{tis(anodic)}}{P_{sup}} = \frac{2I_{stim}^2 R_{tis}}{2I_{stim}V_{DD}} \\ = \frac{I_{stim}R_{tis}}{V_{DD}} \tag{5.3}$$

In the context of an adaptive power supply, the supply voltage (V_{DD}) can be expressed as $V_{DD,Adapt} = V_{tis}+V_{Cdl,peak}+V_{Compl}(t)$, where V_{tis} represents the voltage drop across the tissue, $V_{Cdl,peak}$ represents the peak voltage across the charged dual-layer capacitor, and $V_{Compl}(t)$ represents the time-dependent voltage compliance. Substituting the traditional V_{DD} with $V_{DD,Adapt}$ allows for the evaluation of the efficiency of the neurostimulator with an adaptive power supply. The efficiency of the neurostimulator with an adaptive power supply can be expressed as follows.

$$\eta_{adapt} = \frac{I_{stim} * R_{tis}}{V_{DD,adapt}} = \frac{I_{stim}R_{tis}}{V_{tis} + V_{V_{Cdl,Peak}} + V_{Compl(t)}} \tag{5.4}$$

The neurostimulator described above functions by providing constant current to the target tissue using a fixed and adaptive power supply. In the work by Arfin et al. [7], a Switched-Mode Power Converter (SMPC) was developed to regulate the current output based on changes in V_{load}, thus reducing losses in the electrode resistance. To reverse the current polarity for the anodic phase, the duty cycle is inverted, and an additional capacitor C_{mid} is used to increase the voltage of V_{El2} to V_{mid}. This enables the stored charge at the C_{mid} and the dual-layer capacitance C_{dl} to be recovered and results in efficiency enhancement. To calculate the efficiency, the power required is estimated by integrating the power of the ETI and the stored energy in C_{mid}. The energy injected into the ETI experiences losses due to the finite efficiency of the SMPC. To determine the energy consumed by the SMPC, the energy components are divided by its efficiency, η_{SMPC}. Thus, the supplied power during the cathodic phase can be given by Equation 5.5.

$$P_{cath} = \frac{1}{T_{stim}} \int_0^{T_{stim}} \frac{1}{\eta_{Adiab,SMPC}} \left(V_{mid}I_{stim} + I_{stim}^2 R_{tis} + \frac{1}{2C_{dl}} I_{stim}^2 t\right)dt \\ = \frac{1}{\eta_{Adiab,SMPC}} \left(V_{mid}I_{stim} + I_{stim}^2 R_{tis} + \frac{1}{2C_{dl}} I_{stim}^2 T_{stim}\right) \tag{5.5}$$

During the anodic phase, power is recovered from the mid-rail supply voltage V_{mid} and the dual-layer capacitance C_{dl}, with a fraction dissipated across the tissue resistance. To estimate the energy returned to the power supply, we can multiply the power components by the efficiency of the SMPC, denoted as η_{SMPC}. Therefore, the following equation can be used to express the power returned to the power supply during the anodic phase.

$$P_{anod} = \frac{1}{T_{stim}} \int_{2T_{stim}}^{3T_{stim}} \eta_{Adiab,SMPC}\left(- V_{mid} I_{stim} + I_{stim}^2 R_{tis} + \frac{1}{2C_{dl}} I_{stim}(t - 2T_{stim})\right) dt$$
$$= \eta_{Adiab,SMPC}\left(- V_{mid} I_{stim} + I_{stim}^2 R_{tis} - \frac{1}{2C_{dl}} I_{stim}^2 T_{stim}\right) \quad (5.6)$$

$$\eta_{VCS,Adiab} = \frac{P_{tis}}{P_{sup}} = \frac{2I_{stim}^2 R_{tis}}{P_{cath} + P_{anod}} \quad (5.7)$$

To evaluate and compare the different stimulation methods, a stimulation scenario was devised for a low-density electrode array. The simplified RC model depicted in Figure 5.2 was utilized, with electrode parameters set to $R_{tis} = 1k\Omega$, $C_{dl} = 1\mu F$, and a stimulation phase period of $T_{stim} = 400\mu s$. These selected electrode parameter values were derived from [108], which employed an iridium oxide electrode. For the fixed power supply, the voltage potential was set at $V_{DD} = 12V$, while for the adaptive power supply, $V_{tis,peak}$ was quantized for its full range with a resolution of $N = 4$. An offset on the quantized value was added for the current source compliance voltage, set at $V_{compl} = 200mV$, as shown in Figure 5.3a.

The efficiency of each method was evaluated and compared as a function of the stimulating current, ranging from $0 - 10mA$. Fig. 5.3b shows the efficiency of each method based on the analysis made above. However, in wireless power transfer, the power management is done by the rectifier and the SMPC to provide either a fixed or adaptive power supply. For the rectifier, we assumed an efficiency $\eta_{rect} = 80\%$ and for the SMPC, we assumed $\eta_{SMPC} = 90\%$. In contrast, for the adiabatically driven SMPC used in [7], we used the reported $\eta_{Adiab,SMPC} = 50\%$. Hence the total efficiency of a wireless-powered stimulator with a fixed, adaptive and adiabatically driven power supplies is given by Equations (5.8), (5.9) and (5.10), respectively.

$$\eta_{Fixed,WPT} = \eta_{rect} \times \eta_{SMPC} \times \eta_{Fixed} \quad (5.8)$$

$$\eta_{Adapt,WPT} = \eta_{rect} \times \eta_{SMPC} \times \eta_{Adapt} \quad (5.9)$$

$$\eta_{Adiab,WPT} = \eta_{rect} \times \eta_{VCS,Adiab} \quad (5.10)$$

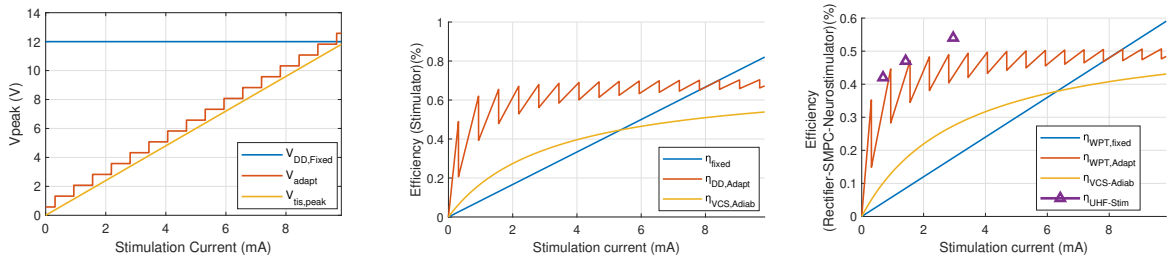

(a) (b) (c)

Figure 5.3: (a) Fixed supply (V_{DD}), adaptive power supply $V_{DD,Adapt}$ and the peak tissue voltage ($V_{tis,peak} = V_{tis} + V_{cdl}$) vs. the stimulation current (I_{stim}). (b) Neurostimulator power efficiency for fixed (V_{DD}) and adaptive power supply ($V_{DD,Adapt}$) and $V_{VCS,Adiab}$ vs. stimulation current (I_{stim}). (c) Total efficiency, including the efficiency of the wireless power management scheme. Calculations were based on the following parameter: $V_{DD} = 12V$, $R_{tis} = 1k\Omega$, $C_{dl} = 1\mu F$, $T_S = 400\mu s$ and a 4-bit resolution for the adaptive power supply.

Moreover, the measured efficiency of the UHF stimulation was plotted. The stimulating current for the measured UHF stimulator efficiency corresponds to the peak current measured at its output. There are a few noteworthy points to consider regarding this value. Firstly, the measured values are lower when compared to the expected value and the current measured on the inductor, which can be attributed to the transition losses. Additionally, due to the frequency scaling required to accommodate switch delays, the neurostimulator remains inactive for half of the period (i.e. $2.5\mu s$), resulting in a low average current value. As illustrated in Figure 5.3c, the UHF method demonstrates an improvement in

efficiency compared to other methods where the total efficiency is impacted by the power management circuits and the neurostimulator efficiency. However, it is essential to note that this is not a direct comparison between systems. For example, the UHF circuit was implemented in a PCB with a much lower frequency than what it was designed for.

5.2. Conclusion and Contribution

The development of a miniaturized, long-lasting medical device for stimulating the occipital and supraorbital nerves is required to suppress the pain of patients suffering from chronic migraine and cluster headaches. The device must be designed to be wireless, have the ability to control the injected charge, and have a small residual charge at the end of a stimulation cycle to ensure efficacy and safety. The limitations of conventional systems, such as AC-DC conversion and stimulator stage efficiency, and the lack of charge control in voltage-mode stimulation, must also be taken into consideration during the design and development process. The end goal is to create a device that is both effective in relieving pain and safe for patients to use.

This thesis presented the design and development of a novel inductively powered UHF neurostimulator. The design uses an inductor to store energy from the link and make a voltage-to-current conversion to inject charge into the tissue. A symmetric topology was also studied, but it was concluded that the original circuit was a better option for the operating distance of the implant. The circuit also includes two channels that measure the charge across measuring capacitors $Cunit1,2$ and two comparators. To detect whether the voltage across the capacitors reached the reference voltage level. By adjusting the number of counts, the injected charge $Q_{Cal} = N \times Cunit1,2 \times V_{ref}$ also changes, this modification is necessary to ensure that the injected charge meets the required threshold for nerve stimulation. A charge balancing scheme, using an additional comparator, $Comp3$, is adapted to prevent charge accumulation across the electrode-tissue interface. The proposed design was successfully designed and tested on a PCB, demonstrating its feasibility as a proof of concept.

The circuit was tested using a linear model of the electrode-tissue interface, with a resistance R_{tis}, of $1k\Omega$ and dual-layer capacitance C_{dl} of $1\mu F$. The results showed that it was effective in controlling the injected charge. With a sensing capacitor of $100nF$, a reference voltage of $200mV$, and N ranging from 10 to 24, the prototype measured stimulation intensities from $182nC$ to $450nC$. The measurements showed an increase of 9.4% and 11.8% for N=10 and N=24, respectively, compared to the injected charge (167nC to 404nC), reflecting the gain error due to the input bias current of the comparator, which corresponds to the estimated charge error caused by the bias current. The parasitic capacitance of the board led to a 16% offset in the measured values compared to the ideal values. Moreover, using a smaller measuring capacitance caused larger oscillations at the output and toggling of $Comp3$, leading to a larger discrepancy between the measured and injected charge due to an earlier shift in the charge metering channel. Finally, the charge-balancing circuit effectively reduced the residual voltage within the safe range. For the tested range, residual voltages from $-20mV$ to $-16mV$ were obtained. The charge balancing effectiveness was also measured using real electrodes, obtaining a residual voltage of $-20mV$. Those values are well within the strict safety limit of $-50mV$.

In the final analysis of the implemented circuit, the power efficiency was evaluated, and the results indicated that the design showed improved efficiency compared to conventional wirelessly-powered neurostimulators across a wide range of stimulation parameters and tissue impedances. However, it is important to note that the definition of efficiency utilized in the evaluation was based only on an electronic perspective. As a result, it must be acknowledged that charge threshold parameters and waveform stimulation efficiency may deviate from a biological point of view.

In conclusion, the implemented novel design achieved efficient stimulation while preserving effectiveness and safety. This works adds a new approach to the existing knowledge on developing efficient wirelessly-powered neurostimulators.

5.3. Recommendation for Future Work

- **Design and test the neurostimulator using the wireless link:** In the initial design phase of the topology in question, a wireless power link was proposed and evaluated through simulation to assess its efficiency. However, the implementation of this wireless link was omitted in the final PCB design to reduce complexity and facilitate the characterization of the board. Nonetheless, to fully validate the functionality of this topology, it is imperative to incorporate the wireless link

and perform comprehensive characterization and testing with the neurostimulator.

- **Wireless data transfer:** In order to improve the system design in the future, a wireless communication link needs to be incorporated to allow for data transfer between the transmitter and receiver. This will enable the ability to adjust the input power and stimulation parameters based on fluctuations in the coupling.
- **Energy efficiency of UHF pulsed stimulation:** The current work only evaluates the efficiency of the UHF pulsed stimulation from a circuit perspective and makes certain assumptions that may not hold true in real-world conditions. In reality, the electrode-tissue interface is a non-linear load, and charge transfer occurs through two mechanisms. This means that relying solely on Ohm's law may result in incorrect conclusions. To accurately assess the efficiency of the UHF stimulation, an analytical study must be performed using a neuron model that considers the biological effects. Additionally, the stimulation parameters used in this work were based on values commonly used in current-mode stimulation and derived from the strength-duration curve. However, it is important to note that the strength-duration curve depends on the stimulation parameters, and as such, it must be revised for other waveform stimulation techniques.
- **Multichannel stimulation:** The UHF stimulation topology allows for the use of multiple channels by alternating the current flow to different electrodes. To maintain the scalability of the charge metering circuit, time-interleaving should be performed only after completing a full charge count. To do this, the count needs to be registered for each individual electrode used for stimulation. This operation was not implemented in the current prototype, but future revisions should incorporate additional switches and modify the hardware description language (HDL) accordingly.
- **Optimisation of the FPGA HDL:** The clock frequency and time registers utilized in this UHF stimulation topology were determined empirically, resulting in time constraints in the logic design. To overcome this limitation, a theoretical approach should be used to determine the optimal clock frequency and implement a pipeline architecture. The current design uses a uniform clock frequency for all processes, which increases the power consumption of the FPGA. In future designs, it is recommended to design finite state machines (FSMs) with different clock frequencies and use synchronizers to transfer data between clock domains. Additionally, adding logic to enable and disable clock signals in different parts of the FPGA can improve the power efficiency and should be taken into consideration when designing an integrated circuit.

Bibliography

[1] F. T. Sun and M. J. Morrell, “Closed-loop Neurostimulation : The Clinical Experience,” pp. 553–563, 2014. DOI: 10.1007/s13311-014-0280-3.

[2] D. W. Dodick, S. D. Silberstein, K. L. Reed, *et al.*, “Safety and efficacy of peripheral nerve stimulation of the occipital nerves for the management of chronic migraine: Long-term results from a randomized, multicenter, double-blinded, controlled study,” *Cephalalgia*, vol. 35, no. 4, pp. 344–358, 2015, ISSN: 14682982. DOI: 10.1177/0333102414543331.

[3] H. M. Lee, H. Park, and M. Ghovanloo, “A power-efficient wireless system with adaptive supply control for deep brain stimulation,” *IEEE Journal of Solid-State Circuits*, vol. 48, no. 9, pp. 2203–2216, 2013, ISSN: 00189200. DOI: 10.1109/JSSC.2013.2266862.

[4] K. Chen, Z. Yang, L. Hoang, J. Weiland, M. Humayun, and W. Liu, “An integrated 256-channel epiretinal prosthesis,” *IEEE Journal of Solid-State Circuits*, vol. 45, no. 9, pp. 1946–1956, 2010, ISSN: 00189200. DOI: 10.1109/JSSC.2010.2055371.

[5] H. Xu, E. Noorsal, K. Sooksood, J. Becker, and M. Ortmanns, “A multichannel neurostimulator with transcutaneous closed-loop power control and self-adaptive supply,” *European Solid-State Circuits Conference*, pp. 309–312, 2012, ISSN: 19308833. DOI: 10.1109/ESSCIRC.2012.6341316.

[6] S. K. Kelly, K. Kelly, M. All, J. L. Wyatt, and A. C. Smith, “A System for Efficient Neural Stimulation with by in partial fulfillment of the requirements for the degree of at the October 2003,” *October*, 2003.

[7] S. K. Arfin and R. Sarpeshkar, “An energy-efficient, adiabatic electrode stimulator with inductive energy recycling and feedback current regulation,” *IEEE Transactions on Biomedical Circuits and Systems*, vol. 6, no. 1, pp. 1–14, 2012, ISSN: 19324545. DOI: 10.1109/TBCAS.2011.2166072.

[8] M. N. van Dongen, F. E. Hoebeek, S. K. Koekkoek, C. I. De Zeeuw, and W. A. Serdijn, “High frequency switched-mode stimulation can evoke post synaptic responses in cerebellar principal neurons,” *Frontiers in Neuroengineering*, vol. 8, no. MAR, pp. 1–10, 2015, ISSN: 16626443. DOI: 10.3389/fneng.2015.00002.

[9] J. Malmivuo and R. Plonsey, *Bioelectromagnetism*. New York: Oxford University Press, 1995, p. 45. [Online]. Available: www.biolabor.hu.

[10] E. N. Marieb and K. Hoehn, *Human Anatomy & Physiology*. 2012, pp. 634–834, ISBN: 9780321743268.

[11] T. Sun, X. Xie, and Z. Wang, *Wireless Power Transfer for Medical Microsystems*. New York: Springer, 2013, ISBN: 9781461477013.

[12] T. Vos, “Global, regional, and national incidence, prevalence, and years lived with disability for 328 diseases and injuries for 195 countries, 1990-2016: A systematic analysis for the Global Burden of Disease Study 2016,” *The Lancet*, vol. 390, no. 10100, pp. 1211–1259, 2017, ISSN: 1474547X. DOI: 10.1016/S0140-6736(17)32154-2.

[13] S. Miller, A. J. Sinclair, B. Davies, and M. Matharu, “Neurostimulation in the treatment of primary headaches,” *Practical Neurology*, vol. 16, no. 5, pp. 362–375, 2016, ISSN: 14747766. DOI: 10.1136/practneurol-2015-001298.

[14] D. M. Meletiche, J. H. Lofland, and W. B. Young, “Quality-of-life differences between patients with episodic and transformed migraine,” *Headache*, vol. 41, no. 6, pp. 573–578, 2001, ISSN: 00178748. DOI: 10.1046/j.1526-4610.2001.041006573.x.

[15] J. Munakata, E. Hazard, D. Serrano, *et al.*, “Economic burden of transformed migraine: Results from the american migraine prevalence and prevention (AMPP) study,” *Headache*, vol. 49, no. 4, pp. 498–508, 2009, ISSN: 00178748. DOI: 10.1111/j.1526-4610.2009.01369.x.

[16] R. B. Lipton, M. L. Diamond, and S. J. Tepper, “Expert Perspectives— Migraine Prevention for Highly Impacted Patients,” vol. 6, no. 2, pp. 1–4, 2011.

[17] M. Ashina, S. Tepper, J. L. Brandes, *et al.*, “Efficacy and safety of erenumab (AMG334) in chronic migraine patients with prior preventive treatment failure: A subgroup analysis of a randomized, double-blind, placebo-controlled study,” *Cephalalgia*, vol. 38, no. 10, pp. 1611–1621, 2018, ISSN: 14682982. DOI: 10.1177/0333102418788347.

[18] A. J. Sinclair, A. Sturrock, B. Davies, and M. Matharu, “Headache management: Pharmacological approaches,” *Practical Neurology*, vol. 15, no. 6, pp. 411–423, 2015, ISSN: 14747766. DOI: 10.1136/practneurol-2015-001167.

[19] J. Schoenen, R. H. Jensen, M. Lantéri-Minet, *et al.*, “Stimulation of the sphenopalatine ganglion (SPG) for cluster headache treatment. Pathway CH-1: A randomized, sham-controlled study,” *Cephalalgia*, vol. 33, no. 10, p. 816, Jul. 2013, ISSN: 03331024. DOI: 10.1177/0333102412473667. [Online]. Available: /pmc/articles/PMC3724276/%20/pmc/articles/PMC3724276/?report=abstract%20https://www.ncbi.nlm.nih.gov/pmc/articles/PMC3724276/.

[20] D. Fontaine, Y. Lazorthes, P. Mertens, and Blond, “Safety and efficacy of deep brain stimulation in refractory cluster headache: a randomized placebo-controlled double-blind trial followed by a 1-year open extension,” *J Headache Pain*, vol. 11, pp. 23–31, 2010. DOI: 10.1007/s10194-009-0169-4.

[21] J. R. Saper, D. W. Dodick, S. D. Silberstein, S. McCarville, M. Sun, and P. J. Goadsby, “Occipital nerve stimulation for the treatment of intractable chronic migraine headache: ONSTIM feasibility study,” *Cephalalgia*, vol. 31, no. 3, pp. 271–285, 2011, ISSN: 03331024. DOI: 10.1177/0333102410381142.

[22] S. D. Silberstein, D. W. Dodick, J. Saper, *et al.*, “Safety and efficacy of peripheral nerve stimulation of the occipital nerves for the management of chronic migraine: Results from a randomized, multicenter, double-blinded, controlled study,” *Cephalalgia*, vol. 32, no. 16, pp. 1165–1179, 2012, ISSN: 14682982. DOI: 10.1177/0333102412462642.

[23] K. L. Reed, S. B. Black, C. J. Banta, and K. R. Will, “Combined occipital and supraorbital neurostimulation for the treatment of chronic migraine headaches: Initial experience,” *Cephalalgia*, vol. 30, no. 3, pp. 260–271, 2010, ISSN: 03331024. DOI: 10.1111/j.1468-2982.2009.01996.x.

[24] S. Hann and A. Sharan, “Dual occipital and supraorbital nerve stimulation for chronic migraine: A single-center experience, review of literature, and surgical considerations,” *Neurosurgical Focus*, vol. 35, no. 3, pp. 1–8, 2013, ISSN: 10920684. DOI: 10.3171/2013.6.FOCUS1323.

[25] D. Rodrigo, P. Acín, and P. Bermejo, “Occipital nerve stimulation for refractory chronic migraine: Results of a long-term prospective study,” *Pain Physician*, vol. 20, no. 1, E151–E159, 2017, ISSN: 21501149. DOI: 10.36076/2017.1.e151.

[26] D. R. Merrill, M. Bikson, and J. G. Jefferys, “Electrical stimulation of excitable tissue: Design of efficacious and safe protocols,” *Journal of Neuroscience Methods*, vol. 141, no. 2, pp. 171–198, 2005, ISSN: 01650270. DOI: 10.1016/j.jneumeth.2004.10.020.

[27] M. N. Van Dongen and W. A. Serdijn, “A Power-Efficient Multichannel Neural Stimulator Using High-Frequency Pulsed Excitation From an Unfiltered Dynamic Supply,” *IEEE Transactions on Biomedical Circuits and Systems*, vol. 10, no. 1, pp. 61–71, 2016, ISSN: 19324545. DOI: 10.1109/TBCAS.2014.2363736.

[28] D. K. Freeman, J. M. O’Brien, P. Kumar, *et al.*, “A sub-millimeter, inductively powered neural stimulator,” *Frontiers in Neuroscience*, vol. 11, no. NOV, pp. 1–12, 2017, ISSN: 1662453X. DOI: 10.3389/fnins.2017.00659.

[29] M. Ortmanns, A. Rocke, M. Gehrke, and H. J. Tiedtke, “A 232-Channel Epiretinal Stimulator ASIC,” *IEEE Journal of Solid-State Circuits*, vol. 42, no. 12, pp. 2946–2959, 2007, ISSN: 00189200. DOI: 10.1109/JSSC.2007.908693.

[30] E. Noorsal, K. Sooksood, H. Xu, R. Hornig, J. Becker, and M. Ortmanns, “A neural stimulator frontend with high-voltage compliance and programmable pulse shape for epiretinal implants,” *IEEE Journal of Solid-State Circuits*, vol. 47, no. 1, pp. 244–256, 2012, ISSN: 00189200. DOI: 10.1109/JSSC.2011.2164667.

[31] H. M. Lee and M. Ghovanloo, “A power-efficient wireless capacitor charging system through an inductive link,” *IEEE Transactions on Circuits and Systems II: Express Briefs*, vol. 60, no. 10, pp. 707–711, 2013, ISSN: 15497747. DOI: 10.1109/TCSII.2013.2278104.

[32] H. Xu, U. Bihr, J. Becker, and M. Ortmanns, “A multi-channel neural stimulator with resonance compensated inductive receiver and closed-loop smart power management,” *Proceedings - IEEE International Symposium on Circuits and Systems*, pp. 638–641, 2013, ISSN: 02714310. DOI: 10.1109/ISCAS.2013.6571923.

[33] I. Williams and T. G. Constandinou, “An energy-efficient, dynamic voltage scaling neural stimulator for a proprioceptive prosthesis,” *IEEE Transactions on Biomedical Circuits and Systems*, vol. 7, no. 2, pp. 129–139, 2013, ISSN: 19324545. DOI: 10.1109/TBCAS.2013.2256906.

[34] W. Y. Hsu and A. Schmid, “Compact, Energy-Efficient High-Frequency Switched Capacitor Neural Stimulator with Active Charge Balancing,” *IEEE Transactions on Biomedical Circuits and Systems*, vol. 11, no. 4, pp. 878–888, 2017, ISSN: 19409990. DOI: 10.1109/TBCAS.2017.2694144.

[35] A. Wongsarnpigoon and W. M. Grill, “Energy-efficient waveform shapes for neural stimulation revealed with a genetic algorithm,” *Journal of Neural Engineering*, vol. 7, no. 4, 2010, ISSN: 17412560. DOI: 10.1088/1741-2560/7/4/046009.

[36] A. Urso, V. Giagka, M. Van Dongen, and W. A. Serdijn, “An Ultra High-Frequency 8-Channel Neurostimulator Circuit with 68 Peak Power Efficiency,” *IEEE Transactions on Biomedical Circuits and Systems*, vol. 13, no. 5, pp. 882–892, 2019, ISSN: 19409990. DOI: 10.1109/TBCAS.2019.2920294.

[37] M. N. van Dongen and W. A. Serdijn, “Does a coupling capacitor enhance the charge balance during neural stimulation? An empirical study,” *Medical and Biological Engineering and Computing*, vol. 54, no. 1, pp. 93–101, 2016, ISSN: 17410444. DOI: 10.1007/s11517-015-1312-9.

[38] N. Butz, A. Taschwer, S. Nessler, Y. Manoli, and M. Kuhl, “A 22 V Compliant 56 μW twin-track active charge balancing enabling 100% charge compensation even in monophasic and 36% amplitude correction in biphasic neural stimulators,” *IEEE Journal of Solid-State Circuits*, vol. 53, no. 8, pp. 2298–2310, Aug. 2018, ISSN: 00189200. DOI: 10.1109/JSSC.2018.2828823.

[39] I. Williams and T. G. Constandinou, “An energy-efficient, dynamic voltage scaling neural stimulator for a proprioceptive prosthesis,” *IEEE Transactions on Biomedical Circuits and Systems*, vol. 7, no. 2, pp. 129–139, 2013, ISSN: 19324545. DOI: 10.1109/TBCAS.2013.2256906.

[40] J. J. Sit and R. Sarpeshkar, “A low-power blocking-capacitor-free charge-balanced electrode-stimulator chip with lesst than 6 nA DC error for 1-mA: Full-Scale Stimulation,” *IEEE Transactions on Biomedical Circuits and Systems*, vol. 1, no. 3, pp. 172–183, Sep. 2007, ISSN: 19324545. DOI: 10.1109/TBCAS.2007.911631.

[41] H. Chun, Y. Yang, and T. Lehmann, “Safety ensuring retinal prosthesis with precise charge balance and low power consumption,” *IEEE Transactions on Biomedical Circuits and Systems*, vol. 8, no. 1, pp. 108–118, 2014, ISSN: 19324545. DOI: 10.1109/TBCAS.2013.2257171.

[42] S. Nag, X. Jia, N. V. Thakor, and D. Sharma, “Flexible charge balanced stimulator with 5.6 fC accuracy for 140 nC injections,” *IEEE Transactions on Biomedical Circuits and Systems*, vol. 7, no. 3, pp. 266–275, 2013, ISSN: 19324545. DOI: 10.1109/TBCAS.2012.2205574.

[43] X. Fang, J. Wills, J. Granacki, J. LaCoss, A. Arakelian, and J. Weiland, “Novel charge-metering stimulus amplifier for biomimetic implantable prosthesis,” *Proceedings - IEEE International Symposium on Circuits and Systems*, pp. 569–572, 2007, ISSN: 02714310. DOI: 10.1109/ISCAS.2007.378801.

[44] X. Fang, J. Wills, J. Granacki, J. LaCoss, and J. Choma, “CMOS charge-metering microstimulator for implantable prosthetic device,” *Midwest Symposium on Circuits and Systems*, pp. 826–829, 2008, ISSN: 15483746. DOI: 10.1109/MWSCAS.2008.4616927.

[45] R. Ranjandish, O. Shoaei, and A. Schmid, “A Fully Fail-Safe Capacitive-Based Charge Metering Method for Active Charge Balancing in Deep Brain Stimulation,” *PRIME 2018 - 14th Conference on Ph.D. Research in Microelectronics and Electronics*, pp. 249–252, Aug. 2018. DOI: 10.1109/PRIME.2018.8430327.

[46] F. Kolbl, R. Guillaume, J. Hasler, *et al.*, “A closed-loop charge balancing FPAA circuit with sub-nano-amp DC error for electrical stimulation,” *IEEE 2014 Biomedical Circuits and Systems Conference, BioCAS 2014 - Proceedings*, pp. 616–619, Dec. 2014. DOI: 10.1109/BIOCAS.2014.6981801.

[47] S. Luan and T. G. Constandinou, “A charge-metering method for voltage-mode neural stimulation,” *Journal of Neuroscience Methods*, vol. 224, pp. 39–47, Mar. 2014, ISSN: 0165-0270. DOI: 10.1016/J.JNEUMETH.2013.11.028.

[48] M. van Dongen and W. Serdijn, *Design Efficient and Safe Neural Stimulator*. Springer, 2016, ISBN: 9783319281292. [Online]. Available: http://www.springer.com/series/7381.

[49] E. Greenwald, C. Maier, Q. Wang, *et al.*, “A CMOS Current Steering Neurostimulation Array with Integrated DAC Calibration and Charge Balancing,” *IEEE Transactions on Biomedical Circuits and Systems*, vol. 11, no. 2, pp. 324–335, Apr. 2017, ISSN: 19324545. DOI: 10.1109/TBCAS.2016.2609854.

[50] E. Maghsoudloo, M. Rezaei, M. Sawan, and B. Gosselin, “A new charge balancing scheme for electrical microstimulators based on modulated anodic stimulation pulse width,” *Proceedings - IEEE International Symposium on Circuits and Systems*, vol. 2016-July, pp. 2443–2446, Jul. 2016, ISSN: 02714310. DOI: 10.1109/ISCAS.2016.7539086.

[51] K. Sooksood, T. Stieglitz, and M. Ortmanns, “An active approach for charge balancing in functional electrical stimulation,” *IEEE Transactions on Biomedical Circuits and Systems*, vol. 4, no. 3, pp. 162–170, Jun. 2010, ISSN: 19324545. DOI: 10.1109/TBCAS.2010.2040277.

[52] M. N. V. Dongen and W. A. Serdijn, “A transistor-only power-efficient high-frequency voltage-mode stimulator for a multichannel system,” pp. 93–96, 2013.

[53] U. M. Jow and M. Ghovanloo, “Design and optimization of printed spiral coils for efficient inductive power transmission,” *Proceedings of the IEEE International Conference on Electronics, Circuits, and Systems*, vol. 1, no. 3, pp. 70–73, 2007. DOI: 10.1109/ICECS.2007.4510933.

[54] G. L. Barbruni, P. M. Ros, D. Demarchi, S. Carrara, and D. Ghezzi, “Miniaturised Wireless Power Transfer Systems for Neurostimulation: A Review,” *IEEE Transactions on Biomedical Circuits and Systems*, vol. 14, no. 6, pp. 1160–1178, 2020, ISSN: 19409990. DOI: 10.1109/TBCAS.2020.3038599.

[55] IEEE, *IEEE Standard for Safety Levels With Respect to Human Exposure to Radio Frequency Electromagnetic Fields, 3 kHz to 300 GHz*. 2006, vol. 2005, pp. 01–238, ISBN: VO -.

[56] K. Agarwal, R. Jegadeesan, Y. X. Guo, and N. V. Thakor, “Wireless Power Transfer Strategies for Implantable Bioelectronics,” *IEEE Reviews in Biomedical Engineering*, vol. 10, pp. 136–161, 2017, ISSN: 19411189. DOI: 10.1109/RBME.2017.2683520.

[57] R. Jegadeesan and Y. X. Guo, “Topology selection and efficiency improvement of inductive power links,” *IEEE Transactions on Antennas and Propagation*, vol. 60, no. 10, pp. 4846–4854, 2012, ISSN: 0018926X. DOI: 10.1109/TAP.2012.2207325.

[58] A. Denisov and E. Yeatman, “Ultrasonic vs. inductive power delivery for miniature biomedical implants,” *2010 International Conference on Body Sensor Networks, BSN 2010*, pp. 84–89, 2010. DOI: 10.1109/BSN.2010.27.

[59] S. Ramo, J. R. Whinnery, and T. Van Duzer, *Fields and Waves in Communication Electronics*, 1994.

[60] C. M. Zierhofer and E. S. Hochmair, “Geometric approach for coupling enhancement of magnetically coupled coils,” *IEEE Transactions on Biomedical Engineering*, vol. 43, no. 7, pp. 708–714, 1996, ISSN: 00189294. DOI: 10.1109/10.503178.

[61] D. W. Knight, “Solenoid Inductance Calculation With emphasis on radio-frequency applications,” Tech. Rep., 2016, p. 30. [Online]. Available: http://g3ynh.info/zdocs/magnetics/.http://g3ynh.info/.

[62] M. Schormans, V. Valente, and A. Demosthenous, “Practical Inductive Link Design for Biomedical Wireless Power Transfer : A Tutorial,” *IEEE Transactions on Biomedical Circuits and Systems*, vol. 12, no. 5, pp. 1–19, 2018. DOI: 10.1109/TBCAS.2018.2846020.

[63] W. Zhang, S. C. Wong, C. K. Tse, and Q. Chen, “Analysis and comparison of secondary series- and parallel-compensated inductive power transfer systems operating for optimal efficiency and load-independent voltage-transfer ratio,” *IEEE Transactions on Power Electronics*, vol. 29, no. 6, pp. 2979–2990, 2014, ISSN: 08858993. DOI: 10.1109/TPEL.2013.2273364.

[64] H. Lyu, J. Wang, J. H. La, J. M. Chung, and A. Babakhani, “An Energy-efficient Wirelessly Powered Millimeter-scale Neurostimulator with Optimized Inductive Loop Antenna and Custom Rectifier,” *IEEE MTT-S International Microwave Symposium Digest*, vol. 2018-June, pp. 1401–1404, 2018, ISSN: 0149645X. DOI: 10.1109/MWSYM.2018.8439143.

[65] M. Kiani and M. Ghovanloo, “An RFID-based closed-loop wireless power transmission system for biomedical applications,” *IEEE Transactions on Circuits and Systems II: Express Briefs*, vol. 57, no. 4, pp. 260–264, 2010, ISSN: 15497747. DOI: 10.1109/TCSII.2010.2043470.

[66] K. Van Schuylenbergh and R. Puers, *Inductive Powering: Basic Theory and Application*. 2009, vol. 151, p. 233, ISBN: 9789048124114. DOI: 10.1007/978-90-481-2412-1. arXiv: 9809069 [gr-qc]. [Online]. Available: http://www.airitilibrary.com/Publication/alDetailedMesh?docid=10190376-201401-201404010027-201404010027-101-108.

[67] G. A. Kendir, W. Liu, G. Wang, *et al.*, “An optimal design methodology for inductive power link with Class-E amplifier,” *IEEE Transactions on Circuits and Systems I: Regular Papers*, vol. 52, no. 5, pp. 857–866, 2005, ISSN: 10577122. DOI: 10.1109/TCSI.2005.846208.

[68] N. d. N. Donaldson and T. A. Perkins, “Analysis of resonant coupled coils in the design of radio frequency transcutaneous links,” *Medical & Biological Engineering & Computing*, vol. 21, no. 5, pp. 612–627, 1983, ISSN: 01400118. DOI: 10.1007/BF02442388.

[69] W. H. Ko, S. P. Liang, and C. D. Fung, “Design of radio-frequency powered coils for implant instruments,” *Medical & Biological Engineering & Computing*, vol. 15, no. 6, pp. 634–640, 1977, ISSN: 01400118. DOI: 10.1007/BF02457921.

[70] M. Soma, D. C. Galbraith, and R. L. White, “Radio-Frequency Coils in Implantable Devices: Misalignment Analysis and Design Procedure,” *IEEE Transactions on Biomedical Engineering*, vol. 40, no. 7, p. 715, 1993, ISSN: 00189294.

[71] U. M. Jow and M. Ghovanloo, “Modeling and optimization of printed spiral coils in air and muscle tissue environments,” *Proceedings of the 31st Annual International Conference of the IEEE Engineering in Medicine and Biology Society: Engineering the Future of Biomedicine, EMBC 2009*, vol. 3, no. 5, pp. 6387–6390, 2009. DOI: 10.1109/IEMBS.2009.5333876.

[72] Y. Lu and W. H. Ki, “A 13.56 MHz CMOS active rectifier with switched-offset and compensated biasing for biomedical wireless power transfer systems,” *IEEE Transactions on Biomedical Circuits and Systems*, vol. 8, no. 3, pp. 334–344, 2014, ISSN: 19324545. DOI: 10.1109/TBCAS.2013.2270177.

[73] K. F. E. Lee, “A timing controlled AC-DC converter for biomedical implants,” *Digest of Technical Papers - IEEE International Solid-State Circuits Conference*, vol. 53, pp. 128–129, 2010, ISSN: 01936530. DOI: 10.1109/ISSCC.2010.5434021.

[74] M. Kiani, U. M. Jow, and M. Ghovanloo, “Design and optimization of a 3-coil inductive link for efficient wireless power transmission,” *IEEE Transactions on Biomedical Circuits and Systems*, vol. 5, no. 6, pp. 579–591, 2011, ISSN: 19324545. DOI: 10.1109/TBCAS.2011.2158431.

[75] M. W. Baker and R. Sarpeshkar, “Feedback analysis and design of RF power links for low-power bionic systems,” *IEEE Transactions on Biomedical Circuits and Systems*, vol. 1, no. 1, pp. 28–38, 2007, ISSN: 19324545. DOI: 10.1109/TBCAS.2007.893180.

[76] M. Ghovanloo, “Wireless Power Transfer From Implantable Devices to Electric Vehicles,” pp. 1–71, 2019.

[77] A. Kurs, A. Karalis, R. Moffatt, J. D. Joannopoulos, and Fisher, “Wireless power transfer via strongly coupled magnetic resonances,” *Science*, vol. 317, no. 5834, pp. 83–86, 2007, ISSN: 00368075. DOI: 10.1126/science.1143254.

[78] A. Karalis, J. D. Joannopoulos, and M. Soljačić, “Efficient wireless non-radiative mid-range energy transfer,” *Annals of Physics*, vol. 323, no. 1, pp. 34–48, 2008, ISSN: 00034916. DOI: 10.1016/j.aop.2007.04.017. eprint: 0611063 (physics).

[79] A. P. Sample, D. A. Meyer, and J. R. Smith, “Analysis, experimental results, and range adaptation of magnetically coupled resonators for wireless power transfer,” *IEEE Transactions on Industrial Electronics*, vol. 58, no. 2, pp. 544–554, 2011, ISSN: 02780046. DOI: 10.1109/TIE.2010.2046002.

[80] a. K. Ramrakhyani, S. Mirabbasi, Mu Chiao, and C. M, “Design and optimization of resonance-based efficient wireless power delivery systems for biomedical implants.,” *IEEE transactions on biomedical circuits and systems*, vol. 5, no. 1, pp. 48–63, 2011, ISSN: 1932-4545. DOI: 10.1109/TBCAS.2010.2072782. [Online]. Available: http://www.ncbi.nlm.nih.gov/pubmed/23850978.

[81] R. F. Xue, K. W. Cheng, and M. Je, “High-efficiency wireless power transfer for biomedical implants by optimal resonant load transformation,” *IEEE Transactions on Circuits and Systems I: Regular Papers*, vol. 60, no. 4, pp. 867–874, 2013, ISSN: 15498328. DOI: 10.1109/TCSI.2012.2209297.

[82] K. M. Silay, D. Dondi, L. Larcher, *et al.*, “Load optimization of an inductive power link for remote powering of biomedical implants,” *Proceedings - IEEE International Symposium on Circuits and Systems*, pp. 533–536, 2009, ISSN: 02714310. DOI: 10.1109/ISCAS.2009.5117803.

[83] “Multistage Complex-Impedance Matching Network Analysis and Optimization,” *IEEE Transactions on Circuits and Systems II: Express Briefs*, vol. 63, no. 9, pp. 833–837, 2016, ISSN: 15583791.

[84] Y. Zhang and Z. Zhao, “Frequency splitting analysis of two-coil resonant wireless power transfer,” *IEEE Antennas and Wireless Propagation Letters*, vol. 13, no. 2, pp. 400–402, 2014, ISSN: 15361225. DOI: 10.1109/LAWP.2014.2307924.

[85] H. D. Thanh and J. I. Agbinya, “Investigation and study of mode splitting in near field inductive communication systems,” *International Journal of Electronics and Telecommunications*, vol. 59, no. 2, pp. 185–194, 2013, ISSN: 20818491. DOI: 10.2478/eletel-2013-0022.

[86] W. Q. Niu, J. X. Chu, W. Gu, and A. D. Shen, “Exact analysis of frequency splitting phenomena of contactless power transfer systems,” *IEEE Transactions on Circuits and Systems I: Regular Papers*, vol. 60, no. 6, pp. 1670–1677, 2013, ISSN: 15498328. DOI: 10.1109/TCSI.2012.2221172.

[87] K. N. Bocan and E. Sejdi, “Adaptive Transcutaneous Power Transfer to Implantable Devices : A State of the Art Review,” vol. 16, no. 3, p. 393, 2016. DOI: 10.3390/s16030393.

[88] T. Van Breussegem and M. Steyaert, *CMOS Integrated Capacitive DC–DC Converters*. New York: Springer, 2013, ISBN: 9781461442790.

[89] P. Si, A. P. Hu, S. Malpas, and D. Budgett, “A frequency control method for regulating wireless power to implantable devices,” *IEEE Transactions on Biomedical Circuits and Systems*, vol. 2, no. 1, pp. 22–29, 2008, ISSN: 19324545. DOI: 10.1109/TBCAS.2008.918284.

[90] S. O. Driscoll, A. S. Y. Poon, and T. H. Meng, “A mm-Sized Implantable Power Receiver with Adaptive Link Compensation,” pp. 294–296, 2009.

[91] Y. Lu, S. Mai, C. Zhang, H. Chen, and Z. Wang, “Design optimization of printed spiral coils and impedance matching networks for load-variable wireless power transfer systems,” *EDSSC 2017 - 13th IEEE International Conference on Electron Devices and Solid-State Circuits*, vol. 2017-Janua, pp. 1–2, 2017. DOI: 10.1109/EDSSC.2017.8126473.

[92] M. A. Hannan, S. Mutashar, S. A. Samad, and A. Hussain, “Energy harvesting for the implantable biomedical devices: Issues and challenges,” *BioMedical Engineering Online*, vol. 13, no. 1, pp. 1–23, 2014, ISSN: 1475925X. DOI: 10.1186/1475-925X-13-79.

[93] M. Schormans, V. Valente, and A. Demosthenous, “Efficiency optimization of class-D biomedical inductive wireless power transfer systems by means of frequency adjustment,” *Proceedings of the Annual International Conference of the IEEE Engineering in Medicine and Biology Society, EMBS*, vol. 2015-Nov, no. 1, pp. 5473–5476, 2015, ISSN: 1557170X. DOI: 10.1109/EMBC.2015.7319630.

[94] M. Schormans, V. Valente, and A. Demosthenous, “Frequency splitting analysis and compensation method for inductive wireless powering of implantable biosensors,” *Sensors (Switzerland)*, vol. 16, no. 8, 2016, ISSN: 14248220. DOI: 10.3390/s16081229.

[95] M. Kiani, B. Lee, P. Yeon, and M. Ghovanloo, “A Q-Modulation Technique for Efficient Inductive Power Transmission,” *IEEE Journal of Solid-State Circuits*, vol. 50, no. 12, pp. 2839–2848, 2015, ISSN: 00189200. DOI: 10.1109/JSSC.2015.2453201.

[96] B. Lee, P. Yeon, and M. Ghovanloo, “A multicycle Q-modulation for dynamic optimization of inductive links,” *IEEE Transactions on Industrial Electronics*, vol. 63, no. 8, pp. 5091–5100, 2016, ISSN: 02780046. DOI: 10.1109/TIE.2016.2550009.

[97] Z. Pantic and S. M. Lukic, “Framework and Topology for Active Tuning of Parallel Compensated Receivers in Power Transfer Systems,” vol. 27, no. 11, pp. 4503–4513, 2012.

[98] D. Ahn and S. Hong, “Wireless power transfer resonance coupling amplification by load-modulation switching controller,” *IEEE Transactions on Industrial Electronics*, vol. 62, no. 2, pp. 898–909, 2015, ISSN: 02780046. DOI: 10.1109/TIE.2014.2336627.

[99] Y. Moriwaki, T. Imura, and Y. Hori, “Basic study on reduction of reflected power using DC/DC converters in wireless power transfer system via magnetic resonant coupling,” *INTELEC, International Telecommunications Energy Conference (Proceedings)*, pp. 1–5, 2011, ISSN: 02750473. DOI: 10.1109/INTLEC.2011.6099737.

[100] M. Fu, H. Yin, X. Zhu, and C. Ma, “Analysis and tracking of optimal load in wireless power transfer systems,” *IEEE Transactions on Power Electronics*, vol. 30, no. 7, pp. 3952–3963, 2015, ISSN: 08858993. DOI: 10.1109/TPEL.2014.2347071.

[101] M. Fu, C. Ma, and X. Zhu, “A Cascaded Boost – Buck Converter for High-Efficiency Wireless Power Transfer Systems,” vol. 10, no. 3, pp. 1972–1980, 2014.

[102] W. X. Zhong and S. Y. R. Hui, “Maximum Energy Efficiency Tracking for Wireless Power,” vol. 30, no. 7, pp. 4025–4034, 2015.

[103] H. Li, J. Li, K. Wang, W. Chen, and X. Yang, “A Maximum Efficiency Point Tracking Control Scheme for Wireless Power Transfer Systems Using Magnetic Resonant Coupling,” vol. 30, no. 7, pp. 3998–4008, 2015.

[104] D. Ahn, S. Kim, J. Moon, and I.-k. Cho, “Wireless Power Transfer With Automatic Feedback Control of Load Resistance Transformation,” vol. 31, no. 11, pp. 7876–7886, 2016.

[105] T.-d. Yeo, D. Kwon, S.-t. Khang, and J.-w. Yu, “Design of Maximum Efficiency Tracking Control Scheme for Closed-Loop Wireless Power Charging,” vol. 32, no. 1, pp. 471–478, 2017.

[106] G. Wang, W. Liu, M. Sivaprakasam, and G. A. Kendir, “Design and analysis of an adaptive transcutaneous power telemetry for biomedical implants,” *IEEE Transactions on Circuits and Systems I: Regular Papers*, vol. 52, no. 10, pp. 2109–2117, 2005, ISSN: 10577122. DOI: 10.1109/TCSI.2005.852923.

[107] P. G. Zufiria, *An Efficacious and Safe Multichannel Neurostimulator Powered by an Ultrasonic Wireless Link*, 2020. [Online]. Available: https://repository.tudelft.nl/islandora/object/uuid%3A166f74ce-9109-4fb3-9ae3-afc7dad93ea8.

[108] S. K. Kelly and J. L. Wyatt, “A power-efficient neural tissue stimulator with energy recovery,” *IEEE Transactions on Biomedical Circuits and Systems*, vol. 5, no. 1, pp. 20–29, 2011, ISSN: 19324545. DOI: 10.1109/TBCAS.2010.2076384.

[109] A. Rashidi, N. Yazdani, and A. M. Sodagar, “Fully implantable, multi-channel microstimulator with tracking supply ribbon, multi-output charge pump and energy recovery,” *IET Circuits, Devices & Systems*, vol. 15, no. 2, pp. 104–120, Mar. 2021, ISSN: 1751-8598. DOI: 10.1049/CDS2.12007. [Online]. Available: https://onlinelibrary-wiley-com.tudelft.idm.oclc.org/doi/full/10.1049/cds2.12007%20https://onlinelibrary-wiley-com.tudelft.idm.oclc.org/doi/abs/10.1049/cds2.12007%20https://ietresearch-onlinelibrary-wiley-com.tudelft.idm.oclc.org/doi/10.1049/cds2.12007.

[110] J. Charthad, T. C. Chang, Z. Liu, *et al.*, “A mm-Sized wireless implantable device for electrical stimulation of peripheral nerves,” *IEEE Transactions on Biomedical Circuits and Systems*, vol. 12, no. 2, pp. 257–270, Apr. 2018, ISSN: 19324545. DOI: 10.1109/TBCAS.2018.2799623.

[111] H.-M. Lee, H. Park, and M. Ghovanloo, “A Power-Efficient Wireless System With Adaptive Supply Control for Deep Brain Stimulation.,” *IEEE journal of solid-state circuits*, vol. 48, no. 9, pp. 2203–2216, Sep. 2013, ISSN: 0018-9200. DOI: 10.1109/JSSC.2013.2266862. [Online]. Available: http://www.ncbi.nlm.nih.gov/pubmed/24678126%20http://www.pubmedcentral.nih.gov/articlerender.fcgi?artid=PMC3964183.

[112] R. Ranjandish and O. Shoaei, “A simple and precise charge balancing method for voltage mode stimulation,” *IEEE 2014 Biomedical Circuits and Systems Conference, BioCAS 2014 - Proceedings*, pp. 376–379, Dec. 2014. DOI: 10.1109/BIOCAS.2014.6981741.

[113] H. M. Lee and M. Ghovanloo, “An integrated power-efficient active rectifier with offset-controlled high speed comparators for inductively powered applications,” *IEEE Transactions on Circuits and Systems I: Regular Papers*, vol. 58, no. 8, pp. 1749–1760, 2011, ISSN: 15498328. DOI: 10.1109/TCSI.2010.2103172.